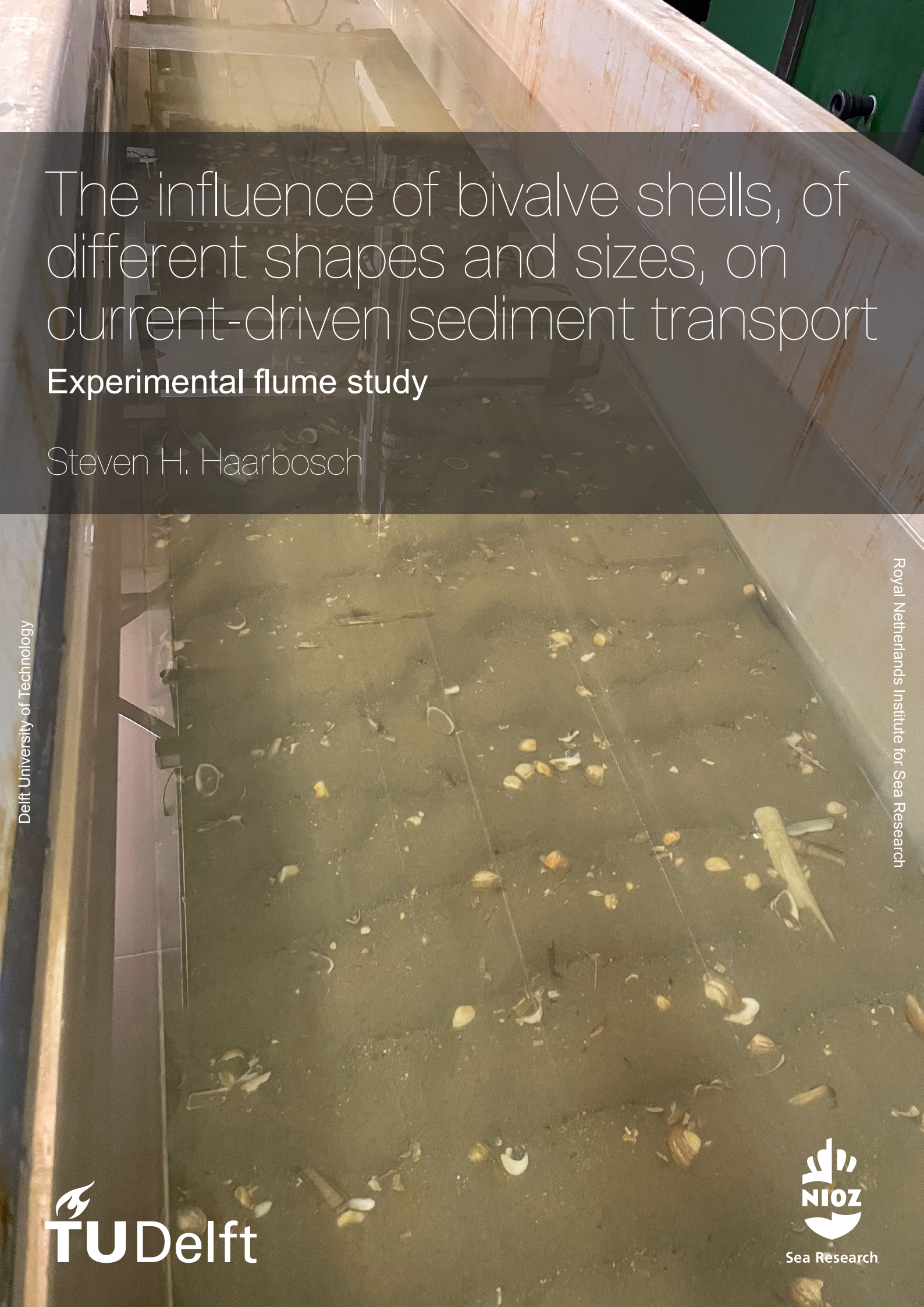

The influence of bivalve shells, of different shapes and sizes, on current-driven sediment transport

Experimental flume study

Steven H. Haarbosch

Delft University of Technology

Royal Netherlands Institute for Sea Research

TU Delft

NIOZ Sea Research

Cover: Top view of a sediment-shell mixture in the racetrack flume.
(On October 24th, 2022, at NIOZ in Yerseke, the Netherlands)

The influence of bivalve shells, of different shapes and sizes, on current-driven sediment transport

Experimental flume study

by

Steven H. Haarbosch

in partial fulfillment of the requirements for the degree of

Master of Science
in Hydraulic Engineering

at the Delft University of Technology,
to be defended publicly on Wednesday, August 30th, 2023, at 3:00 PM.

Student number:	5182352	
Project duration:	September 2022 – August 2023	
Thesis committee:	Dr. ir. B.C. van Prooijen	TU Delft
	Dr. ir. S.G. Pearson	TU Delft
	Dr. ir. S. de Vries	TU Delft
	T.J. Kooistra, MSc.	NIOZ

Delft University of Technology
Faculty of Civil Engineering and Geosciences
Department of Hydraulic Engineering

TU Delft Delft University of Technology

NIOZ Royal Netherlands Institute for Sea Research

Summary

In the Netherlands, the coastlands act as the principal protection against the sea. Effective coastal management strategies are needed to protect the Dutch coastline against erosion and flooding. The preferred coastal management strategy is sand nourishment. Nourishments have become larger in scale and more complex over the last 70 years. And, in the coming decades, the demands for nourishment are expected to further increase due to the rising sea levels. Therefore, it becomes increasingly important to have more reliable sediment transport predictions to help manage the placement of sand. In addition to sand, large quantities of mollusc shells can also be found on the ocean floor. With increasing shell content, sand ripple dimensions are reduced, and ripple migration rates slow down. In essence, this limits the rate of bed load transport, meaning that existing tools to predict sediment transport may overestimate transport in a shell environment. Thus, there is still a need to better qualify the threshold of motion of sand grains and quantify bed load transport of a bed composition consisting of a sediment-shell mixture. This study aimed to gain insight into the current-driven bed load transport of a sediment-shell bed composition using bivalve shells of different shapes and sizes.

Flume experiments were carried out in the racetrack flume facility at the NIOZ Royal Netherlands Institute for Sea Research. A set of two separate experiments were conducted: (i) a slowly accelerating flow experiment to measure the influence of bivalve shells on the threshold of motion of sand grains, and (ii) a constant flow experiment to measure their influence on current-driven bed load transport. In the constant flow experiment, flow velocities ranging from below (0.25 m s^{-1}) to above (0.45 m s^{-1}) the threshold of motion were tested. The sediment-shell bed composition was altered in both experiments by changing the volumetric percentage of shell content. The bed compositions consisted of two different bivalve shell species: *Ensis leei* (elongated) and *Spisula subtruncata* (rounded).

The slowly accelerating flow experiment showed an increased threshold of motion of sand grains with the presence of shells. At a low shell content of 5/10%, turbulence intensities increased, while a similar amount of motion of sand was observed for comparable depth-averaged velocities. When the shell content was further increased (20%), the depth-averaged velocities and turbulence intensities showed a distinct difference compared to the lower shell contents. In the case of a bed consisting of *S. subtruncata* or a mixture of both shells, the depth-averaged velocity required for incipient motion increased while the turbulence intensities decreased. In contrast, when considering a bed consisting of *E. leei* shells, the depth-averaged velocity decreased while the turbulence intensities increased.

The constant flow experiment showed a decrease in bed load transport rates with increasing shell content. Initially, at a shell content of 10%, the bed load transport rates only decreased marginally compared to a situation without shells, and no clear difference between shell species was observed. However, bed load transport rates further decreased when the shell content increased to 20%. The bed composition consisting of *E. leei* shells was shown to have higher transport rates than the *S. subtruncata*. Existing bed load transport formations deviated from measured bed load transport rates, and bed load transport did not exhibit a distinct impact on bed armouring.

It is proposed that shells initially increase turbulence intensities. As shell content increases, a second effect becomes prevalent, which is sediment stabilization. The smaller sediment grains are hidden from the flow by larger shell valves and fragments. Consequently, a higher bed shear stress is required to mobilize the sand grains. The relative importance of these processes varies depending on shell content, shell species, and the potential of the shell to enhance turbulence. With increasing shell content, bed load transport rates decrease. The *E. leei* shell appears to have a higher transport rate than the *S. subtruncata*, due to its ability to generate turbulence. Thus, when predicting sediment transport or the behavior of sand nourishments over time, the mere presence of shells alone is insufficient, and consideration of shell shape and size is crucial. Additionally, the enhancement of bed load transport predictors using stochastic modeling has been demonstrated to give more accurate predictions.

Acknowledgements

This thesis completes the Master of Science in Hydraulic Engineering program at Delft University of Technology. In September 2022, I started my thesis project and moved to Yerseke, the Netherlands. After conducting two distinct flume experiments and numerous experimental runs, I am finishing this master's thesis. The past ten months have been incredibly educational, at times challenging, yet predominantly an enjoyable experience.

The realization of this work would not have been possible without the support of others. First and foremost, I extend my thanks to my graduation committee for their invaluable contributions to this project. I want to thank my chair, Bram van Prooijen, for sharing your experience and knowledge and allowing me to present my research at the NCK Days 2023. I would also like to thank Stuart Pearson for his unwavering enthusiasm, constructive feedback, and for ensuring that I remained on track throughout this project. Thank you to Sierd de Vries for encouraging me to think more critically, and asking insightful questions that helped refine my research.

At NIOZ, I would like to say a special thank you to Tjitske Kooistra for welcoming me aboard for this experiment. It is incredible to recall that a field trip to the mudflat of the Western Scheldt back in May 2022 led to this opportunity and exciting collaboration. Working with you to conduct the experiments, engaging in critical thinking about the research, and having you on my committee truly expanded the research with your background and experience. Thank you, too, to Tjeerd Bouma for helping set up the flume experiment and for generously offering his time and knowledge.

At Utrecht University, I want to thank Maarten Kleinhans for his valuable feedback and ideas that elevated the quality of the results and discussion. Thank you, too, to Jorn Bosma for designing and conducting the experiments together and for the feedback you have provided me with.

Thank you to Chiu Cheng for sharing your experience conducting an experimental flume study. The many conversations during lunch and discussions over coffee breaks, coupled with your thorough review of my thesis, greatly contributed to its refinement.

I want to conclude this acknowledgment by offering my family and friends special thanks. Conducting experimental research demands long hours of focused work, critical thinking, and a willingness to endure challenges. During these times, your support, love, and encouragement were invaluable. Your understanding of my commitment to this project and your encouragement has been a constant source of motivation, helping me to stay on track, and focused on achieving my goals. Thank you for all your support.

Steven H. Haarbosch
Delft, August 2023

Contents

List of Figures

List of Tables

List of Symbols

C'	$m^{1/2}s^{-1}$	Chézy grain roughness
c_f	–	Friction coefficient
d	μm, mm	Grain diameter
d_{10}	μm, mm	Grain diameter at the 10^{th} percentile
d_{50}	μm, mm	Mean grain diameter
d_{90}	μm, mm	Grain diameter at the 90^{th} percentile
d_*	–	Dimensionless particle diameter
g	m s^{-2}	Gravitational acceleration
h	m	Water depth
K	–	Constant
κ	–	Von Kármán constant
k_s	mm, m	Nikuradse grain roughness
m	–	Scale factor
n	–	Shape factor
φ	–	Dimensionless bed load transport rate (Einstein parameter)
p	–	Probability of occurrence
$\overline{u}$	m s^{-1}	Depth-averaged velocity in longitudinal direction
$\overline{u}_{cr}$	m s^{-1}	Critical depth-averaged velocity in longitudinal direction
$q_{b,c}$	kg s^{-1} m^{-1}	Bed load transport rate, current
r_u	–	Relative turbulence in longitudinal direction
Re_*	–	Particle Reynolds number
ρ_w	kg m^{-3}	Water density
ρ_s	kg m^{-3}	Sediment density
σ	–	Standard deviation
t	s	Time
τ	N m^{-2}	Bed shear stress
τ'	N m^{-2}	Grain bed shear stress
τ_{cr}	N m^{-2}	Critical bed shear stress
θ	–	Dimensionless bed shear stress (Shields parameter)
θ'	–	Dimensionless grain bed shear stress
u	m s^{-1}	Velocity in longitudinal direction
u_*	m s^{-1}	Shear velocity in longitudinal direction
u'	m s^{-1}	Turbulent intensities in longitudinal direction
υ	m s^{-1}	Kinematic viscosity
w_s	m s^{-1}	Settling velocity
x	m	Longitudinal coordinate
y	m	Lateral coordinate
γ	–	Relative standard deviation
z	m	Vertical coordinate, height above the bed
z_0	m	Roughness length

List of Abbreviations

ADV	Acoustic Doppler Velocimeter
ADVP	Acoustic Doppler Velocimeter Profiler
CBL	Collected bed load
CFE	Constant flow experiment
GPC	GoPro camera
MPM	Meyer-Peter and Müller transport formulation
OP	Orthomosaic photos
PPT	Parts-per-thousand
PS	Pressure sensor
SNR	Signal-to-noise ratio
SAFE	Slowly accelerating flow experiment
WP	Wong and Parker transport formulation

1

Introduction

In the Netherlands, the coastlands act as the principal protection against the sea. These areas typically consist of sandy material, which is a common type of coast globally (Luijendijk et al., 2018). Over time, sediment transport can cause significant changes to the physical shape and structure of the coastal system. Without human interventions, the Dutch coast would be eroding due to an imbalance in the sediment budget of the coastal zone (Brand et al., 2022). This imbalance is the result of sea level rise, land subsidence, and a decreasing input of sediment from marine sources and rivers over time (Beets and Van Der Spek, 2000; Van der Meulen et al., 2007; Van der Spek and Lodder, 2015).

Effective coastal management strategies are needed to protect the Dutch coastline against erosion and flooding. In the Netherlands, the preferred coastal management strategy is sand nourishment, which follows the principle: ”soft where possible, hard where necessary” (Ministerie van Infrastructuur en Milieu, 2015, p.39). Sand nourishment represents a soft approach to coastal management, involving the mechanical placement of sand to create a non-permanent, more natural structure that requires regular maintenance –i.e., re-nourishment– to protect coastlines against erosion and flooding. This differs from the latter approach, where man-made structures, such as concrete seawalls and rock revetments, protect coastlines against erosion and flooding. Figure 1.1 shows a beach along the North Sea in summer.

Figure 1.1: Shells on a beach along the North Sea in summer. Credit: Jan Marijs.

Sand nourishments have become larger in scale and more complex over the last 70 years (Brand et al., 2022). Nourishment volumes have significantly increased (ICES, 2016), and the demands for nourishment are expected to further increase in the coming decades due to the rising sea levels (Deltares, 2020). However, (suitable) sand is relatively rare. With the increasing demand for this resource, the global demand for natural sand will rapidly approach the point at which it will exceed the rate of natural renewal (Peduzzi, 2014; Bendixen et al., 2021). The availability of sufficient sand against reasonable extraction costs will become subject to increasingly more pressure. For instance, De Jong (2016) reasons that the volume of extractable sand on the Dutch continental shelf may be exhausted within decades due to the growing number of annual nourishments in the Netherlands. In this context, it becomes more crucial to have more reliable sediment transport predictions to help manage the placement of sand.

The sedimentary environments of today are complex systems that feature a combination of different materials, including carbonate shells (Gutiérrez et al., 2003). Bivalve shells from molluscs have a wide global distribution and are commonly found in many marine habitats, including intertidal zones, shallow water, and deep sea (Smaal et al., 2019). A bivalve shell comprises two valves joined at a tip known as the umbo. Over time, when shells die, the action of water causes the shell halves to separate into two pieces and smaller fragments (Dey, 2003; Newell et al., 2007). Compared to the original composition of the beach, nourished beaches typically exhibit higher concentrations of shell valves and shell fragments (e.g., Peterson et al., 2000; Van der Wal, 2000). This emphasizes the importance of understanding the influence of shells on sediment transport and whether shells can positively contribute to effective coastal management strategies.

Here we introduce the motivation for this research. The following section provides the problem statement. Section 1.2 gives a brief introduction to sediment-shell interactions. Section 1.3 states the research objective, followed by the scope of the research in Section 1.4. Finally, Section 1.5 presents a brief outline of the report.

1.1. Problem statement

The sandy marine environment is a distinctive and ever-changing ecosystem (McLachlan and Defeo, 2018). Large quantities of mollusc shells can be found on the ocean floor (ICES, 2016). These shells serve as protective barriers and consist mainly of calcium carbonate (Kaplan, 1998). Unlike siliciclastic sediments, typically brought in from external sources, the carbonate structures that form the shells are often generated within the sandy marine environment itself (Kennedy et al., 1969). Moreover, the shape, size, and density of carbonate shells and shell fragments differ significantly from siliciclastic grains. Both shells and fragments are characterized by their plate-like, irregular, and angular shapes, while sands mainly comprise roughly spherical quartz grains (Soulsby, 1997). Furthermore, due to their lower density and distinctive shape and size (i.e., a large horizontal cross-sectional area and a small cross-sectional area exposed to the flow), shells have a lower settling velocity and require a larger erosion velocity compared to siliciclastic grains (Miedema and Ramsdell, 2011). These characteristics also govern sediment entrainment thresholds (Komar and Clemens, 1986), determining whether the sediment is carried as bed load or suspension load (Van Rijn, 1997). Although much of the research on sediment transport has centered on siliciclastic grains, the contribution of carbonate shells and shell fragments to sand transport is less well-known.

Previous research on the threshold of motion of a sediment-shell mixture has primarily focused on shell debris and random shapes (e.g., Prager et al., 1996; Paphitis et al., 2002; Rieux et al., 2018; Silva et al., 2023). However, mollusc shells show a wide range of sizes and shapes, which implies a difference in the entrainment of shells. Several studies have investigated the threshold of motion for intact mollusc shells through experiments on the movement of single shell valves under unidirectional flow. These studies have explored the effects of shell position (Dey, 2003; Fick et al., 2020), as well as the effects of umbo orientations on drag and their incipient motion condition (Diedericks et al., 2018). Furthermore, Olivera and Wood (1997) show that circular or rectangular shells are less susceptible to entrainment compared to elongated shells. While a significant amount of research has been devoted to studying the threshold of motion of shells, there has been relatively little exploration of the relationship between sediment transport and shells of different shapes and sizes.

Sediment transport refers to the displacement of sediment particles within a distinct plane over a defined time frame (Bosboom and Stive, 2023). The water flow exerts a shear stress on the bed surface. Bed shear stress is commonly expressed in terms of a friction coefficient (c_f), the water density (ρ_w),

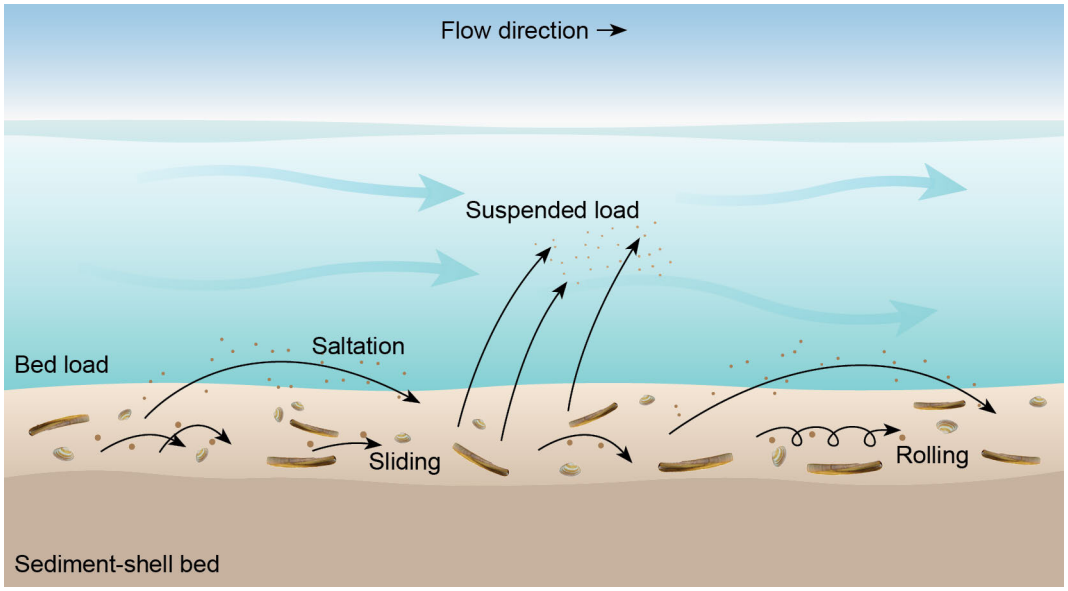

Figure 1.2: Schematic of a sediment-shell mixture bed configuration considered in this study, defining sediment transport modes as per Bagnold (1956).

and the depth-averaged velocity ($\bar{u}$). Alternatively, it can be expressed in terms of the shear velocity (u_*):

$$\tau = c_f \rho_w \bar{u}^2 = u_*^2 \rho_w \tag{1.1}$$

Bed shear stress initiates sediment transport when it surpasses the critical shear stress required to overcome the stabilizing forces (Van Rijn, 1993). In general, two main modes of sediment transport can be distinguished: (i) bed load transport and (ii) suspended load transport (Bagnold, 1956). Bed load transport involves rolling, sliding, and saltation (hopping) of grains in close contact along the bed. With suspended load transport, smaller particles are uplifted by the flow of the fluid and remain suspended due to the turbulence of the fluid (Figure 1.2).

The presence of intact shells and larger fragments can either stabilize sediment through armoring or enhance sediment transport by scouring. The formation of an armor layer is driven by the winnowing of finer sediment particles by the action of water, which gradually exposes coarser particles on the surface of the bed. As shells are more difficult to erode, they may also be able to provide a similar armoring effect against sand erosion (Miedema and Ramsdell, 2011). The smaller sediment grains are hidden from the flow by larger, more exposed shell valves and fragments. This process is also known as the hiding-exposure effect, which complicates the calculation of bed load transport, as it increases the threshold of motion for smaller grains (McCarron et al., 2019). Only a limited number of studies have explored the direct impact of shell material on bed load transport by modifying bed roughness (Gutiérrez et al., 2003; Kumagai and Nakajima, 2012). In a recent study, Cheng et al. (2021) researched the effects of a sediment-shell mixture on the development and movement of sand ripples. As shell content increases, sand ripple dimensions are reduced, and ripple migration rates slow down (Cheng et al., 2021). In essence, this limits the rate of bed load transport. Although shells are commonly found in the sandy marine environment, there has been limited research into quantifying the bed load transport of sand in the presence of shells of varying sizes and shapes.

As the demand for sand nourishment continues to increase globally, there is a corresponding rise in pressure on available sand against reasonable extraction costs. Therefore, it is becoming increasingly important to have more accurate predictions on the behavior of sand nourishments over time to understand their effectiveness. However, the presence of shells complicates these predictions. Despite extensive research on carbonate shells, their threshold of motion, and sediment transport of a sediment-shell mixture, there is currently a knowledge gap in terms of:

- Determination of the threshold of motion of sand grains for a bed composition consisting of sandy sediment and shells of different shapes and sizes.
- Quantification of bed load transport for a bed composition consisting of sandy sediment and shells of different shapes and sizes.

1.2. Introduction to sediment-shell interactions

A distinction can be made between two situations: (i) a single isolated shell (Section 1.2.1), and (ii) a cluster of shells (Section 1.2.2). A comparison between these two situations can be made by looking at a horizontal cross-section of vegetation at various elevations. In this analogy, a single isolated shell corresponds to the trunk of a plant, while a cluster of shells corresponds to the shoot (Folkard, 2011).

1.2.1. A single isolated shell

In the simplest case, a single valve of a *Spisula subtruncata* shell is resting on the seabed (Figure 1.3a). This specific situation represents a low shell content where shells are sparsely distributed on the bottom. The shell is assumed to be in a convex upward condition in its most favorable orientation, i.e., with the umbo also pointing in the downstream direction (e.g., Dey, 2003; Silva et al., 2023). The isolated shell will modify the flow conditions in the immediate surroundings, as described by previous studies (e.g., Brayshaw et al., 1983; Nowell and Jumars, 1984; Verhaegen et al., 2019). As the flow encounters the leading edge of the shell, it is directed toward the bed immediately in front of the shell. This facilitates scour of sediment particles in front of the shell (Figure 1.3c). Additionally, the shell presence reduces the available cross-sectional fluid area, resulting in an acceleration of the flow (contracting flow lines) and scouring of sediment particles over and around each side of the shell (Figure 1.3d). This phenomenon is known as 'blockage'. Simultaneously, the presence of the shell creates a wake structure behind it, leading to reduced velocities on its trailing edge (Figure 1.3c). This effect is known as 'sheltering'. At the edge of the wake, differences in velocity give rise to the formation of a mixing layer characterized by intense shear stresses and subsequent turbulence. In addition to modifying the flow conditions, the presence of a shell valve results in sediment coverage, reducing the amount of sediment available for transport. Figure 1.3b presents a comparison of the flow velocity, sediment available for transport, and bed elevation.

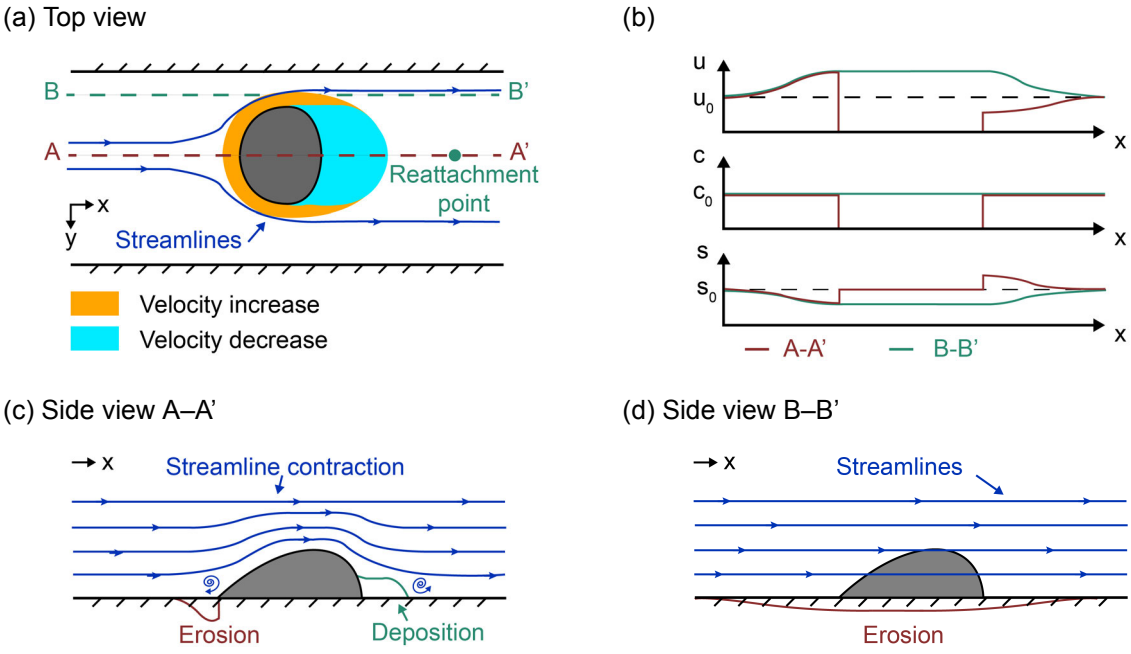

Figure 1.3: Schematic of a single isolated *Spisula subtruncata* shell valve: (a) top view, (b) flow velocity u, sediment available for transport c and bed elevation s, (c) side view A-A', and (d) side view B-B'.

Here, a single valve of a *Ensis leei* shell is resting on the bed in a horizontal flat position (Figure 1.4a). In contrast to the *S. subtruncata* shell, the *E. leei* shell has an elongated, slender, and straight shell shape. The distinct shape characteristics allow for a more streamlined water flow over the shell, following its shape without significant disruptions (Figure 1.4c-d), with minimal blockage of the flow. This reduces flow separation, minimizes increased shear stress, induces a relatively lower degree of turbulence, and hence less scour can be expected. Additionally, the *E. leei* shell covers a greater area of the sediment bed, reducing the sediment available for transport compared to the *S. subtruncata* shell (Figure 1.4b).

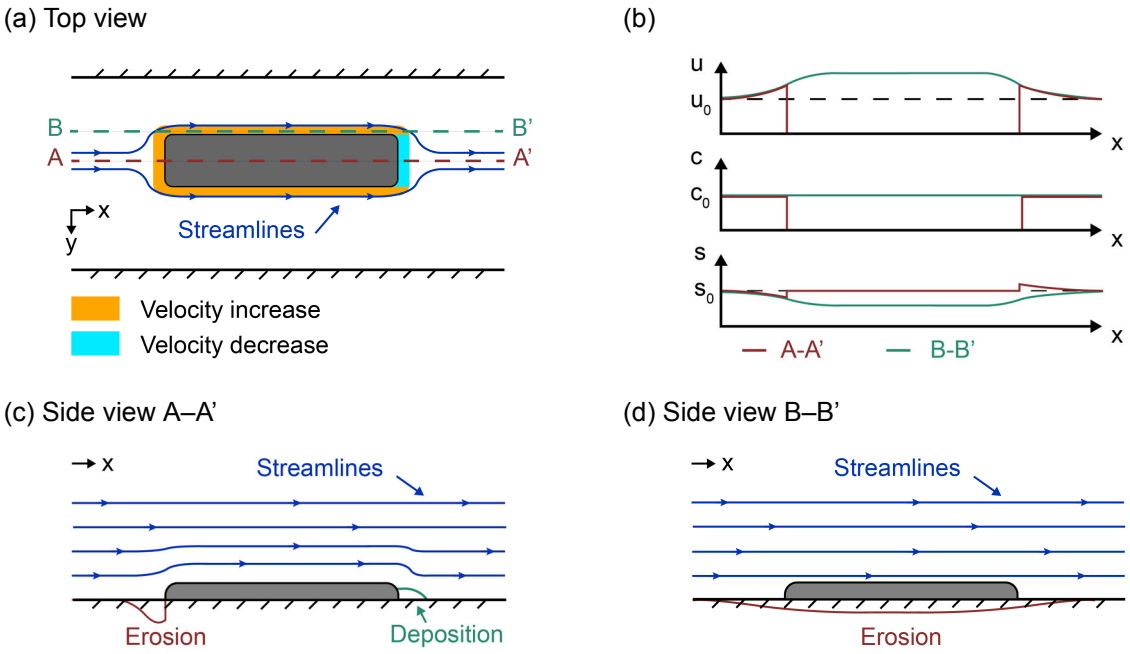

Figure 1.4: Schematic of a single isolated *Ensis leei* shell valve: (a) top view, (b) flow velocity u, sediment available for transport c and bed elevation s, (c) side view A-A', and (d) side view B-B'.

1.2.2. A cluster of shells

A more complex situation arises when multiple shells are positioned close to each other. The interaction between shells can create more complex flow patterns, which have a more significant impact on the immediate surroundings than a single shell (Nowell and Jumars, 1984). This situation represents a high shell content, in which shell cover is significant. Detailed measurements are necessary to accurately characterize the flow within and around a cluster of arbitrarily shaped objects when closely spaced (Brayshaw et al., 1983). In a recent study, Gijón Mancheño et al. (2021) explored the effect of vertical cylindrical structures on currents and showed that the relative significance of the two processes, i.e., blockage and sheltering, varies and relies on factors such as the prevailing flow conditions and the size and spacing of the structures. Similarly, in the case of a cluster of shells, one can anticipate changes in blockage. The collective presence of shells can act as a barrier, leading to enhanced sheltering and decreasing the available flow velocity near the bed to move sand grains. Conversely, Nowell and Church (1979) show that turbulence levels in a fluid surrounded by objects arranged in a regular pattern are higher compared to an absence of objects. The turbulence levels depend on the density of objects covering the bed's surface area (Friedrichs et al., 2000, 2009). Moreover, velocities and turbulence levels near the bed are influenced by the density of roughness elements.

The distance between roughness elements on a surface is commonly referred to as roughness spacing. Morris (1955) defined three types of roughness spacing: (i) skimming flow, (ii) wake interaction, and (iii) isolated roughness (Figure 1.5). Isolated roughness refers to individual roughness elements that are sparsely distributed on a surface, allowing for significant spacing between them. This large spacing allows for a relatively uninterrupted flow between elements, and the hydraulic effects are dissipated before the flow encounters the next roughness element, reducing the overall impact on the flow field. However, it is important to note that there may still be influences from the wake. As the ratio of the height (H) of the roughness element to the characteristic width (W) increases, wakes generated on the leading- and trailing edge begin to interact with each other, i.e., wake interference. This flow accompanies turbulent mixing and intense turbulence. If the H/W ratio continues to increase, this results in the formation of trapped eddies within the gaps between the elements, and the flow is shifted to the top of the roughness elements, i.e., skimming flow. (Morris, 1955; Perry et al., 1969). For isolated roughness, Perry et al. (1987) suggested that eddies are injected into the flow above the crest of the roughness elements, while for skimming flow, eddies maintain trapped between the roughness elements.

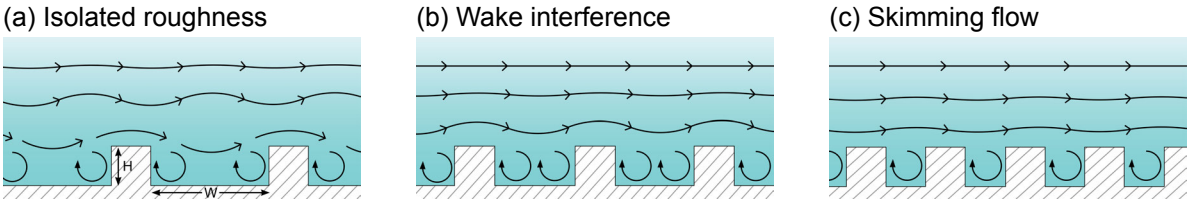

Figure 1.5: The different types of roughness spacing with increasing H/W ratios as per Morris (1955).

1.3. Research objective

This research aims to provide insights into the complex interaction between bivalve shells and their physical environment. To accomplish this, multiple disciplines –e.g., sediment dynamics, fluid dynamics, ecology, etc.– are brought together. To achieve the research goal, an experimental flume study was carried out to investigate the effects of bivalve shells on sediment transport under unidirectional flow. This study attempts to answer the following research question:

How do bivalve shells of different shapes and sizes influence current-driven sand transport?

The study focuses on (i) identifying the important parameters of current-driven sand transport; (ii) evaluating the effect of bivalve shells on the threshold of motion of sand grains; and (iii) evaluating the effect of bivalve shells on bed load transport (rates). The research will answer three sub-questions derived from the main research question, which are:

1. What are the important parameters of current-driven sand transport, and how can they be quantified in an experimental flume study?
2. What is the influence of bivalve shells on the threshold of motion of sand grains?
3. What is the influence of bivalve shells on bed load transport (rates)?

This research aims to enhance existing sediment transport formulations by determination of the threshold of motion and quantifying bed load transport of a bed composition consisting of sandy sediment and bivalve shells of different shapes and sizes. The ultimate goal is to incorporate the improved formulations into predictive models. The resulting models will enhance the coastal management toolbox, leading to more effective nourishment management strategies over time.

1.4. Scope of the research

The research is centered around the transport of a sediment-shell bed composition in water under varying forcing conditions. It involves two species of bivalve shells –*Ensis leei* and *Spisula subtruncata*– and studies forcing conditions ranging from below to above the threshold of motion of sand grains. The experimental flume setup enables precise control of the conditions –e.g., water depth, salinity, temperature– across multiple experimental runs.

However, this research does not cover all aspects of the complex sediment-shell interaction, nor does it cover all shell types or forcing situations, because only limited knowledge is available on the effects of bivalve shells on the threshold of motion of sand grains, let alone on the quantification of bed load transport in the presence of bivalve species. Therefore, only two shell species are included in this study due to time limitations. Simplifications are made possible through the use of an experimental flume setup. The scope of this research is listed below:

- **Selection of shell species**

  This research considers two different bivalve shell species: *Ensis leei* and *Spisula subtruncata*. These species exhibit a wide distribution in size and shape –elongated in comparison with rounded– while having a similar shell thickness (Table A.3 and Figure A.3 in Appendix A). Moreover, both species are abundant along the Dutch shoreline (Gittenberger and Loon, 2011; Naturalis Biodiversity Center, 2022).

- **Sediment-shell bed configurations**

  Shells can make up a significant share of sediment composition (by volume) in environments where they are highly abundant, ranging from 20% to 70% (Soulsby, 1997). In previous research, Cheng et al. (2021) showed that shell percentages of 10%-15% already reduced ripple sizes significantly, and above 20%, the ripples were almost entirely absent. In essence, this limits the rate of bed load transport. Therefore, this research considers the following range of volumetric percentages of shells: 0%, 10%, and 20%. The experimental control (0% shells) was composed only of sandy North Sea sediment, which is the focus of this research. A limit has been set on the number of bed configurations due to time limitations.

- **Hydrodynamic forcing conditions**

  This research aims to provide insights into the complex interaction between bivalve shells and their physical environment. The emphasis is on sand transport in deeper waters, where the effect of waves is limited. To this extent, this research focuses on current-driven sediment transport in different transport stages: just below to well above the threshold of motion of sand grains. Although a complementary set of experiments was conducted to examine the impact of waves, that will not be discussed here.

- **Experimental flume setup**

  To some degree, the experiment is limited to the dimensions and possibilities within the flume facility. For instance, the water depth is limited to 40 cm, and only depth-averaged velocities up to a maximum of 0.45 m s^{-1} can be generated (Bouma et al., 2007). In combination with waves (generated by a wave pedal), the maximum velocity that the conveyer belt system can generate is further restricted. On the other hand, using an experimental flume setup allows for the conditions to be controlled over different experimental runs over a long period.

- **Selection of data to analyze**

  The experimental flume study contains a broad range of hydrodynamic forcing conditions, resulting in the collection of a substantial amount of data from various measurements. Due to time limitations, the focus will be on the camera footage, Acoustic Doppler Velocimeter data, and sediment collected from the bed load transport. The use of the remaining data, e.g., Acoustic Doppler Velocimeter Profiler data and orthomosaic photos, will be further elaborated on in the recommendations.

1.5. Thesis outline

Chapter 1 outlines the motivation and knowledge gaps for this study. Chapter 2 states the methodology used to research the influence of bivalve shells on current-driven sand transport, and Chapter 3 presents the study's results. In Chapter 4, a discussion of the findings is presented, and Chapter 5 summarises the main conclusion and offers recommendations for further research. The appendices provide additional details on the materials and instruments used in the experimental flume setup (Appendices A-B), a summary of all experimental runs (Appendix C), a derivation of the threshold of motion of sand grains and existing knowledge (Appendix D), a description of the data processing (Appendix E), and supporting figures (Appendix F).

2

Methodology

This research aims to provide insights into the complex interaction between bivalve shells and their physical environment. To achieve this, an experimental flume study was conducted to measure the onset of motion of sand grains and the resulting bed load transport. The choice of this method is based on its ability to examine specific aspects of the natural phenomenon's progression, and the controlled conditions implemented in various experimental runs enable other researchers to replicate the study (Gomez, 1978).

Here we introduce the methodological approach. The following section explains the experimental setup. Section 2.2 describes the two experiments performed in this study. Finally, the chapter concludes with a description of the data analysis (Section 2.3).

2.1. Experimental setup

This section describes the entire setup of the experiment. Starting with an overview of the main flume dimensions. This is followed by the flume setup (Section 2.1.2). The section then concludes with a description of the sediment-shell bed composition in Section 2.1.3.

2.1.1. Flume dimensions

Flume experiments have been performed in the racetrack flume facility at the NIOZ Royal Netherlands Institute for Sea Research in Yerseke, the Netherlands. The racetrack flume is approximately 17.5 m in length and 3.25 m in width, with a flow channel of approximately 0.60 m wide (Figure 2.1a). A conveyor belt system, located on the opposite straight side of the test section, can generate unidirectional flow with velocities up to 0.45 m s^{-1} (Bouma et al., 2007). The speed of the conveyor belt can be adjusted, allowing for the flow velocity to be controlled with high precision. To minimize the effects of secondary flows, the bends have been divided into different compartments by turning vanes. Additionally, the flow is diffused by two stacks of diffusion tubes (⌀ 20 mm) which act as collimators. Using a flume of sufficient size allowed us to carry out experiments at full scale, thereby mitigating the risk of errors that could arise from scaling.

2.1.2. Flume setup

The flume was filled with fresh water up to a water depth of 0.35 m. Approximately 200 kilograms of salt was dissolved in the freshwater. The addition of salt was monitored using a Salinity Tester from Hanna Instruments (HI98319 Marine Salinity Tester) until it reached approximately 30 parts-per-thousand (PPT), approximately 1023 kg m^{-3}. This salinity level was chosen to simulate natural environments like the Oosterschelde and Wadden Sea, the Netherlands. In these environments, salinity typically falls within 20 to 30 PPT (Van Aken, 2008). It is worth noting that this range is lower than the salinity commonly found in the open ocean (35 PPT). The salinity was tested and adjusted as needed before each experimental run to maintain the desired level.

At the far end of one of the straight sections is a 2.00 m long and 0.60 m wide test section, with a transparent side window for direct observation (Figure 2.1b). The test section has a height-adjustable bottom that allows sediment placement down to a depth of 0.25 m. A sediment tray, measuring 160.5

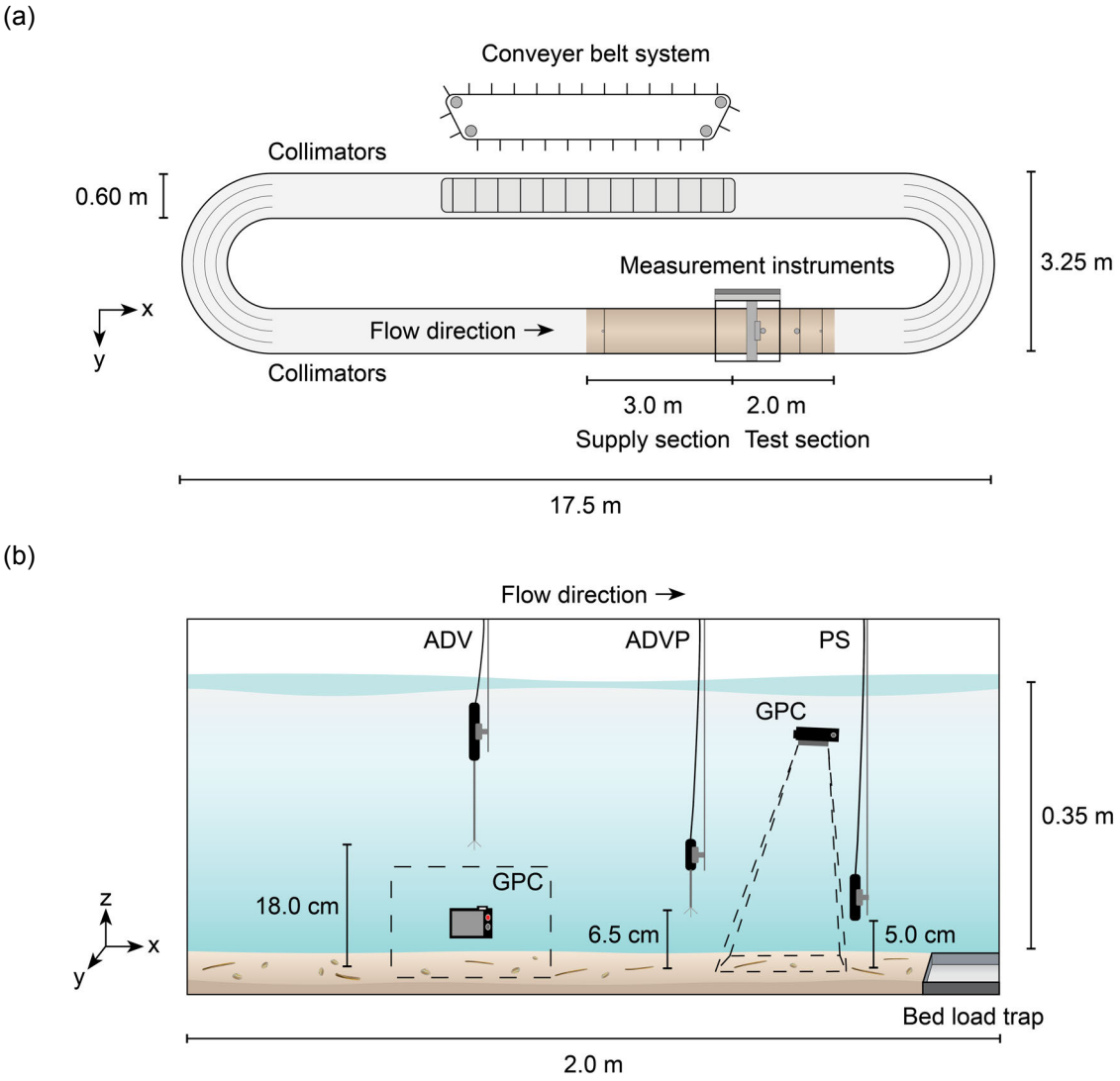

Figure 2.1: (a) The top view of the racetrack flume. (b) A side view of the 2.0 meters long test section showing the measurement instruments considered in this study: Acoustic Doppler Velocimeter (ADV), Acoustic Doppler Velocimeter Profiler (ADVP), Pressure Sensor (PS), and GoPro Camera (GPC).

cm × 57.5 cm × 25.5 cm (L × W × H) was placed into the test section. The openings between the flume walls and the sediment tray were filled with foam strips to prevent a sediment sink from developing. At the downstream end of the test section, a bed load trap was also installed and had a dimension of 58.5 cm × 20.0 cm × 12.0 cm (L × W × H). On the top side, a 2.0 cm edge was applied on each side to lift out the tray when needed. This left a 16.0 cm gap in width for sediment to 'fall' through. Finally, the remaining gap between the sediment tray and the end of the lowered floor of the test section was closed off by a plywood plate.

Within the test section, a Nortek Vectrino Acoustic Doppler Velocimeter (ADV), mounted on a 3D positioning system, was used to record flow velocities at a frequency of 25 Hz. The probe head was positioned at the center of the flume. To obtain the depth-averaged velocity, the probe head was placed at the height of 0.37 × the water depth plus an additional 5 cm of blanking distance above the bed surface (Vanoni, 1941). A Nortek Vectrino Acoustic Doppler Velocimeter Profiler (ADVP) recorded three-dimensional flow velocities near the bed. The probe head was positioned approximately 6.5 cm above the bed. With a blanking distance of 4 cm, it measured from −0.5 cm below to 2.5 cm above the bed surface, using 16 cells (2.0 mm interval) while recording at 25 Hz. Two pressure sensors (PS) were also used. One was located at the beginning of the sediment supply section, and a second sensor was placed at the end of the test section. Both pressure sensors were positioned approximately

5 cm above the bed surface and recorded at 25 Hz. Before each experimental run, the positions of the measurement instruments were checked using either the distance check (ADV and ADVP) or a meterstick. Lastly, two GoPro HERO4 Session cameras (GPC) recorded a top- and side view of the test section. Appendix B contains a comprehensive list of all the measurement instruments used in the experiment, along with their corresponding manufacturers and serial numbers.

2.1.3. Sediment-shell bed composition

North Sea sandy sediment was used during the experiment. The particle size of the sediment was determined by laser diffraction, using a Mastersizer 2000 from Malvern Instruments, following McCave et al. (1986). The median grain size was roughly 348 µm. In addition, the sand could mainly be classified as medium sand (Table A.1 and Table A.2 in Appendix A).

For this study, two distinct species of bivalve shells were chosen, specifically *Ensis leei* and *Spisula subtruncata*. In July 2022, *E. leei* and *S. subtruncata* shells were obtained from Meromar Seafoods B.V. in Harlingen, the Netherlands. These shells were not empty, as they still had some meat residue, so they were subjected to a cleaning process. This involved soaking the shells in a solution of enzyme-based detergent (i.e., biotex) for at least two weeks, after which they were rinsed. A random sample was taken from the stockpile of shells to establish the average dimensional properties of the shell valves. Measurements were taken following Vanoni (1975) in which he defined the length, width, and height as the longest, intermediate, and smallest dimensions along three mutually perpendicular axes. The shell species reflect a wide distribution in size and shape –elongated in comparison with rounded– while having a similar shell thickness (Figure 2.2). The shell species had a significant difference in weight, as the mean weight of *E. leei* shells was twice that of *S. subtruncata* shells (Table A.3 in Appendix A). Additionally, a pycnometer was used to measure the density of the shell valves, shell fragments, and North Sea sandy sediment. The results indicated that the density of the North Sea sandy sediment corresponded to typical density values for sediment (i.e., 2650 kg m^{-3}). Additionally, the bulk density of the carbonate shells was considerably lower than the bulk density of the sediment (Figure A.4 in Appendix A). This supports Soulby's claim that the presence of shells reduces the bulk density of the sediment by diluting the quartz fraction (Soulsby, 1997).

For the sediment-shell mixture, the sediment and shell quantities were determined using different-sized buckets (either 1 or 20 L of size). Three types of sediment-shell mixtures were used in the experiments. First, a mixture of sand and shells containing both the *E. leei* and *S. subtruncata* species together (Table 2.1). Secondly, a mixture of sand and shells containing only the *E. leei* species (Table

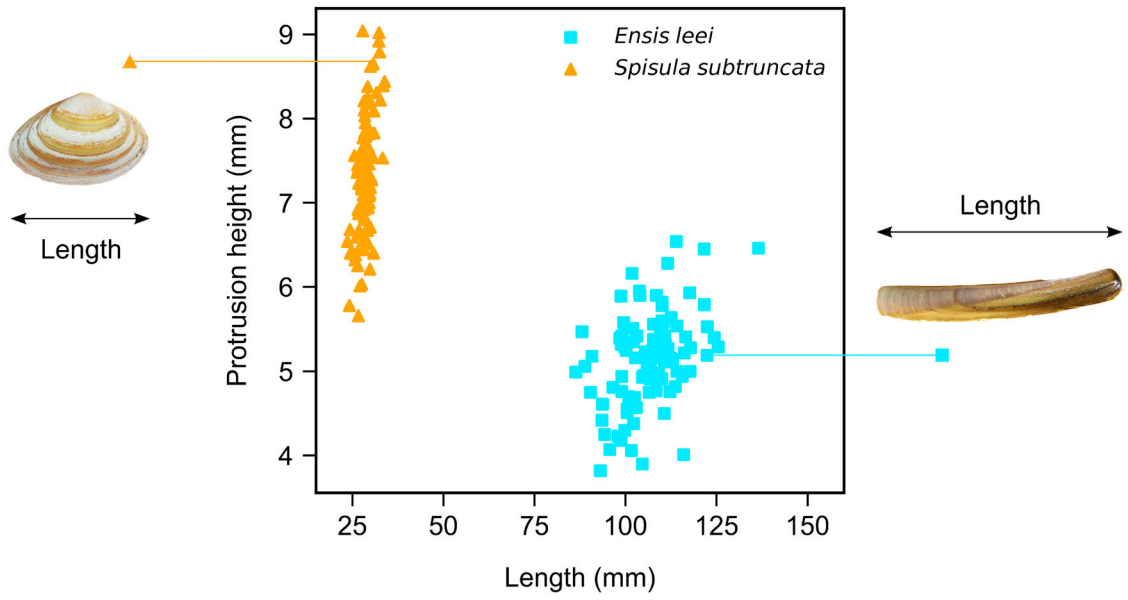

Figure 2.2: Shell valve protrusion height versus length, along with the bivalve shell species used in the experiment. Credit: Björn Wylezich.

Table 2.1: Sediment-shell bed composition for different shell contents, containing both *Ensis leei* and *Spisula subtruncata* shells, hereafter this bed composition will be indicated with Mixture. All quantities are given concerning a 100 L batch.

Shell content (%)	Sediment (L)	*Ensis leei* (L)	*Spisula subtruncata* (L)	Fragments (L)
0	100	0	0	0
5	95	2.5	2.5	2
10	90	5	5	4
20	80	10	10	8
50	50	25	25	20

Table 2.2: Sediment-shell bed composition for different shell contents, containing only *Ensis leei* or *Spisula subtruncata* shells. All quantities are given concerning a 100 L batch.

Shell content (%)	Sediment (L)	*Ensis leei* / *Spisula subtruncata* (L)	Fragments (L)
0	100	0	0
10	90	10	4
20	80	20	8

2.2). Lastly, a mixture of sand and shells containing only the *S. subtruncata* species (Table 2.2). Since the shells cannot be packed as densely as the sand, fragments of shells were added to the mixture to compensate for these packing differences. The mixture comprised an equal proportion of shell grit less than 2 mm and one ranging from 2-4 mm. The experimental control with 0% shells consisted only of North Sea sandy sediment, while subsequent mixtures included varying amounts of shell material. The study examined shell volumetric percentages of 10% and 20%. Additionally, two mixtures containing both shell species with a volumetric percentage of 5% and 50% shells were tested.

The sediment-shell mixtures were produced in batches of 100 L. Each sediment-shell configuration required an average of 2 batches (200 L) to perform the experiments. Both batches were produced in series on the same day to prevent inconsistencies. All elements of the mixture were loaded into a portable concrete cement mixer to guarantee sufficient mixing. Subsequently, the mixture was mixed for approximately 1-2 minutes, after which the mixture appeared to be well-mixed. Mixing for more than 2 minutes was averted to prevent possible abrasion of the shells. Roughly 125 L of the sediment-shell mixture could initially be loaded into the sediment tray. A layer of lightweight foam was applied on the bottom of the tray to reduce the overall weight and volume of material required. On top of the foam layer, a cover plate was used to reduce the sediment tray's height by 15.5 cm, leaving a layer of 10.0 cm for the sediment. The tray has eight attachment points, allowing easy placement and removal using an electric hoist. A thin layer of 2-3 cm of sand was placed in the preceding 2-3 m in front of the test section to guarantee a constant sediment supply throughout the experiment. Additional sediment was stored in a container for later use. Following each experiment, the bed was levelled and thoroughly mixed using a wooden pole equipped with a rake or squeegee. Additionally, before each experimental run, the sediment supply section was reinstated.

2.2. Experimental runs

The study consisted of two separate experiments: (i) a slowly accelerating flow experiment (Section 2.2.1), and (ii) a constant flow experiment (Section 2.2.2). Both experiments consisted of several experimental runs in which the sediment-shell bed composition was altered by changing the volumetric percentage of shell content.

2.2.1. Slowly accelerating flow experiment

This experiment aimed to determine how bivalve shells affect the threshold of motion of sand grains. Three out of the seven motion stages defined by Breusers and Schukking (1969) were selected, namely: (i) a few rolling grains, (ii) frequent movement in several places, and (iii) full bed mobility. The initial bed would be flat to quantify shells' direct effect on sediment stability. The bed load trap was removed, and a plywood plate closed off the end of the lowered floor. According to Van Rijn (1993), sandy sediment with a median grain size of roughly 348 µm is not expected to experience sediment motion below a flow velocity of 0.28 m s^{-1} (Appendix D.3). The starting velocity of each run was set at 0.15 m s^{-1},

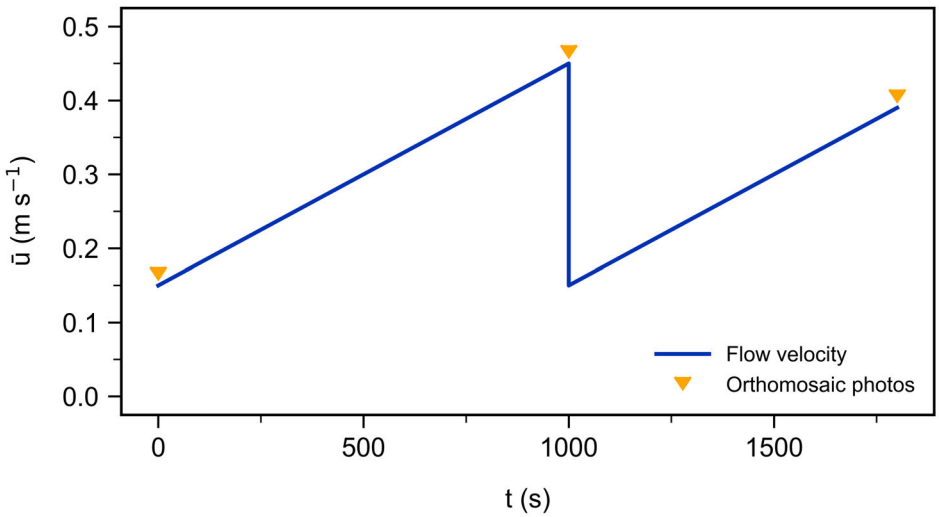

Figure 2.3: Flume flow settings used for the slowly accelerating flow experiment (line), along with the time of capturing of the orthomosaic photos indicated by markers.

increasing with approximately 0.02 m s^{-1} min^{-1} until the final motion stage was observed. The bed, which had been water-worked, was tested again to see if the first motion stage changed following the initial disturbances of the bed. The velocity was reset, and the flow velocity was again linearly increased over time, starting from 0.15 m s^{-1}. One experimental run took approximately 30 minutes (Figure 2.3).

During this experiment, the ADV measured the depth-averaged velocity. The two GoPro HERO4 Session cameras video-recorded the experiment in 1080p video resolution (1920 × 1080 pixels) at 50 frames/second. Visual observations were made of the different motion stages, indicated by showing a coloured paper in view of the side view camera. Moreover, a set of top-view photos of the bed surface were captured over the complete length of the test section at intervals of 5 cm. These photos were taken while the flow was stationary at the experiment's beginning, midpoint, and end (See Figure 2.3). By stitching the multiple individual photos together, orthomosaic photos (OP) could be generated to monitor the evolution of the bed surface.

An overview of all nine experimental runs for this experiment, including the availability of measurement data, is given in Table C.1 of Appendix C.

2.2.2. Constant flow experiment

This experiment aimed to measure the influence of bivalve shells on current-driven bed load transport in different transport stages. Flow velocities below and above the threshold of motion were tested. Once started, the flow velocities were kept constant throughout the entire experimental run. The initial bed would be flat, and the bed load trap would be emptied. One experimental run took 120 minutes (Figure 2.4).

Again, the ADV measured the depth-averaged velocity throughout the experiment. Both GPCs were set on time-lapse mode, capturing a photo once every minute at a 2720 × 2040 pixels resolution. Samples were collected from the bed's top layer at the experiment's beginning and end. Bed load transport rates are typically measured by collecting sediment during a specific time interval or measuring sediment flux. However, the time-averaged values of these rates depend significantly on time intervals due to the non-Gaussian fluctuations observed (Ancey and Pascal, 2020). Ancey and Pascal (2020) found that measurements of time-averaged bed load transport rates can be biased to varying degrees depending on the chosen time interval. Therefore, balancing the trade-off between the level of noise and representatives of time-averaging is essential to accurately estimate bed load transport rates (Ballio et al., 2014). Following the recommendations of Ancey and Pascal (2020), who also conducted flow experiments in a long (19 m) flume, the sampling intervals here have been defined as 30 minutes, 60 minutes, and 120 minutes from the start of the experiment. The flow was halted at the given sampling intervals, and the bed load trap was emptied using a plastic tube as a siphon. The water-sediment mixture was filtered over a 90 µm sieve and collected for later analysis. Lastly, at both

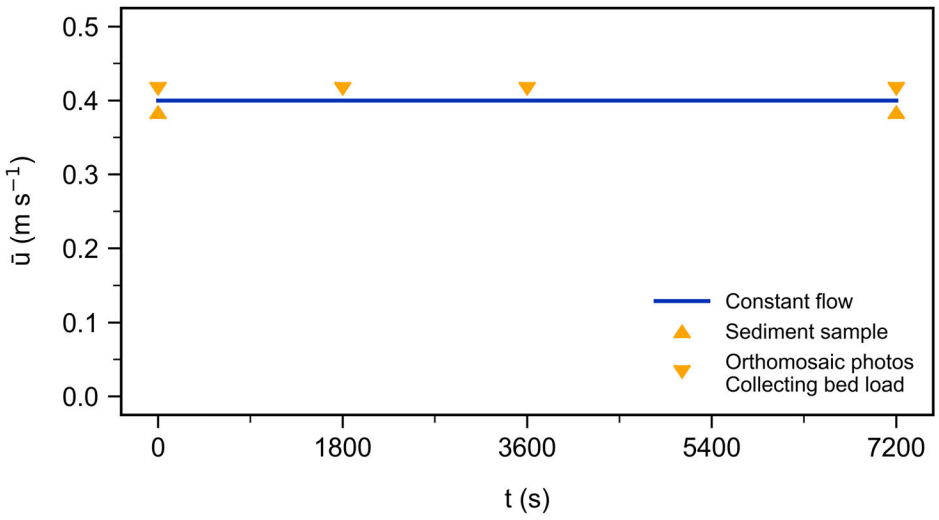

Figure 2.4: Flume flow settings used for the constant flow experiment (line), along with the time of conducting additional measurements indicated by markers. For simplicity, the figure only displays one of the tested flow velocities. In each experimental run, the constant flow velocity varied.

the beginning and given sampling intervals, a set of top-view photos were taken while the flow was stationary. Similarly to the other experiment, these photos were used to generate OP to monitor the evolution of the bed surface over time.

This experiment required the sand to be transported as bed load rather than suspended load. The sand's settling velocity (w_s) must be smaller than the upward turbulent component of the velocity, which is related to the friction velocity (u_*). This led to a criterion for the threshold of suspension of sediment given approximately by $w_s \sim u_*$, the minimum shear stress required for suspension is given by:

$$\tau_{min} = \rho_w w_s^2 \tag{2.1}$$

Following Soulsby (1997), w_s = 0.026 m s^{-1} and τ_{min} = 0.69 N m^{-}2 for the sand used in this experiment.

An overview of all 24 experimental runs for this experiment, including the availability of measurement data, is given in Table C.2 of Appendix C.

2.3. Data analysis

The defined knowledge gap (Section 1.1), in combination with research sub-question 2 and 3, state two clear objectives: (i) determination of the threshold of motion of sand grains for a bed composition consisting of sandy sediment and shells of different shapes and sizes, and (ii) quantification of bed load transport. This resulted in three different data analyses: (i) identifying the threshold of motion (Section 2.3.1), (ii) quantification of bed load transport for a bed composition consisting of sandy sediment and shells of different shapes and sizes (Section 2.3.2), and (iii) characterization of bed load transport (Section 2.3.2).

2.3.1. Estimating the threshold of motion of sand grains

An analysis was conducted to determine the threshold of motion of sand grains for the data from the slowly accelerating flow experiment. The first step involved improving the quality of the GoPro video recordings by applying a combination of enhancements: gamma correction +12.0, brightness -5.0, contrast -1.0, and sharpening +5.0. A timecode was added to the bottom left corner of the video (Figure E.4 in Appendix E.1.1). Following Nortek AS (2020), the ADV data were filtered for minimum correlation values of 70% and a minimum signal-to-noise ratio (SNR) of 10 dB (Table E.1 in Appendix E.1.2). Afterward, observed spikes in the velocity time series were removed by applying two filters: (i) a difference filter set at 0.5 m s^{-1}, and (ii) a hard threshold filter discarding velocities below 0.0 m s^{-1} and above 0.7 m s^{-1} (Table E.2 in Appendix E.1.3).

The threshold of motion was visually derived from the GoPro video recordings. Visual observations made during the experiment were used as an initial indication. Since it was not possible to switch on the ADV and GPC at the same time, the time stamps of the ADV and GoPro videos were matched by examining the experiment's start and end points, when the belt was switched on- and off.

For each motion stage, the depth-averaged velocities were derived from the ADV measurements by taking the median over the 10 seconds preceding and the 10 seconds after the identified threshold of motion. The selection of a 20-second window prevented the filtering out of large turbulent fluctuations while still allowing for a sufficient time window to obtain an accurate velocity measurement.

The depth-averaged velocity alone is insufficient to provide a complete description of the threshold of motion. This is because the bed shear stress, which determines the initiation of motion, depends on the depth-averaged velocity and bed roughness, i.e., friction coefficient (Equation 1.1). Nezu and Nakagawa (1993) established a relationship between the turbulence intensity (u') and the shear velocity (u_*):

$$\frac{u'}{u_*} = 2.30 \exp\left(-\frac{z}{h}\right) \tag{2.2}$$

where h is the water depth and z is the height above the bed. At a specific height above the bed, the right-hand side of Equation 2.2 can be expressed as a constant value (K). By rewriting Equation 1.1 and Equation 2.2, the relationship between the relative turbulence and the friction coefficient can be expressed as:

$$u_* = \sqrt{\frac{\tau_b}{\rho_w}} = \sqrt{c_f}\bar{u} \quad \rightarrow \quad \frac{u_*}{\bar{u}} = \sqrt{c_f} \quad \rightarrow \quad r_u = \frac{u'}{\bar{u}} = K\sqrt{c_f} \tag{2.3}$$

Hence, in addition to the depth-averaged velocity, the turbulence intensity was determined to obtain a complete description of the threshold of motion. Turbulence intensity is defined as the square root of the average of the velocity fluctuations. The relative turbulence (r_u) can be determined by considering both the depth-averaged velocity and turbulence intensity. Relative turbulence refers to the degree of disturbance in water caused by various factors such as the presence of obstructions and variations in fluid flow velocity (Sentker and Riess, 1999). It is a useful measure since it can provide insight into bed roughness, i.e., friction coefficient. Together, the depth-averaged velocity and friction coefficient allow for the determination of the bed shear stress using Equation 1.1, and subsequently the dimensionless bed shear stress (Shields parameter) using Equation D.1.

The depth-averaged flow velocity can be estimated assuming a logarithmic velocity profile:

$$\bar{u} = \frac{u_*}{\kappa} \ln\left(\frac{z}{z_0}\right) \tag{2.4}$$

where κ is the von Kármán constant (0.41), z is the height above the bed ($0.37h$), and z_0 is the roughness length. The roughness length is given as:

$$z_0 = \frac{k_s}{30} \tag{2.5}$$

where k_s is the Nikuradse current-related grain roughness, which is assumed to be equal to the grain diameter at the 90^{th} percentile (d_{90}) following Van Rijn (1993). The relationship between the depth-averaged velocity and turbulence intensity can be approximated by combining Equation 2.2 and Equation 2.4.

2.3.2. Quantification and characterization of bed load transport

To quantify bed load transport, an analysis was performed using the ADV data and the collected bed load from the constant flow experiment. Again following Nortek AS (2020), the ADV data were filtered for minimum correlation values of 70% and a minimum SNR of 10 dB (Table E.3 in Appendix E.2.1). Afterward, observed spikes in the velocity time series were removed (Table E.4 in Appendix E.2.2). The depth-averaged velocity for each sampling interval was determined by averaging over the entire interval. Determination of the depth-averaged velocity for each sampling interval was necessary since the conveyer belt system revealed slight variations (0.00–0.02 m $s^{-}1$) in the flow velocity after switching on- and off between the sampling intervals.

The collected bed load underwent a drying process at a temperature of 60°C until fully dry, which took roughly 8-10 days per sample. Once completed, the dry weight of the bed load was measured. Next, the bed load was sieved through a 1 mm sieve, and the weight of each fraction was determined. A 1 mm sieve was selected to allow sand grains to fall through while blocking the larger shell fragments and valves. The measured dry weights were divided by the interval time and the flume width to obtain the transported bed load rate ($q_{b,c}$) in kg s^{-1} m^{-1}. It is essential to mention that the flume width (60 cm) is slightly larger than the width of the bed load trap (58.5 cm). Lastly, a sample was taken from the bed load fraction smaller than 1 mm to obtain a more detailed understanding of the bed load transport. The particle size of the fraction was determined by laser diffraction, using a Mastersizer 2000 from Malvern Instruments.

Numerous (semi-)empirical formulations for bed load transport exist, such as those proposed by Meyer-Peter and Müller (1948), Einstein and Banks (1950), Bagnold (1966), and Van Rijn (1984). In this study, a bed load transport predictor by Meyer-Peter and Müller (MPM) is utilized (Equation 2.6). Additionally, a re-analysis of the MPM formulation given by Wong and Parker (2006) (WP), is implemented (Equation 2.7):

$$\varphi_m = 8.00(\theta - 0.047)^{1.5} \tag{2.6}$$

$$\varphi_w = 3.97(\theta - 0.0495)^{1.5} \tag{2.7}$$

where φ represents the dimensionless bed load transport rate (Einstein parameter), θ is the dimensionless bed shear stress (Shields parameter) with a critical value for the initiation of motion of grains at the bed, respectively 0.047 (MPM) and 0.0495 (WP). For the MPM bed load transport predictor, the scale factor (m) was determined to be 8, and the shape factor (n) was found to be 1.5 through curve fitting analysis. Later research conducted by Wong and Parker (2006) involved a re-analysis of the bed load transport formulation proposed by MPM. They identified and corrected an unnecessary bed roughness correction for plane-bed conditions that MPM had applied. The revised analysis resulted in an adjusted scale factor of 3.97, while the shape factor remained constant at 1.5. The original MPM transport formulation is based on the total dimensionless bed shear stress, which was corrected for ripple roughness using a ripple factor. Here, a more straightforward approach for calculating the dimensionless grain bed shear stress (θ') is utilized, following Van Rijn (1984). The dimensionless grain bed shear stress can be calculated from the grain bed shear stress (τ'), defined as:

$$\tau' = \rho_w g \frac{\bar{u}^2}{C'^2} \tag{2.8}$$

with the water density ρ_w, the gravitational acceleration g (9.81 m s^{-2}), the depth-averaged velocity $\bar{u}$, and the Chézy grain roughness C' given by the White-Colebrook formula:

$$C' = 18 \log \frac{12R}{k_s} \tag{2.9}$$

in which R is the hydraulic radius, and k_s is the Nikuradse current-related grain roughness, again assumed to be equal to the grain diameter at the 90^{th} percentile (d_{90}). The dimensionless grain bed shear stress is given as:

$$\theta' = \frac{\tau'}{(\rho_s - \rho_w) g d_{50}} \tag{2.10}$$

The bed load transport rate is expressed in non-dimensional form as:

$$\varphi = \frac{q_{b,c}}{\rho_s \sqrt{\frac{\rho_s - \rho_w}{\rho_w} g d_{50}^3}} \tag{2.11}$$

where $q_{b,c}$ is the bed load transport rate in kg s^{-1} m^{-1}, ρ_s is the sediment density (2640 kg m^{-3}), ρ_w is the water density, g is the gravitational acceleration, and d_{50} is the mean grain diameter.

Since bed load transport was measured near the threshold of motion, an empirical predictor, such as MPM, is affected by the criterion for the threshold of motion. The presence of turbulence-induced

flow fluctuations enables transport in conditions below the threshold of motion. To account for this, a simple stochastic approach, as outlined by Kleinhans and van Rijn (2002); Kleinhans and Grasmeijer (2006), is used in the WP predictor. Bed load transport rates are calculated for a range of grain bed shear stresses (τ'). Each τ' is described by a Gaussian distribution, where the mean is equal to τ', and the standard deviation $\sigma_{\tau'}$ is given as $\sigma_{\tau'} = \gamma\tau'$. The relative standard deviation γ of τ' must be chosen appropriately, in which De Ruiter (1980) and Bridge and Bennett (1992) give $\gamma = 0.4$. The transport is calculated for a range of τ'_i below and above the average τ'. The calculated transports φ_i are multiplied with the probabilities p_i of occurrence of all the τ'_i in the shear stress distribution. For a discrete normal distribution with class width Δ:

$$p_i = \Delta \frac{\tau'}{\sqrt{2\pi\sigma_\tau}} \exp\left[-\frac{1}{2}\left(\frac{\tau'_i - \tau_{cr}}{\sigma_\tau}\right)\right] \tag{2.12}$$

The distribution is discretized for $-6\sigma_\tau \leq \tau' \leq 6\sigma_\tau$. The sum of the products represents the cumulative bed load transport due to turbulent fluctuations:

$$\varphi = \sum p_i \varphi_i \tag{2.13}$$

for non-zero transport φ_i, which implies calculation only for $|\tau'_i| > |\tau_{cr}|$.

Using this method, bed load transport can be quantified for a bed composition consisting of sandy sediment and shells, allowing for a comparison with both existing bed load transport predictors and an additional stochastic approach.

3 Results

Here, we present the results of the study. The following section illustrates the results of the threshold of motion analysis. Section 3.2 describes the results of the bed load transport analysis. The chapter concludes with a description of the results of the bed load characteristics (Section 3.3).

3.1. Threshold of motion of sand grains

In general, the performed analysis obtained agreeable results. The GoPro video recordings allowed for a precise determination of the defined motion stages. However, the threshold of motion could not be determined for a shell content of 50% due to excessive shell coverage.

3.1.1. Flow characteristics

Figure 3.1 presents the relationship between the depth-averaged velocity and shell content for each distinct motion stage. The results showed only a slight difference in depth-averaged velocity between a shell content of 10% and the experimental control with 0% shells. Mainly at a shell content of 20%, a clear contrast between sediment-shell mixtures can be observed. Specifically, the bed composition containing only *E. leei* shells showed a decrease in depth-averaged velocity, while the mixture showed an increase in depth-averaged velocity. As for *S. subtruncata* shells, no distinct difference was observed during the first two motion stages, but an increase was observed during motion stage 3.

The depth-averaged flow velocity alone is insufficient to provide a complete understanding of sediment-flow interactions. Therefore, Figure 3.2 presents the turbulence intensity and relative turbulence. For the bed composition containing only *E. leei* shells, no significant difference was observed in depth-

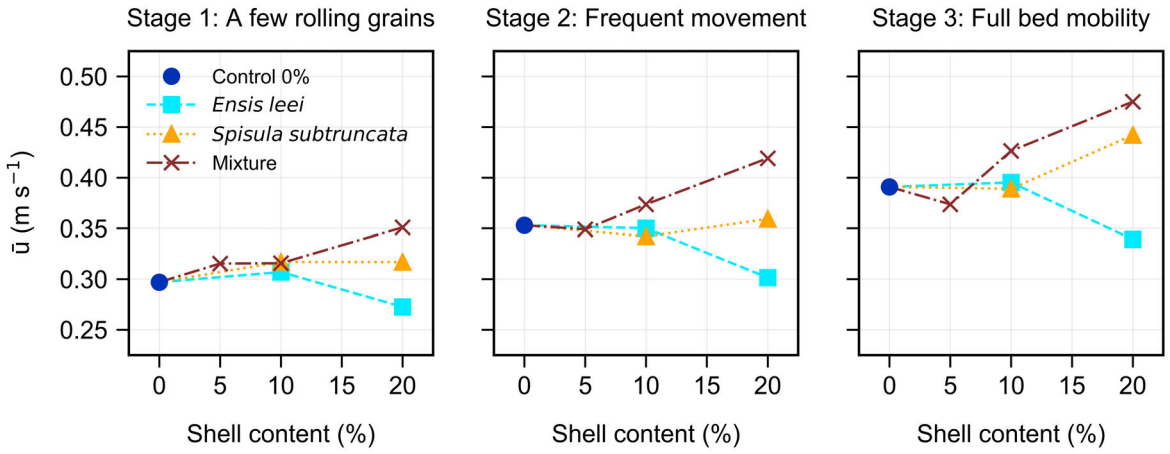

Figure 3.1: The depth-averaged velocity versus shell content separately for each motion stage. The lines and markers indicate the different sediment-shell mixtures, whereas the control indicates the experimental group with 0% shells.

averaged velocity between the control (0% shells) and a shell content of 10%. However, a noticeable decrease in depth-averaged velocity was observed for each motion stage when the shell content increased to 20%. This decrease in depth-averaged velocity corresponds to an increase in turbulence intensity and relative turbulence (Figure 3.2d/g). The bed composition consisting of only the *S. subtruncata* shells showed no significant difference in depth-averaged velocity when comparing the control (0% shells) with a shell content of 10%. The depth-averaged velocity increased for a shell content of 20%. However, this was only clearly observed for motion stage 3 (Figure 3.2b). The turbulence intensity and relative turbulence slightly increased at a shell content of 10%. At a shell content of 20%, the turbulence intensity and relative turbulence decreased, except at motion stage 1, where they increased further (Figure 3.2e/h). When both *E. leei* and *S. subtruncata* shells were combined (i.e., mixture), an initial decrease in depth-averaged velocity was observed. This was followed by an increase in depth-averaged velocity from a shell content of 10%, which continued to increase at a shell content of 20% (Figure 3.2c). Again, turbulence intensity and relative turbulence showed an initial increase at shell contents of 5% and 10%, after which they decreased (Figure 3.2f/i).

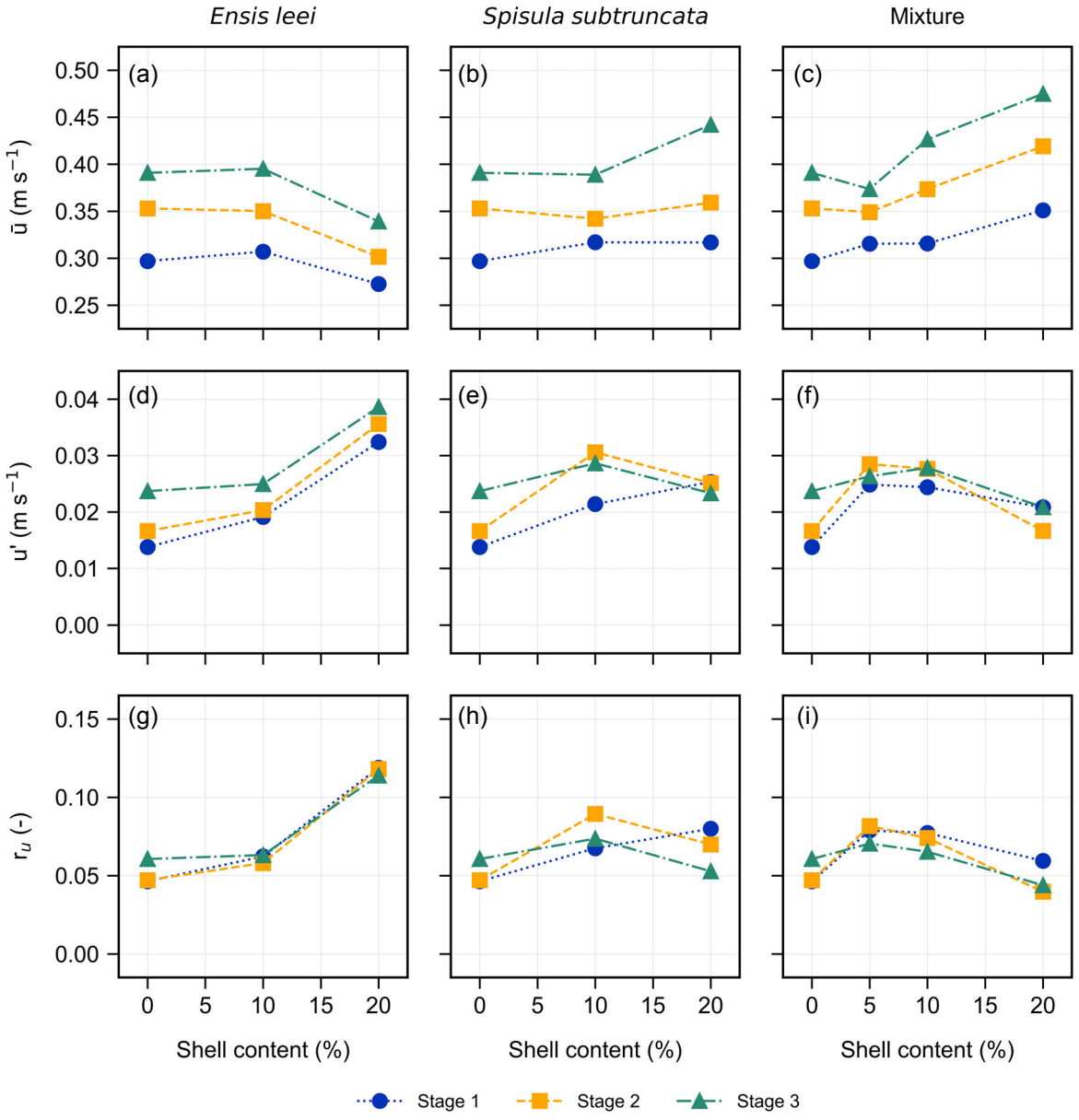

Figure 3.2: The depth-averaged velocity (a-c), turbulence intensity (d-f), and relative turbulence (g-i) versus shell content separately for each sediment-shell mixture. The lines and markers indicate the different motion stages: (i) stage 1: A few rolling grains, (ii) stage 2: Frequent movement, and (iii) stage 3: Full bed mobility.

In Figure 3.3, the turbulence intensity and depth-averaged velocities are presented together, and the lines connect the three stages of motion from a single experiment. A dashed line is included in the figure, representing the relationship between turbulence intensity and depth-averaged velocity under the assumptions of a logarithmic flow profile and a constant relationship between depth-averaged velocity and turbulence intensity at the depth-averaged velocity (Section 2.3.1). The results indicate that both the turbulence intensity and the depth-averaged velocities show a distinct difference from the control (0% shells). Some sediment-shell mixtures demonstrated an increase in turbulence intensity, while others showed an increase in depth-averaged velocity or even both. Especially the experiment with a shell content of 20% and a bed compositing consisting of *E. leei* shells showed a considerable increase in turbulence intensity while the depth-averaged velocity remained more or less similar to the control (0% shells). The experimental control with 0% shells does not follow the theoretical line. Turbulence intensity is lower for a given depth-averaged velocity.

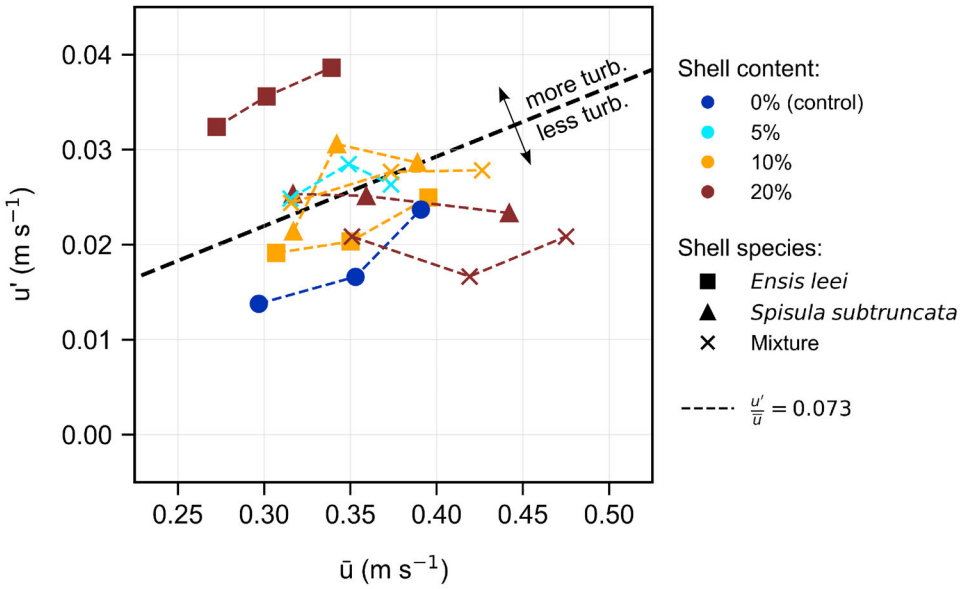

Figure 3.3: Turbulence intensity versus depth-averaged velocity. The lines connect the three stages of motion of a single experiment. The colors indicate the shell content, whereas the markers indicate the shell species. The dashed line indicates the relationship between the depth-averaged velocity and turbulence intensity.

3.1.2. Bed shear stress

Figure 3.4 presents the dimensionless bed shear stress (Shields parameter) and the bed shear stress. Both quantities show a similar trend since the Shields parameter is derived from the bed shear stress (as per Equation D.1). The bed shear stress increased for sediment-shell mixtures with a shell content of 10%. However, above this point, the bed shear stress decreased again for sediment-shell bed compositions consisting of *S. subtruncata* shells or a mixture of both shell species. In contrast, bed compositions consisting of *E.* shells showed the opposite behavior, with the shear stress continuing to increase. Furthermore, bed shear stresses remain below the threshold of suspension of sediment (Section 2.2.2).

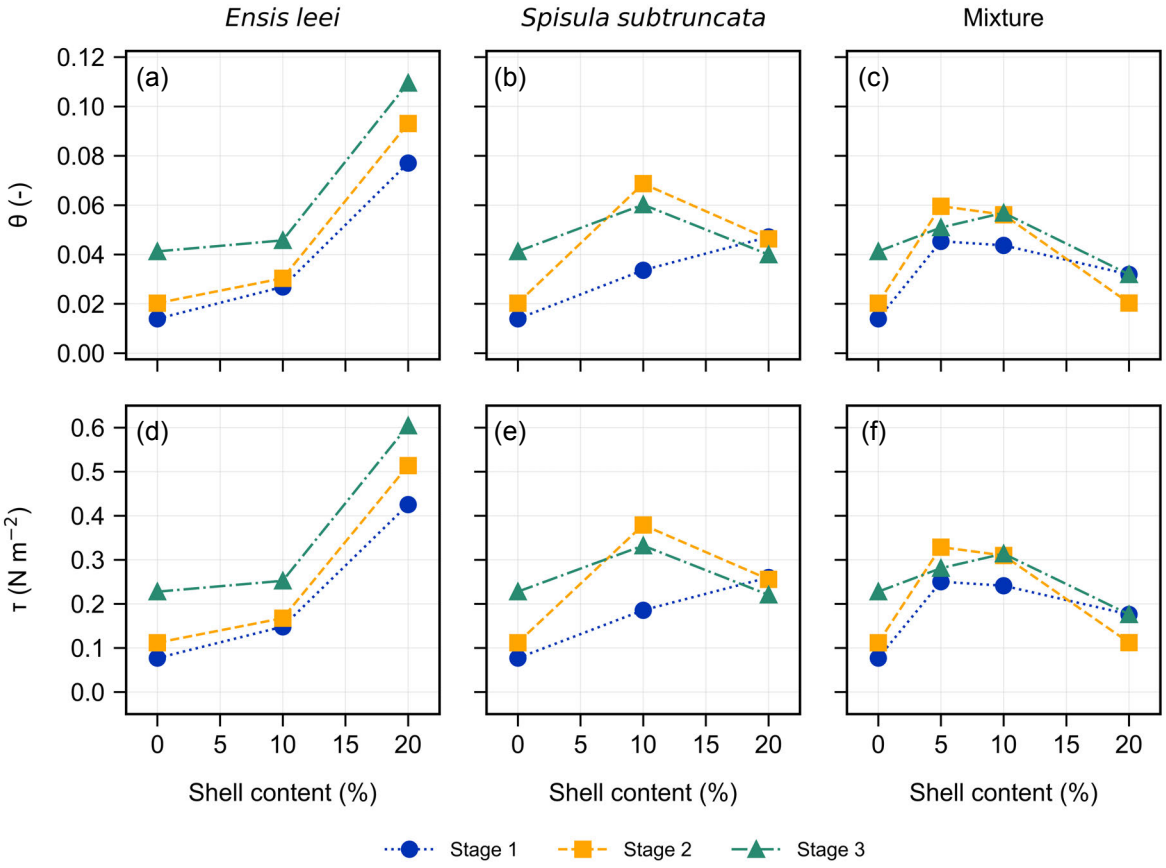

Figure 3.4: Dimensionless bed shear stress (a-c), and bed shear stress (d-f) versus shell content for each sediment-shell mixture separately. The lines and markers indicate the different motion stages: (i) stage 1: A few rolling grains, (ii) stage 2: Frequent movement, and (iii) stage 3: Full bed mobility.

3.1.3. Influence of the water-worked bed surface

Figures 3.5a-c present the relationship between the depth-averaged velocity and shell content for each sediment-shell mixture. The focus is on comparing the initial flat surface with the water-worked surface for motion stage 1. The water-worked bed showed an increasing depth-averaged velocity with increasing shell content for each sediment-shell mixture. Particularly at higher shell contents (20%), a significant difference is observed between the depth-averaged velocity of the initial flat surface and the water-worked surface. Furthermore, the turbulence intensity and relative turbulence showed a noticeable increase for the control when comparing the initial flat surface with the water-worked surface. However, for most other bed configurations, the turbulence intensity and relative turbulence showed only minor differences (Figure 3.5d-i).

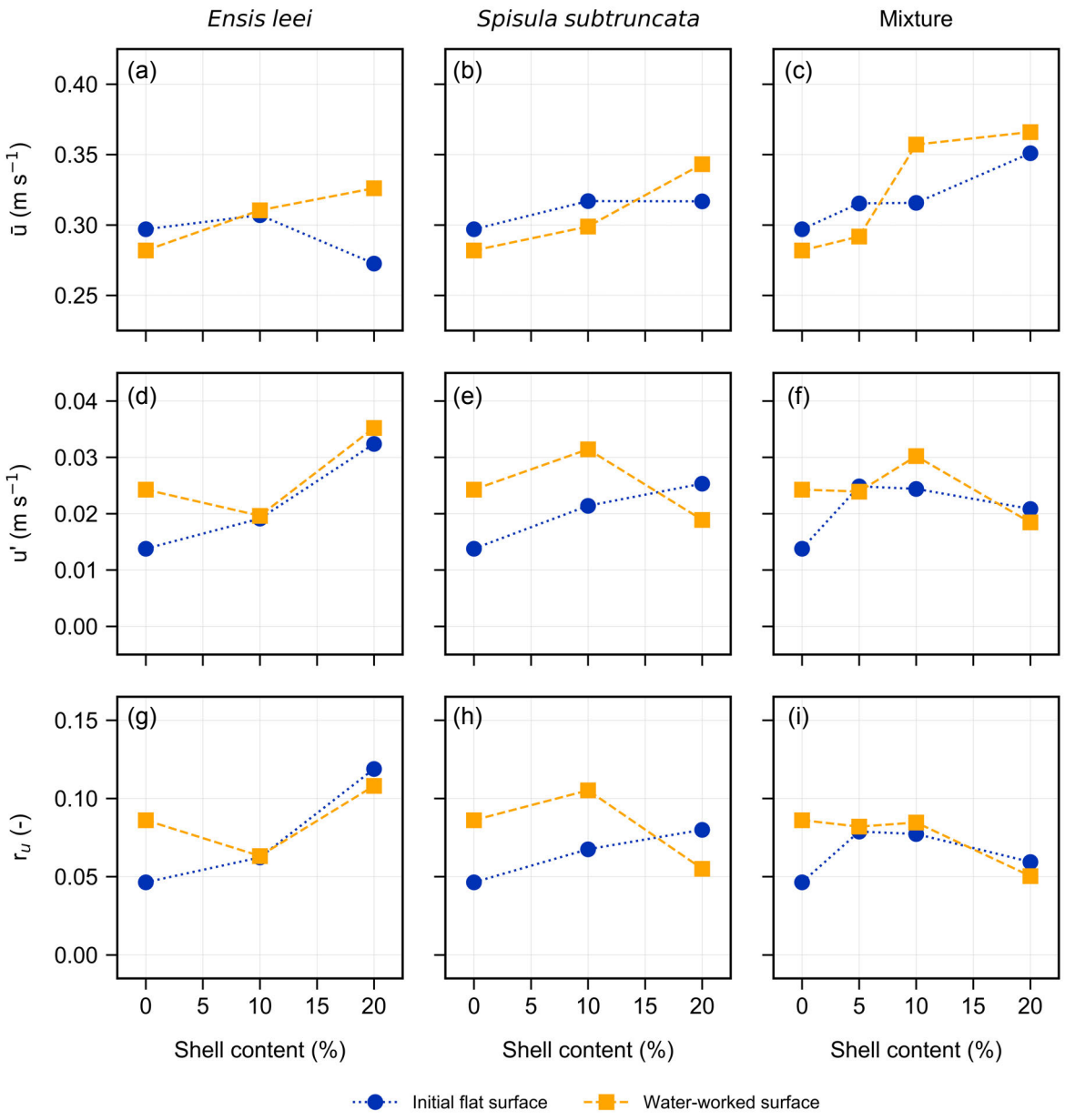

Figure 3.5: The depth-averaged velocity (a-c), turbulence intensity (d-f), and relative turbulence (g-i) versus shell content separately for each sediment-shell mixture with a focus on the influence of the water-worked bed surface in stage 1: A few rolling grains.

3.2. Quantification of bed load transport

Measured bed load transport rates are represented in Figure 3.6. The figure consists of individual plots that represent the bed load transport rates for different shell contents, as well as a division based on total mass, the fraction smaller than 1 mm, and the fraction larger than 1 mm. Overall, as the depth-averaged velocity increased, there was a corresponding increase in bed load transport rates. When comparing a shell content of 10% to the situation without any shells, no clear trend was observed between bed load transport rates. However, bed load transport rates showed a (slight) decrease when comparing a shell content of 20% to a shell content of 10% or no shells (0%). No clear trend is observed between the different sampling intervals.

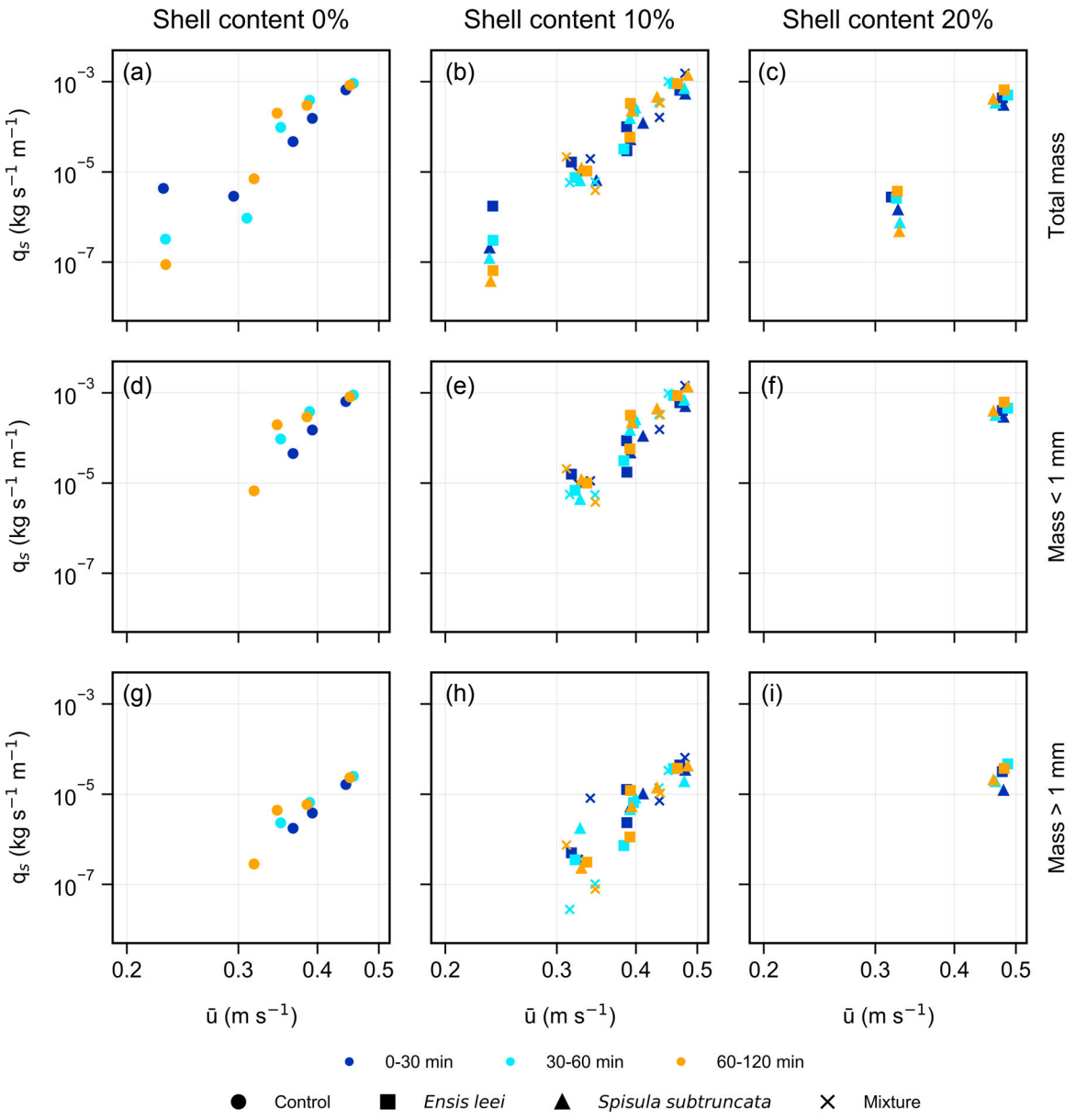

Figure 3.6: Bed load transport rates total (a-c), smaller than 1 mm (d-f), and larger than 1 mm (g-i) versus depth-averaged velocity separately for each shell content. The colors indicate the sampling interval, and markers indicate the various sediment-shell mixtures.

3.2.1. Predicted bed load transport rates

In Figure 3.7, the measured bed load transport rates are represented versus dimensionless grain bed shear stress. At Shields parameters above the critical Shields value (given by MPM and WP), the data are generally over-predicted by most predictors. The WP predictor showed the best fit. Above the critical Shields value, it over-predicts the bed load transport by a factor of 3-4. Below the critical Shields value, the MPM and WP predictors showed no transport. This corresponds well to data points near the critical Shields value. However, a scatter is observed below this threshold, and bed load transport rates correspond to lower dimensionless grain bed shears stresses, i.e., transport stages 1 or 2 (Figure 3.4). A stochastic approach to WP (Kleinhans and van Rijn, 2002) showed an improved fit. However, the stochastic approach overestimated bed load transport near and above the critical Shields value.

In general, bed load transport rates reduced (slightly) with a shell content of 10%. With increasing shell content (20%), bed load transport rates are further reduced. Appendix F shows this behaviour in separate figures for *E. leei* and *S. subtruncata* shells (Figure F.8 and Figure F.9). At a shell content of 20%, measurements showed that bed load transport rates for *E. leei* shells decreased to a lower extent than the *S. subtruncata* shells. The trend is less visible for the combination of shell species (Mixture) as no experiments have been performed for a shell content of 20% (Figure F.10).

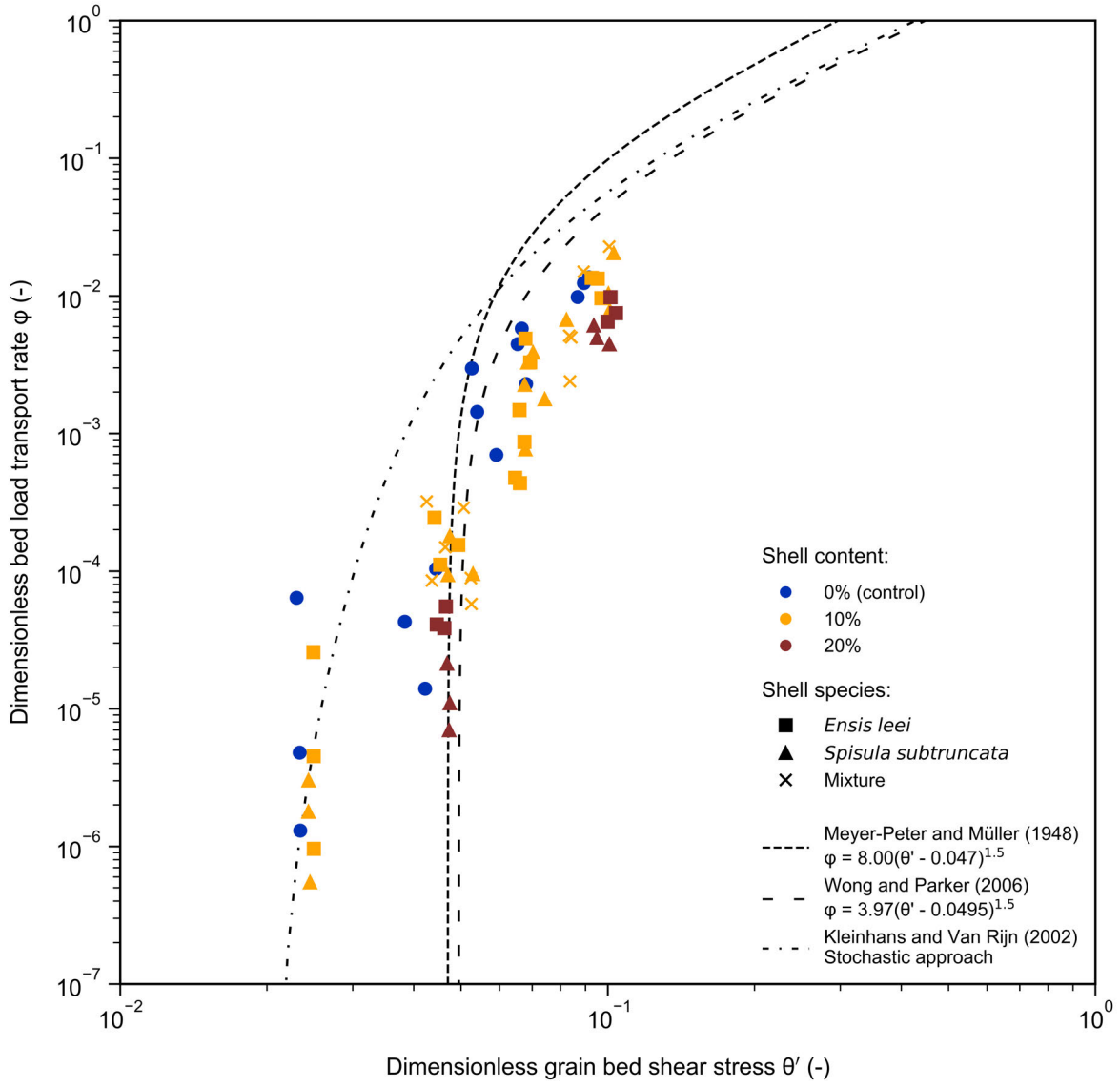

Figure 3.7: Dimensionless bed load transport rate versus dimensionless grain bed shear stress. Comparison to MPM and WP transport predictors. The colors indicate shell content, and markers indicate the shell species.

3.3. Characterisation of bed load transport

The bed load collected during the constant flow experiment was sieved using a 1mm sieve to separate the smaller sand grains from the larger shell fragments and shell valves. The particle size distribution of the smaller fraction was then determined using laser diffraction. The sediment grain size was plotted against the flow velocity for each percentile and shell content separately (Figure 3.8). The different colors represent different time intervals, as explained in Section 2.2.2, while different markers indicate the sediment-shell mixture.

To provide further context, a vertical line was introduced in the plot to highlight the sediment size of the initial North Sea sandy sediment (Table A.1 in Appendix A). The results showed that the percentiles of the transported bed load are generally smaller than the initial sandy sediment size. No clear pattern emerged over time, and no clear distinction was observed between sediment-shell bed configurations.

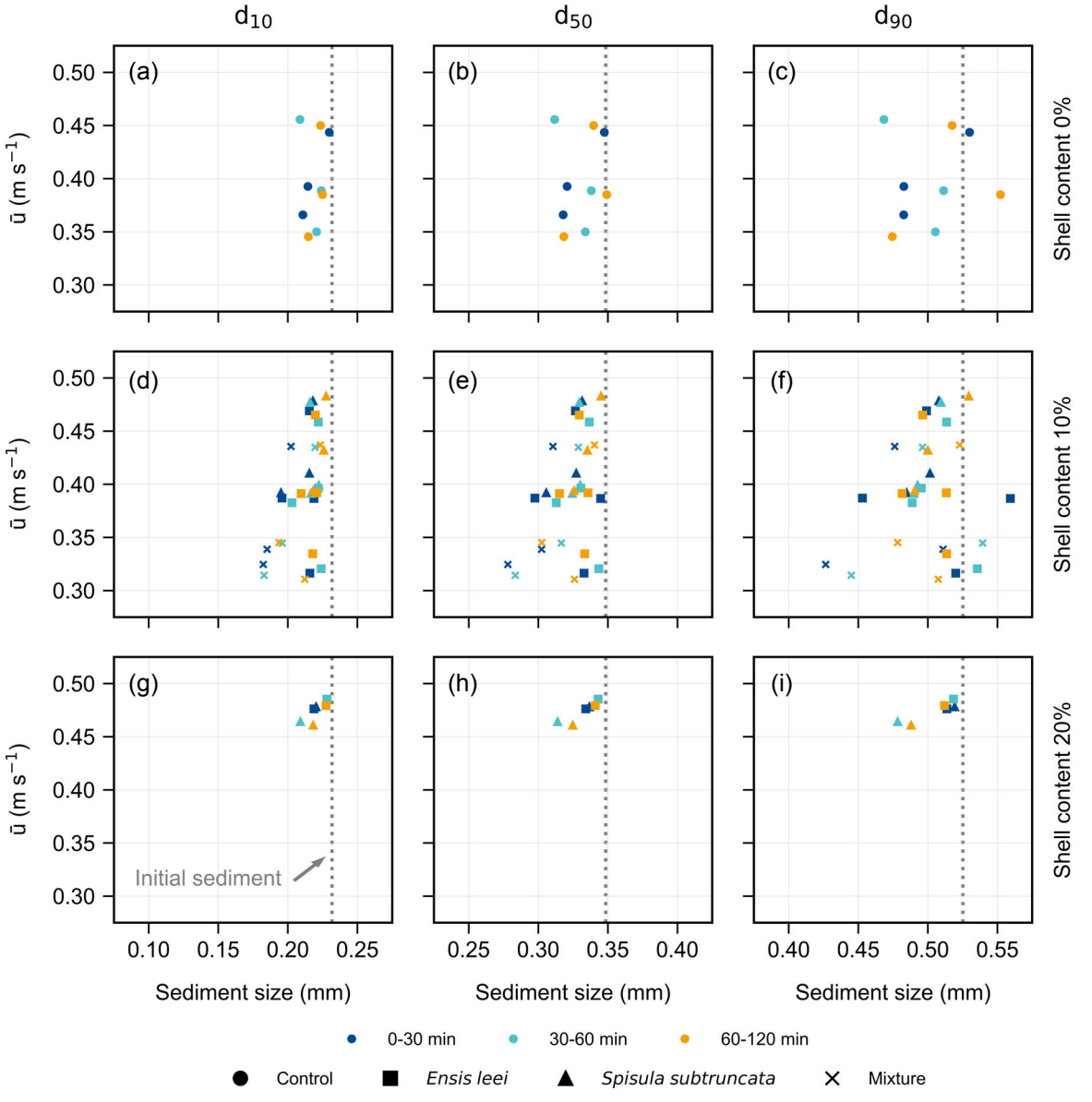

Figure 3.8: Depth-averaged velocity versus sediment size for three percentiles and each shell content. The colors indicate the different measurement intervals, and a distinction is made between sediment-shell mixtures using different markers. The vertical lines indicate the initial sediment size of the initial North Sea sandy sediment (Table A.1 in Appendix A).

4

Discussion

The discussion starts with the findings of the slowly accelerating flow experiment (Section 4.1). Next, Section 4.2 discusses the results of the constant flow experiment, focusing on bed load transport. The chapter concludes with a discussion on existing bed load transport predictors (Section 4.3).

4.1. Shell vs threshold of motion

Similar to what was described by Cheng et al. (2021), an opposing behavior is observed in the depth-averaged velocities and turbulence intensities. This behavior suggests that shells have the potential to modify sediment-flow interactions in two ways: (i) by stabilizing the sediment, and (ii) by increasing the bed roughness.

When the shell content is 10%, and the bed is composed of a single species of shells, the findings suggest that each shell valve functions as an isolated roughness element, i.e., isolated roughness spacing (Figure 1.5a). The hydraulic effects caused by the shells are dissipated before the flow encounters the next shell, resulting in a limited overall impact on the flow field. The depth-averaged velocities show no significant differences compared to the experimental control with 0% shells. However, the turbulence intensities increase, and subsequently, the bed shear stress required for the same motion of sand particles increases (Figure 3.4).

When the shell content increases (20%), the depth-averaged velocities and turbulence intensities show a distinct difference compared to the lower shell content (10%). The former suggests that isolated roughness spacing no longer holds, indicating the formation of shell clusters. The results reveal a distinct difference between both shell species. In the case of a bed consisting of *S. subtruncata* shells, the depth-averaged velocity increases while the turbulence intensities decrease. This reduces relative turbulence and, consequently, a lower friction coefficient (as per Equation 1.1). The streamlined shape and small frontal area of the shells may cause the flow to be deflected over the shells, minimizing disturbances in the boundary layer. As a result, turbulence intensities are reduced, leading to sediment stabilization. The bed shear stress required for the same motion of sand particles is lower than the lower shell content (10%), although it is still higher than without any shells. Previous research has shown a similar reduction in turbulence intensity as roughness spacing decreases. Tan and Curran (2012) demonstrated that when three clusters were closely located on the bed surface, the recirculation cells produced by each cluster would interfere with one another, resulting in a reduction in the overall turbulent flow field intensity, similar to a skimming flow (Figure 1.5c).

In contrast, when considering a bed consisting of *E. leei* shells, the depth-averaged velocity decreases while the turbulence intensities increase. This leads to an increase in relative turbulence and consequently a higher friction coefficient (as per Equation 1.1), i.e., an increase in bed roughness. Visual observation of the GoPro video recordings reveals that *E. leei* shells were positioned side-ways or protruded significantly above the bed surface, resulting in an enlarged frontal area, and hence greater obstruction of the flow. Additionally, due to their elongated shape, flow lines became curved and flow separation occurs, increasing overall turbulence intensities. Curran and Tan (2014) show a similar behavior of clusters on a gravel bed, where the flow separates over the cluster crest, creating an increase in turbulence intensities and a high-turbulence intensity region when the flow re-attaches to the bed.

As the bed consisted of a combination of both shell species, the results suggest that shells may have disrupted the flow at a low shell content (5%). Cheng et al. (2021) found a similar initial increase in turbulence intensities at low shell contents. For an increasing shell content (10% and 20%), the results indicate a similar trend as observed for the *S. subtruncata* shells. Initially at 10%, the depth-averaged velocity and turbulence intensities increase, causing an increase in the bed shear stress required for the same motion of sand particles. At 20% shell content, the depth-averaged velocity increases while the turbulence intensities decrease. The required bed shear stress for the same motion of sand particles is therefore reduced compared to 10%, but still higher than the situation without any shells.

It is proposed that the presence of shells initially disrupts the flow, causing an increase in turbulence intensities. In theory, this indicates that the bed shear stress required for the motion of sand particles is reached at a lower depth-averaged velocity ((Figure 3.2a). However, the bed shear stress required for the same motion of sand particles increases (slightly), indicating the existence of the second sediment-shell effect: sediment stabilization. The smaller sediment grains are hidden from the flow by larger, more exposed shell valves and shell fragments. Consequently, higher bed shear stress is needed to mobilize the sand grains due to this hiding-exposure effect (sediment stabilization). A similar observation was made by McCarron et al. (2019) regarding bimodal sediment mixtures, where an increase in the proportion of coarse to fine material led to an increase in critical bed shear stress due to the hiding-exposure effect. The effect of shells on the threshold of motion of sand grains is determined by the relative magnitude of both the increase in turbulence intensities caused by increased bed roughness and the hiding-exposure effect resulting from sediment stabilization.

Our research findings indicate that the presence of shells affects the required bed shear stress for the motion of sand particles. At a very low shell content (5%), the depth-averaged velocity required for the same amount of particle movement decreases slightly, and higher turbulence intensities are observed compared to the situation without shells. This indicates that the increase in roughness is greater than the sediment stabilization as movement is observed at a lower depth-averaged velocity. At a shell content of 10%, a similar amount of particle movement is observed at a comparable depth-averaged velocity as with the situation without shells. However, higher turbulence intensities are observed, indicating that higher bed shear stress is required to move the grains. Since particle movement is still observed at a comparable depth-averaged velocity, this indicates that both the effect of increased bed roughness and the effect of sediment stabilization are of similar magnitude.

In contrast, at a higher shell content (20%), turbulence intensities decrease, and a higher depth-averaged velocity is needed for the same amount of movement compared to the situation without shells. The effect of sediment stabilization is no longer balanced by an increase in bed roughness. This holds true unless the shell species has the potential to further increase turbulence intensities and overcome the sediment stabilization process. In this case, the shape, size, and ability of the shells to generate turbulence become significant factors. Both shell species researched in this study show opposing behavior. Figure 4.1 provides a schematic representation of this process.

At a very high shell content of 50%, it was not possible to determine the threshold of motion. The shell cover was extensive, patches of shells formed, and limited sediment movement was observed. This suggests that the flow is shifted to the top of the shells, known as skimming flow conditions (Figure 1.5c), and the lack of sediment movement around the patches further limits the velocities near the bed. Mayaud et al. (2016) observed similar behavior for densely packed vegetation patches, where velocities decrease in the near-surface region behind a patch, and the potential for sediment transport is reduced.

If flow velocity exceeds well above the threshold of motion of grains, it is possible for shells to also be displaced. Shells seek a more stable position and a favorable orientation, limiting the increase in turbulence intensities. Additionally, as sediment is eroded, more shells appear on the surface, leading to increased armor formation. However, the water-worked bed results (Figure 3.5) do not sufficiently support either hypothesis, as neither process is clearly represented in the data. It is possible that the flow velocities did not reach a level high enough to displace the shells and that velocities above the threshold of motion for sand grains did not persist sufficiently to erode sediment and increase shell cover for stimulating armor formation.

Moreover, it is important to note that the results presented in this study are based on a single experimental run. Repetition of the experiment is necessary to provide better certainty regarding the observed outcomes.

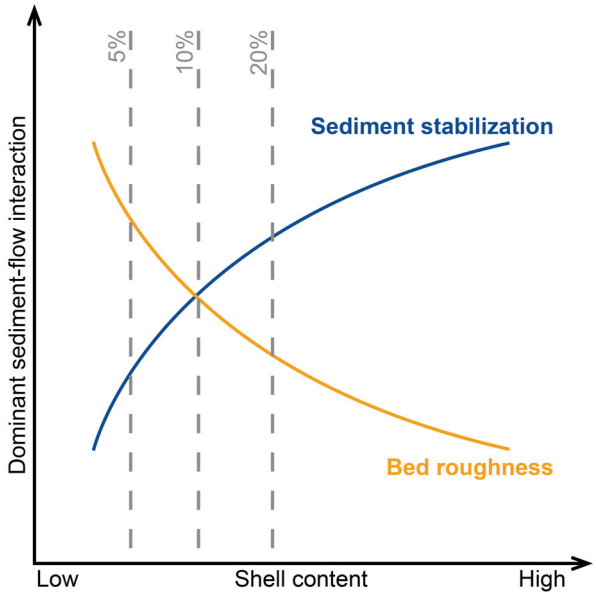

Figure 4.1: Schematic of the dominant sediment-flow interaction with changing shell content. An important note: The purpose of the lines is to draw a comparison between the two processes, but the shape lacks a theoretical basis.

4.2. Reduced bed load transport rates

Velocity measurements combined with measured bed load transport rates show declining bed load transport rates as shell content increases (Figure 3.6). At a shell content of 10%, bed load transport rates only decrease marginally compared to a situation without shells. However, at a higher shell content of 20%, the decrease becomes apparent. Several studies have indicated that turbulence plays a significant role in the movement and displacement of particles (e.g., Celik et al., 2010; Shih and Diplas, 2018; Dey et al., 2019). The results show that shells produce additional turbulence that impacts sediment transport (Figure 3.3). Similarly, other roughness elements such as vegetation and bedforms have been shown to generate extra turbulence and, consequently, affect sediment transport (Yang and Nepf, 2018). With increasing shell content, the roughness spacing changes. Shell clusters form and reduce the overall turbulent flow field intensity, limiting sediment transport, similar to was observed by Tan and Curran (2012). Furthermore, the results show that the presence of shells increases the required bed shear stress for the same motion of sand particles (Figure 3.4), thereby limiting bed load transport. A similar finding was made by Curran and Tan (2014), who show a decrease in mobility, indicating a higher degree of bed surface stability, as sand content decreases on an armored gravel bed surface.

Although not explicitly studied in this research, shells are known to alter the bed topography, thereby impacting sediment transport. During the experiments, the shells were mainly completely immobile over the entire duration of the experimental runs. The presence of shells reduces the amount of sediment available for transport. Moreover, shells create a wake structure behind them, reducing velocities on the trailing edge of the shell and consequently reducing sediment mobility. With an increase in shell content and a decrease in roughness spacing, the areas of limited mobility become more prominent (Nowell and Jumars, 1984).

Over time, more shells appear on the surface as sediment erodes, leading to increased armor formation. Additionally, preferential transport of finer sand fractions can induce bed armoring (Huisman et al., 2016). However, the results of this study did not explicitly show an armoring process. While sediment size did slightly coarsen over time (Figure 3.8), potentially hinting on preferential transport as a function of grain size, as reported by Pearson et al. (2021), no clear trend was observed regarding declining bed load transport rates. It is possible that the flow velocity did not persist sufficiently to clearly show the effect of bed armoring, which takes some time to develop (Kleinhans and van Rijn, 2002).

4.3. Test of existing bed load transport formulations

The deviation between measured bed load transport rates and the existing transport predictors (Figure 3.7) could be caused by several reasons. One key factor is that the current bed load transport formulations do not consider the presence of shell content. Adjustments accounting for shell cover, which reduces the effective area, and the alterations in flow patterns around shells have not been incorporated. Incorporating these effects will result in a reduction factor, similar to reducing the scale factor in the existing bed load transport formulations. Reducing the scale factor by a factor of 2 shows the impact of such a 'shell cover' reduction factor (Figure F.6), resulting in a vertical line shift. Alternatively, an overestimation of grain roughness could lead to deviation, as a smaller grain roughness also results in a vertical shift of the line (Figure F.5). Most likely, the calculated grain bed shear stresses might be overestimated due to the absence of corrections for sidewall effects (e.g., Vanoni and Brooks, 1957). Additionally, the boundary layer may not have been fully developed, leading to a rightward shift in the data (Figure 3.3).

The stochastic approach shows improved results for the bed load transport near the threshold of motion (Figure 3.7), more accurately representing the natural process of turbulence-induced flow fluctuations. The continuation of bed load transport below the threshold of motion reveals a gradual incipient region instead of a distinct threshold, which aligns with well-established knowledge (e.g., Breusers and Schukking, 1969). Above the threshold of motion, the stochastic predictor gradually approaches the non-stochastic WP predictor, to which the stochastic module was applied. If a relative shear stress deviation of 0.2 is used instead of 0.4, the stochastic transport predictor exhibits a steeper behavior below the threshold of motion (Figure F.7). With increasing shell content, turbulence intensities decrease (Section 4.1). Thus, it is argued that an improved approximation of the relative shear stress deviation is needed for different shell contents to obtain a better fit.

5

Conclusions and Recommendations

This report is completed with a series of concluding remarks and recommendations. The research questions, as defined in Section 1.3, are answered in Section 5.1. Section 5.2 addresses the limitations encountered. And lastly, section 5.3 focuses on the recommendations for future (experimental) studies looking into the complex interaction between bivalve shells and their physical environment.

5.1. Conclusions

This research aimed to provide insights into the complex interaction between bivalve shells and their physical environment. To achieve the research goal, an experimental flume study was carried out to investigate the effects of bivalve shells on sediment transport under a unidirectional flow. In this section, the study's key findings are summarised by answering the sub-questions, after which a conclusion is drawn by addressing the main research question.

1. **What are the important parameters of current-driven sand transport, and how can they be quantified in an experimental flume study?**

   In an experimental flume study, sediment transport can be quantified by determining the shear stress and the bed load transport rates. The shear stress is influenced by the flow velocity and bed roughness, both of which can be obtained using velocity measurements. The flow velocity can be measured using an Acoustic Doppler Velocimeter to measure depth-averaged velocities or an Acoustic Doppler Velocimeter Profiler to measure the near-bed flow velocities. Bed roughness, caused by irregularities and protrusions on the sediment bed, can be assessed through turbulence intensity measurements.

   The bed load transport rate, which indicates the volume or mass of sediment transported over time, can be measured using a sediment trap. Additionally, it is essential to consider the sediment grain size and water salinity as they play crucial roles. Sediment grain size can be determined through techniques such as laser diffraction or sieving, while water salinity can be measured using a salinity meter.

   Collectively, quantifying these parameters contributes to understanding current-driven sand transport in experimental flume studies.

2. **What is the influence of bivalve shells on the threshold of motion of sand particles?**

   The presence of bivalve shells can influence the sediment-flow interactions in two ways: (i) by stabilizing the sediment, and (ii) by increasing the bed roughness. The relative magnitude of these processes varies depending on shell content and shell species. Initially, at a very low shell content (5%), shells disrupt the flow in the boundary, leading to an increase in bed roughness. As the shell content increases, both processes reach a similar magnitude at around 10%. When the shell content is even higher (20%), the roughness spacing changes, and sediment stabilization

becomes more prevalent than the increase in bed roughness. However, this is true only if the shell species does not have the potential to enhance turbulence intensity further and overcome the stabilization effect. With its elongated shape, the *Ensis leei* shell appears to have this potential at a shell content of 20%. In contrast, the *Spisula subtruncata* shell and the combination of both shell species do not exhibit this potential at 20% shell content.

3. **What is the influence of bivalve shells on bed load transport (rates)?**

   Bed load transport rates decrease with increasing shell content. Initially, at a shell content of 10%, the rates only decrease marginally compared to a situation without shells, and no clear difference between shell species is observed. When shell content increases to 20%, bed load transport rates further decrease. The *E. leei* shell exhibits higher transport rates than the *S. subtruncata*, which can be related to the ability of the *E. leei* shell to generate turbulence.

   Existing bed load transport formulations deviate from measured bed load transport rates. Most probably, the reason is two-fold: (i) existing formulations do not take shell cover and alterations in flow patterns around shells into account, and (ii) calculated grain bed shear stresses have been overestimated. Based on the analyses of the data and predictors, it can be concluded that a predictor based only on dimensionless shear stress is not feasible. This conclusion is drawn because several data points consistently fall below the values predicted by most predictors. Thus, it is essential to consider the impact of shell cover, increased bed roughness, and sediment stabilization properties resulting from the presence of shells. These factors can exert a substantial influence on bed load transport rates. Additionally, it can be concluded that using a stochastic approach improves existing bed load transport predictors.

   The characteristics of bed load transport do not exhibit a distinct impact on bed armoring, likely due to the extended duration of the required processes for this to occur.

The main research question is repeated here:

> How do bivalve shells of different shapes and sizes influence current-driven sand transport?

In conclusion, bivalve shells influence current-driven sand transport in two main ways: by stabilizing the sediment and by increasing the bed roughness. The relative importance of these processes varies depending on shell content, shell species, and the potential of the shell to enhance turbulence intensities. With increasing shell content, bed load transport rates decrease. The *E. leei* shell appears to have a higher transport rate than the *S. subtruncata*, due to the ability of the *E. leei* shell to generate turbulence. Thus, when predicting sediment transport or the behavior of sand nourishments over time, the mere presence of shells alone is insufficient, and consideration of shell shape and size is crucial. Additionally, the enhancement of current bed load transport predictors using stochastic modeling has been demonstrated to give more accurate predictions.

5.2. Limitations

The study was limited by two main constraints that restricted the scope: (i) simplification of processes that experimental flume research necessarily entails, and (ii) time-based limitation on varying bed configurations, varying forcing conditions, and the selection of data to analyze.

The key limitations regarding the scope therefore included:

- Selection of shell species
- Sediment-shell bed configurations
- Hydrodynamic forcing conditions
- Experimental flume setup
- Selection of data to analyze

5.3. Recommendations

This section summarizes the recommendations for future (experimental) studies and practical applications based on the findings of this report.

1. **Extend the experimental dataset**

   This work would greatly benefit from further studies to extend the experimental dataset. For example, including different grain sizes, a more comprehensive range of shell species, or more sediment-shell bed compositions would be beneficial. A valuable start would be extending the existing database by incorporating a sediment-shell bed composition of 30%, aiming to assess the persistent impact of *E. leei* on turbulence intensity. Additionally, it is recommended to include additional data points for bed load transport rates at higher shell contents, specifically 20% and beyond. This expanded database has the potential to reveal a more distinctive decline in bed load transport rates with increasing shell content.

   Additionally, simulating tidal conditions by incorporating a change in velocity direction would allow for a more realistic representation of natural environments and help capture the complexities associated with tidal effects.

2. **Use more precise measurement techniques**

   Visual observations of the threshold of motion can be subjective. It is recommended to use quantitative methods to assess the threshold of motion more accurately. For example, (Uphues et al., 2022) performed a tracer study where grains were marked in such a way that their transport characteristics were not changed, and the displacement of grains was determined with higher accuracy. Alternatively, Celik et al. (2010) showed the benefit of using a particle tracking system that offers high temporal and spatial resolution in detecting the motion of a single particle.

   Considering the stochastic nature of bed load transport, time-averaged bed load transport rates can be biased to varying degrees depending on the chosen time interval (Ancey and Pascal, 2020). To address this, it is recommended to analyze bed load transport (track bedforms and approximate roughness lengths) using orthomosaic photos and the elevation data measured by the ADVP.

3. **Study the combined effects of shells and bedforms on bed roughness over time**

   This study shows the influence of shells, of different shapes and sizes, on bed roughness. However, it is essential to consider that bed roughness may be altered over time. For example, bedforms can increase the friction factor and, subsequently, the bed shear stress due to form roughness (Van Rijn, 1993). By analyzing the ADVP data, which provides insight into the near-bed flow velocities and bed elevation, it would be possible to determine the influence of shells on bed roughness over time.

4. **Study the effect of shell cover on sediment transport**

   The presence of shells on the sediment surface reduces the availability of sediment for transport. However, it is essential to consider that shell cover may change over time. For example, factors such as bedform migration or flow acceleration in front of the shells can decrease shell cover or expose shells to the surface through scouring. To research the effect of changing shell cover, it is recommended to analyze the orthomosaic photos.

5. **Study flow around a cluster of shells in a high resolution**

   The flow characteristics around a cluster of shells differ from those around a single isolated shell. The obtained results, specifically the observed increase in turbulence intensities for *E. leei* shells at a shell content of 20%, underline the need to research the source of this turbulence generation or dissipation. An analysis of the orthomosaic photos facilitates the visualization and identification of spatial patterns and trends related to shell orientation. However, more controlled measurements are needed to accurately characterize the flow characteristics.

6. **Explore the connection with field data**

   A series of field investigations conducted by Black et al. (1989) in Whangarei Harbour, northeast New Zealand, revealed that sediment-shell mixtures have a significant influence on sediment transport, prohibiting transport even when the flow velocity exceeded the threshold for sandy

sediments. Using a numerical hydrodynamic model, the location of shell and sand beds was explained in terms of spatial changes to sediment transport capacity. Our experimental research revealed a similar link between shells and sediment transport for shell species abundant along the Dutch shoreline. Exploring the connection with field data is recommended to validate the research findings further.

For example, in a recent field study, Holzhauer et al. (2022) studied the ebb-tidal delta of Ameland, the Netherlands, focusing on the spatial patterns of benthic communities. Their study identified several dominant bivalve species, including *E. leei*, *Macoma balthica*, and *S. subtruncata*. Given that two of these species coincide with the ones studied in this research, this location presents a good starting point for exploring connections with field data.

Bibliography

Adobe Inc. (2023). Adobe Premiere Pro 2023 (23.2).

Ancey, C. and Pascal, I. (2020). Estimating Mean Bedload Transport Rates and Their Uncertainty. *Journal of Geophysical Research: Earth Surface*, 125(7):e2020JF005534.

Bagnold, R. A. (1956). The flow of cohesionless grains in fluids. *Philosophical Transactions of the Royal Society of London. Series A, Mathematical and Physical Sciences*, 249(964):235–297.

Bagnold, R. A. (1966). An Approach to the Sediment Transport Problem from General Physics. *USGS Professional Paper*.

Ballio, F., Nikora, V., and Coleman, S. E. (2014). On the definition of solid discharge in hydro-environment research and applications. *Journal of Hydraulic Research*, 52(2):173–184.

Beets, D. J. and Van Der Spek, A. J. F. (2000). The Holocene evolution of the barrier and the back-barrier basins of Belgium and the Netherlands as a function of late Weichselian morphology, relative sea-level rise and sediment supply. *Geologie en Mijnbouw/Netherlands Journal of Geosciences*, 79(1):3 – 16.

Bendixen, M., Iversen, L. L., Best, J., Franks, D. M., Hackney, C. R., Latrubesse, E. M., and Tusting, L. S. (2021). Sand, gravel, and UN Sustainable Development Goals: Conflicts, synergies, and pathways forward. *One Earth*, 4(8):1095–1111.

Black, K. P., Healy, T. R., and Hunter, M. G. (1989). Sediment dynamics in the lower section of a mixed sand and shell- lagged tidal estuary, New Zealand. *Journal of Coastal Research*, 5(3).

Bosboom, J. and Stive, M. J. (2023). *Coastal Dynamics*. TU Delft Open, Delft, 1.2 edition.

Bouma, T. J., van Duren, L. A., Temmerman, S., Claverie, T., Blanco-Garcia, A., Ysebaert, T., and Herman, P. M. (2007). Spatial flow and sedimentation patterns within patches of epibenthic structures: Combining field, flume and modelling experiments. *Continental Shelf Research*, 27(8):1020–1045.

Brand, E., Ramaekers, G., and Lodder, Q. (2022). Dutch experience with sand nourishments for dynamic coastline conservation – An operational overview. *Ocean & Coastal Management*, 217:106008.

Brayshaw, A. C., Frostick, L. E., and Reid, I. (1983). The hydrodynamics of particle clusters and sediment entrapment in coarse alluvial channels. *Sedimentology*, 30(1).

Breusers, H. and Schukking, W. (1969). Begin van beweging van bodemmateriaal [Beginning of bed load movement]. Technical report, Delft Hydraulics, Delft.

Bridge, J. S. and Bennett, S. J. (1992). A model for the entrainment and transport of sediment grains of mixed sizes, shapes, and densities. *Water Resources Research*, 28(2):337–363.

Celik, A. O., Diplas, P., Dancey, C. L., and Valyrakis, M. (2010). Impulse and particle dislodgement under turbulent flow conditions. *Physics of Fluids*, 22(4).

Cheng, C. H., de Smit, J. C., Fivash, G. S., Hulscher, S. J. M. H., Borsje, B. W., and Soetaert, K. (2021). Sediment shell-content diminishes current-driven sand ripple development and migration. *Earth Surface Dynamics*, 9(5):1335–1346.

Curran, J. C. and Tan, L. (2014). Effect of Bed Sand Content on the Turbulent Flows Associated with Clusters on an Armored Gravel Bed Surface. *Journal of Hydraulic Engineering*, 140(2).

De Jong, M. F. (2016). *The ecological effects of deep sand extraction on the Dutch continental shelf. Implications for future extraction*. PhD thesis, Wageningen University.

De Ruiter, J. C. C. (1980). 'Stochastic model for incipient motion of sediment grains as a function of local parameters. *Rep. No. R657-XI*.

Deltares (2020). Technisch Advies Sedimentbehoefte Kustfundament; ten behoeve van het beleidsadvies Kustgenese 2.0 [Technical Advice Sediment Needs Coastal Foundation: for the benefit of the policiy advice Kustgenese 2.0], authors Arno Nolte, Claire van Oeveren, Jebbe van der Werf, Pieter Koen Tonnon, Bart Grasmeijer, Ad van der Spek, Edwin Elias and Zheng Wang. Technical report, Deltares.

Dey, S. (2003). Incipient Motion of Bivalve Shells on Sand Beds under Flowing Water. *Journal of Engineering Mechanics*, 129(2).

Dey, S., Ali, S. Z., and Padhi, E. (2019). Bedload transport from analytical and turbulence phenomenological perspectives.

Diedericks, G. P. J., Troch, C. N. A., and Smit, G. J. F. (2018). Incipient Motion of Shells and Shell Gravel. *Journal of Hydraulic Engineering*, 144(3).

Doroudian, B., Bagherimiyab, F., and Lemmin, U. (2010). Improving the accuracy of four-receiver acoustic Doppler velocimeter (ADV) measurements in turbulent boundary layer flows. *Limnology and Oceanography: Methods*, 8(11):575–591.

Einstein, H. A. and Banks, R. B. (1950). Fluid resistance of composite roughness. *Eos, Transactions American Geophysical Union*, 31(4).

Fick, C., Puhl, E., and Toldo, E. E. (2020). Threshold of motion of bivalve and gastropod shells under oscillatory flow in flume experiments. *Sedimentology*, 67(1).

Folkard, A. M. (2011). Vegetated flows in their environmental context: A review.

Friedrichs, M., Graf, G., and Springer, B. (2000). Skimming flow induced over a simulated polychaete tube lawn at low population densities. *Marine Ecology Progress Series*, 192.

Friedrichs, M., Leipe, T., Peine, F., and Graf, G. (2009). Impact of macrozoobenthic structures on near-bed sediment fluxes. *Journal of Marine Systems*, 75(3-4):336–347.

Gijón Mancheño, A., Jansen, W., Winterwerp, J. C., and Uijttewaal, W. S. (2021). Predictive model of bulk drag coefficient for a nature-based structure exposed to currents. *Scientific Reports*, 11(1).

Gittenberger, A. and Loon, W. M. G. M. (2011). Common Marine Macrozoobenthos Species in the Netherlands, their Characteristics and Sensitivities to Environmental Pressures.

Gomez, B. (1978). Flume. In *Sedimentology*, pages 487–489. Springer Berlin Heidelberg, Berlin, Heidelberg.

Gutiérrez, J. L., Jones, C. G., Strayer, D. L., and Iribarne, O. O. (2003). Mollusks as ecosystem engineers: the role of shell production in aquatic habitats. *Oikos*, 101(1):79–90.

Holzhauer, H., Borsje, B. W., Herman, P. M., Schipper, C. A., and Wijnberg, K. M. (2022). The geomorphology of an ebb-tidal-delta linked to benthic species distribution and functionality. *Ocean and Coastal Management*, 216.

Huisman, B. J., de Schipper, M. A., and Ruessink, B. G. (2016). Sediment sorting at the Sand Motor at storm and annual time scales. *Marine Geology*, 381.

ICES (2016). Report of the Working Group on the Effects of Extraction of Marine Sediments on the Marine Ecosystem (WGEXT).

Kaplan, D. L. (1998). Mollusc shell structures: novel design strategies for synthetic materials. *Current Opinion in Solid State and Materials Science*, 3(3):232–236.

Kennedy, W. J., Taylor, J. D., and Hall, A. (1969). Environmental and biological controls on bivalve shell mineralogy. *Biological Reviews*, 44(4):499–530.

Kleinhans, M. G. and Grasmeijer, B. T. (2006). Bed load transport on the shoreface by currents and waves. *Coastal Engineering*, 53(12).

Kleinhans, M. G. and van Rijn, L. C. (2002). Stochastic Prediction of Sediment Transport in Sand-Gravel Bed Rivers. *Journal of Hydraulic Engineering*, 128(4).

Komar, P. D. and Clemens, K. E. (1986). The relationship between a grain's settling velocity and threshold of motion under unidirectional currents. *Journal of Sedimentary Petrology*, 56(2):258 – 266.

Kumagai, T. and Nakajima, S. (2012). Experimental Study on Bed Load Transport of Shell Fragment-Mixed Sand under Waves. *The International Journal of Ocean and Climate Systems*, 3(2):85–96.

Luijendijk, A., Hagenaars, G., Ranasinghe, R., Baart, F., Donchyts, G., and Aarninkhof, S. (2018). The State of the World's Beaches. *Scientific Reports*, 8(1).

Mayaud, J. R., Wiggs, G. F., and Bailey, R. M. (2016). Dynamics of skimming flow in the wake of a vegetation patch. *Aeolian Research*, 22.

McCarron, C. J., Van Landeghem, K. J., Baas, J. H., Amoudry, L. O., and Malarkey, J. (2019). The hiding-exposure effect revisited: A method to calculate the mobility of bimodal sediment mixtures. *Marine Geology*, 410:22–31.

McCave, I. N., Bryant, R. J., Cook, H. F., and Coughanowr, C. A. (1986). Evaluation of a laser-diffraction-size analyzer for use with natural sediments. *Journal of Sedimentary Research*, 56(4):561–564.

McLachlan, A. and Defeo, O. (2018). Introduction. *The Ecology of Sandy Shores*, pages 1–3.

Meyer-Peter, E. and Müller, R. (1948). Formulas for Bed-Load Transport. *International Association for Hydraulic Structures Research*, pages 39–64.

Miedema, S. and Ramsdell, R. (2011). Hydraulic transport of sand/shell mixtures in relation with the critical velocity. *Terra et Aqua*, 122.

Ministerie van Infrastructuur en Milieu (2015). Nationaal Waterplan 2016-2021 [National Water Plan 2016-2021]. Technical report, Ministerie van Infrastructuur en Milieu.

Morris, H. M. (1955). Flow in Rough Conduits. *Transactions of the American Society of Civil Engineers*, 120(1).

Naturalis Biodiversity Center (2022). Beach Shell Count.

Newell, A. J., Gower, D. J., Benton, M. J., and Tverdokhlebov, V. P. (2007). Bedload abrasion and the in situ fragmentation of bivalve shells. *Sedimentology*, 54(4).

Nezu, I. and Nakagawa, H. (1993). *Turbulence in open channel flows*. A.A.Balkema.

Nortek AS (2020). Nortek Manuals: The Comprehensive Manual for Velocimeters.

Nowell, A. R. and Church, M. (1979). Turbulent flow in a depth-limited boundary layer. *Journal of Geophysical Research*, 84(C8).

Nowell, A. R. and Jumars, P. A. (1984). Flow environments of aquatic benthos. *Annual review of ecology and systematics. Vol. 15*.

Olivera, A. M. and Wood, W. L. (1997). Hydrodynamics of bivalve shell entrainment and transport. *Journal of Sedimentary Research*, 67(3):514–526.

Paphitis, D., Collins, M. B., Nash, L. A., and Wallbridge, S. (2002). Settling velocities and entrainment thresholds of biogenic sands (shell fragments) under unidirectional flow. *Sedimentology*, 49(1):211–225.

Pearson, S. G., van Prooijen, B. C., Poleykett, J., Wright, M., Black, K., and Wang, Z. B. (2021). Tracking fluorescent and ferrimagnetic sediment tracers on an energetic ebb-tidal delta to monitor grain size-selective dispersal. *Ocean and Coastal Management*, 212.

Peduzzi, P. (2014). Sand, rarer than one thinks. *Environmental Development*, 11:208–218.

Perry, A. E., Lim, K. L., and Henbest, S. M. (1987). An experimental study of the turbulence structure in smooth- and rough-wall boundary layers. *Journal of Fluid Mechanics*, 177(10).

Perry, A. E., Schofield, W. H., and Joubert, P. N. (1969). Rough wall turbulent boundary layers. *Journal of Fluid Mechanics*, 37(2).

Peterson, C. H., Hickerson, D. H. M., and Johnson, G. G. (2000). Short-Term Consequences of Nourishment and Bulldozing on the Dominant Large Invertebrates of a Sandy Beach. *Journal of Coastal Research*, 16(2):368–378.

Prager, E. J., Southard, J. B., and Vivoni-Gallart, E. R. (1996). Experiments on the entrainment threshold of well-sorted and poorly sorted carbonate sands. *Sedimentology*, 43(1):33–40.

Rieux, A., Weill, P., Mouazé, D., Poirier, C., Nechenache, F., Perez, L., and Tessier, B. (2018). Threshold of motion and settling velocities of mollusc shell debris: Influence of faunal composition. *Sedimentology*, 66.

Sentker, A. and Riess, W. (1999). Experimental Investigation of Turbulent Wake-Blade Interaction in Axial Compressors. *Engineering Turbulence Modelling and Experiments 4*, pages 731–740.

Shields, I. A. (1936). Anwendung der Aehnlichkeitsmechanik und der Turbulenzforschung auf die Geschiebebewegung [Application of similarity principles and turbulence research to bed-load movement]. Technical report, Preußischen Versuchsanstalt fur Wasserbouw.

Shih, W. and Diplas, P. (2018). A Unified Approach to Bed Load Transport Description Over a Wide Range of Flow Conditions via the Use of Conditional Data Treatment. *Water Resources Research*, 54(5):3490–3509.

Silva, F., Borges, A. L., Jr, E., Fick, C., Puhl, E., Oliveira, V., and Cruz, F. (2023). Threshold of motion and orientation of bivalve shells under current flow. *Brazilian Journal of Geology*, 53.

Smaal, A. C., Ferreira, J. G., Grant, J., Petersen, J. K., and Strand, Ø. (2019). *Goods and Services of Marine Bivalves*. Springer International Publishing.

Soulsby, R. (1997). *Dynamics of marine sands: a manual for practical applications*. Thomas Telford Publications.

Soulsby, R. L. and Whitehouse, R. (1997). *Threshold of Sediment Motion in Coastal Environments*. Centre for Advanced Engineering, University of Canterbury.

Tan, L. and Curran, J. C. (2012). Comparison of Turbulent Flows over Clusters of Varying Density. *Journal of Hydraulic Engineering*, 138(12).

Uphues, C. F., van IJzendoorn, C. O., Hallin, C., Pearson, S. G., van Prooijen, B. C., Miot da Silva, G., and de Vries, S. (2022). Coastal aeolian sediment transport in an active bed surface layer: Tracer study and conceptual model. *Earth Surface Processes and Landforms*, 47(13).

Van Aken, H. M. (2008). Variability of the salinity in the western Wadden Sea on tidal to centennial time scales. *Journal of Sea Research*, 59(3).

Van der Meulen, M. J., van der Spek, A. J. F., de Lange, G., Gruijters, S. H. L. L., van Gessel, S. F., Nguyen, B.-L., Maljers, D., Schokker, J., Mulder, J. P. M., and van der Krogt, R. A. A. (2007). Regional Sediment Deficits in the Dutch Lowlands: Implications for Long-Term Land-Use Options (8 pp). *Journal of Soils and Sediments*, 7(1):9–16.

Van der Spek, A. J. F. and Lodder, Q. J. (2015). A new sediment budget for The Netherlands; the effects of 15 years of nourishing (1991-2005). In *Coastal Sediments 2015*. Word Scientifc Publishing, Singapore, 2015.

Van der Wal, D. (2000). Grain-Size-Selective Aeolian Sand Transport on a Nourished Beach. *Journal of Coastal Research*, 16(3):896–908.

Van Rijn, L. C. (1984). Sediment Transport, Part I: Bed Load Transport. *Journal of Hydraulic Engineering*, 110(10):1431–1456.

Van Rijn, L. C. (1993). Principles of Sediment Transport in Rivers, Estuaries and Coastal Seas. *Principles of Sediment Transport in Rivers , Estuaries and Coastal Seas*.

Van Rijn, L. C. (1997). Sediment transport and budget of the central coastal zone of Holland. *Coastal Engineering*, 32(1):61–90.

Vanoni, V. A. (1941). Velocity Distribution in Open Channels. In *Hydrodynamics Laboratory*. California Institute of Technology.

Vanoni, V. A. (1975). *Sedimentation Engineering*. American Society of Civil Engineers.

Vanoni, V. A. and Brooks, N. (1957). Laboratory Studies of the Roughness and Suspended Load of Alluvial Streams. *California Institute of Technology*, E-68(December).

Verhaegen, G., Herzog, H., Korsch, K., Kerth, G., Brede, M., and Haase, M. (2019). Testing the adaptive value of gastropod shell morphology to flow: A multidisciplinary approach based on morphometrics, computational fluid dynamics and a flow tank experiment. *Zoological Letters*, 5(1).

Wong, M. and Parker, G. (2006). Reanalysis and Correction of Bed-Load Relation of Meyer-Peter and Müller Using Their Own Database. *Journal of Hydraulic Engineering-asce - J HYDRAUL ENG-ASCE*, 132.

Yang, J. Q. and Nepf, H. M. (2018). A Turbulence-Based Bed-Load Transport Model for Bare and Vegetated Channels. *Geophysical Research Letters*, 45(19).

A

Material characteristics

This chapter describes the material characteristics used during the experiments. Section A.1 presents the sediment characteristics. Two separate measurements were taken to (i) determine the main morphometry of the bivalve shells (Section A.2), and (ii) determine the density of the shells concerning the North Sea sandy sediment and shell fragments (Section A.3).

A.1. Sediment characteristics

North Sea sandy sediment was used during the experiment. Two large bags of sand, approximately one m^3 each, were acquired from De Houtkaai B.V. in Goes, the Netherlands. The particle size of the sediment was determined using a Mastersizer 2000 from Malvern Instruments. Table A.1 shows the result of the analysis. The medium grain size was roughly 348 µm. Further results indicate that the sand could mainly be classified as medium sand (Table A.2).

Table A.1: Grain size characteristics of the North Sea sandy sediment used during the experiments, sampled at three different instances.

Sample	Description	Grain size (μm)		
		d_{10}	d_{50}	d_{90}
1	At sand depot	231.40	347.36	524.16
2	Big bag 1	231.94	348.28	526.61
3	Big bag 2	232.48	348.54	523.76

Table A.2: Grain size distribution of the North Sea sandy sediment used during the experiments, sampled at three different instances.

	Sand classification				
Sample	Silt (%)	Very fine (%)	Fine (%)	Medium (%)	Coarse (%)
	(63 μm)	(62.5-125 μm)	(125-250 μm)	(250-500 μm)	(500-1000 μm)
1	0.00	0.00	15.26	71.77	12.97
2	0.00	0.00	15.09	71.66	13.26
3	0.00	0.00	14.92	72.11	12.97

A.2. Shell characteristics

For this study, two distinct species of bivalve species were chosen, specifically *Ensis leei* and *Spisula subtruncata*. A significant number of shell valves of the two bivalve shells were chosen and then divided into ten equal stacks. Ten shell valves were randomly selected from each stack, resulting in a total sample size of 100 shell valves for each species. The shell valves' main morphometry (shape and size) was determined using a digital caliper from Duro with a 0.01 mm resolution. Measurements were taken following Vanoni (1975) in which he defines the length, width, and height as the longest,

intermediate, and smallest dimensions along three mutually perpendicular axes. The *S. subtruncata* is often considered as an ellipse (e.g., Dey, 2003). Therefore an additional measurement was carried out to measure the inner width. Furthermore, the shell thickness was determined. The weight of the individual valves was determined using a precision scale. The results are shown in Table A.3.

Table A.3: Representative measurements of the shell valves used in the experiments.

Species	**Nr**	**Mean (± SD)**					
		Length (mm)	**Width (mm)**	**Inner width (mm)**	**Height (mm)**	**Thickness (mm)**	**Weight (g)**
Ensis leei	100	106.54 (± 8.66)	16.83 (± 1.70)	-	5.15 (± 0.55)	0.59 (± 0.08)	3.02 (± 0.68)
Spisula subtruncata	100	28.64 (± 1.97)	20.02 (± 1.40)	16.68 (± 1.35)	7.29 (± 0.73)	1.05 (± 0.17)	1.49 (± 0.45)

Table A.3 demonstrates a noteworthy dissimilarity in the mean weight of shell species, although their shell thickness is comparable. Additionally, the outcomes were illustrated using boxplots. Figure A.1 shows the boxplots for the *Ensis leei* shell valves and Figure A.2 for the *Spisula subtruncata* shell valves. Other measurements, such as length and height, show a wide distribution (Figure A.3).

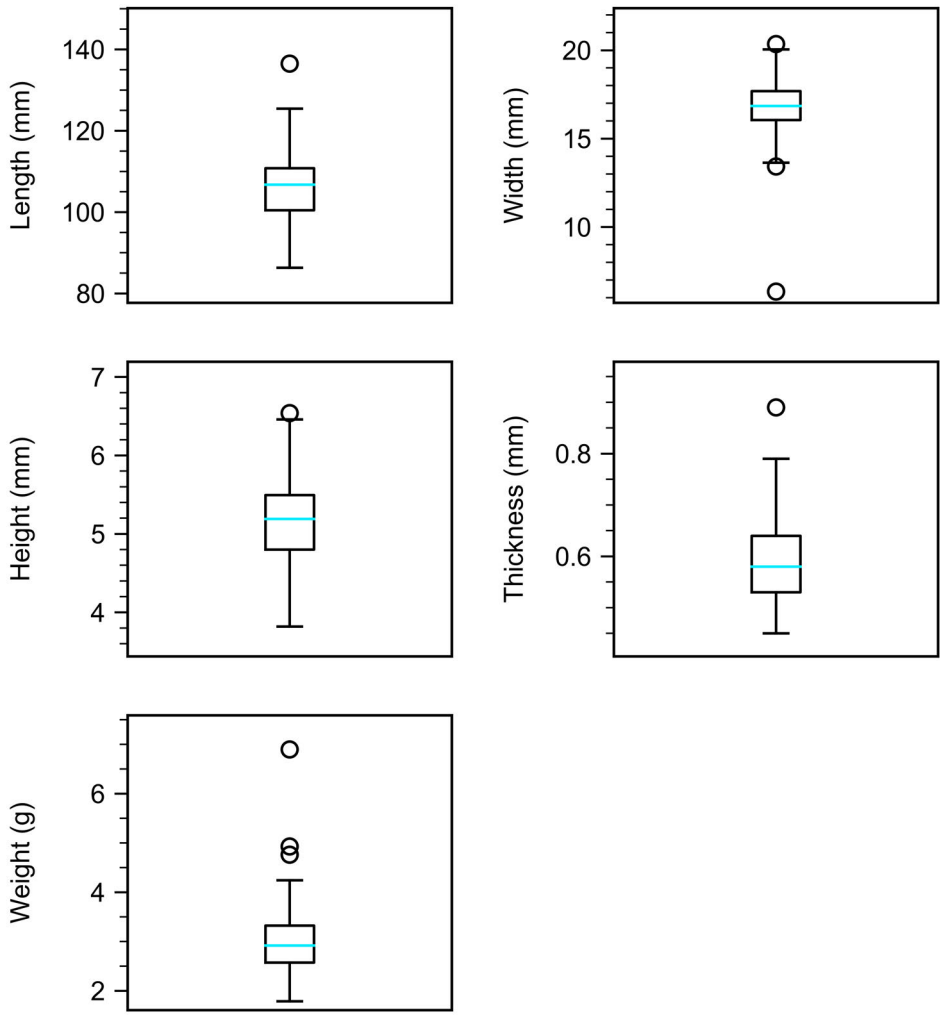

Figure A.1: Boxplots showing varying shell valve characteristics of *Ensis leei*.

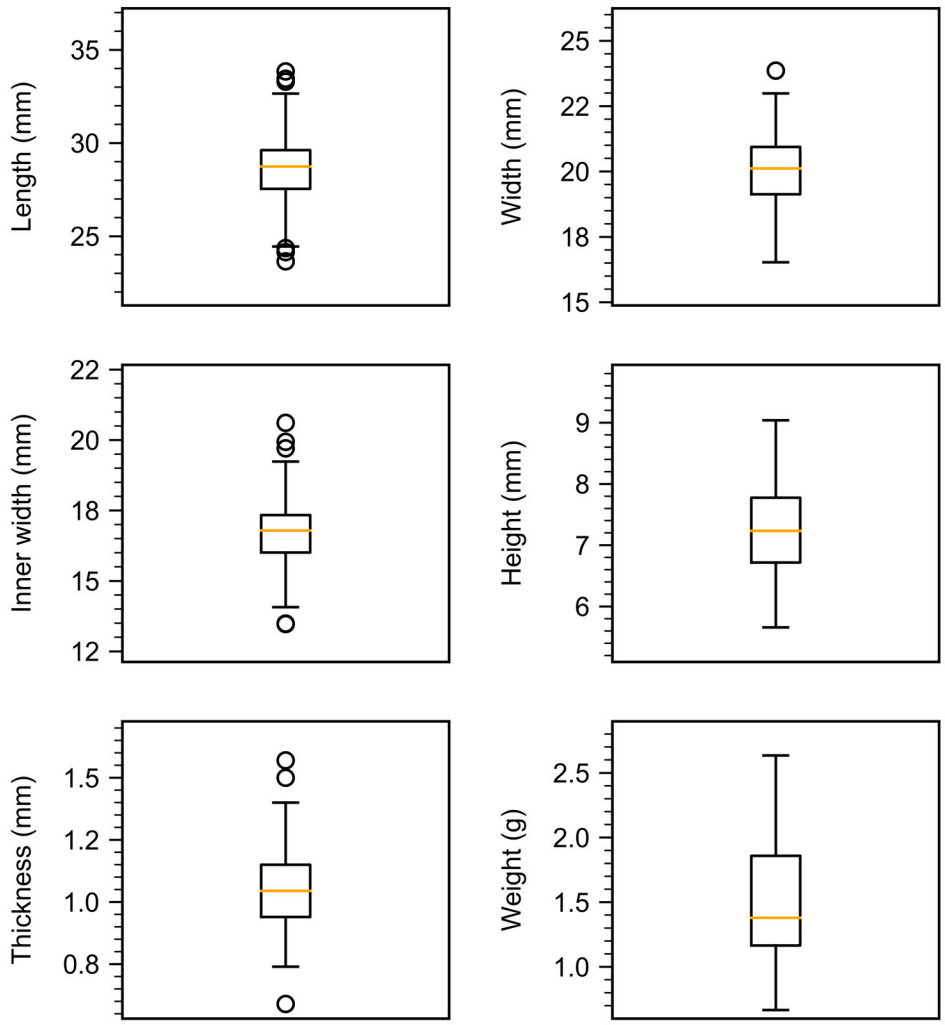

Figure A.2: Boxplots showing varying shell valve characteristics of *Spisula subtruncata*.

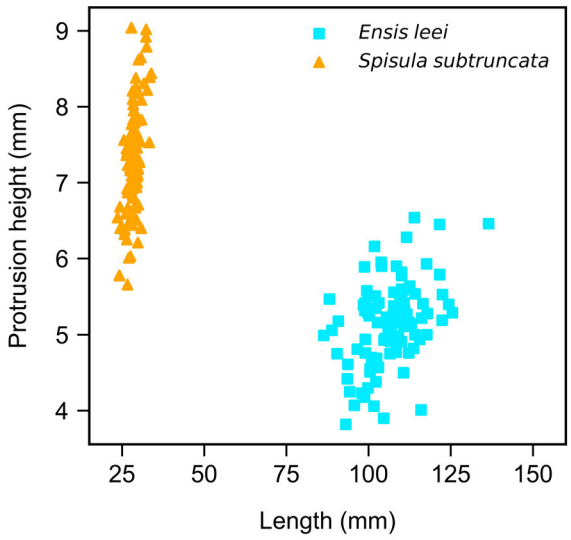

Figure A.3: Measured height versus length for whole shell valves.

A.3. Density analysis

For this study, the different materials used were: (i) North Sea sandy sediment, (ii) valves of bivalve shells, and (iii) fragments of shells. In line with the information presented in Section A.1 and Section A.2, the shape and size of siliciclastic grains differ significantly from those of carbonate shells. Density, shape, and size play an important role in sediment entrainment thresholds (Komar and Clemens, 1986), determining whether the sediment is carried as bed load or suspension load (Van Rijn, 1997). Therefore, a pycnometer was used to measure the density of the materials.

In this particular experiment, a glass pycnometer (along with a glass stopper) with a precisely measured volume of 99.4 ml (V_{py}) was used. The following measurement procedure was carried out:

1. Measure the mass of the empty, clean, and dry pycnometer: m_{py}
2. Fill the pycnometer with water; dry off any excess water, and measure the mass again: $m_{py,w}$
3. Prepare the materials by using a pestle to grind the bivalve shell valves
4. Fill the pycnometer to the top with the sediment, crushed shell valves, or shell fragments
5. Dry off any excess water and again measure the mass of the pycnometer: $m_{py,w,m}$
6. Measure the mass of the empty drying pan: m_{pan}
7. Collect the sediment, crushed shell valves, or shell fragments from the pycnometer in the drying pan
8. Dry the materials in an oven and, once cooled off, measure the mass of the pan containing the dry materials: $m_{pan,m}$

The above-mentioned procedure was carried out twice for each material, resulting in 10 measurements. Table A.4 presents the resulting measurements.

Table A.4: Measurements of the pycnometer and pan as described in the measurement procedure.

Materials sediment-shell mixture	**Nr**	V_{py} **(ml)**	m_{py} **(g)**	$m_{py,w}$ **(g)**	$m_{py,w,m}$ **(g)**	m_{pan} **(g)**	$m_{pan,m}$ **(g)**
Sandy sediment	1	99.4	45.4	143.6	243.6	6.0	165.4
Sandy sediment	2	99.4	45.4	143.6	243.0	6.0	163.8
Ensis leei	1	99.4	46.7	143.7	223.4	6.0	126.8
Ensis leei	2	99.4	45.4	143.8	223.0	6.4	128.2
Spisula subtruncata	1	99.4	46.6	143.8	217.8	6.2	125.8
Spisula subtruncata	2	99.4	45.6	143.8	222.8	6.0	126.2
Fragments 2-4 mm	1	99.4	45.6	143.8	223.2	6.2	129.2
Fragments 2-4 mm	2	99.4	45.6	143.8	223.4	6.0	129.6
Fragments <2 mm	1	99.4	46.7	143.8	222.8	6.2	140.2
Fragments <2 mm	2	99.4	45.6	143.8	223.0	6.4	143.8

Using the measurement data from Table A.4, the mass of the water inside the pycnometer m_w can be calculated using the following equations:

$$m_w = m_{py,w} - m_{py} \tag{A.1}$$

Using Equation A.1, a validation check can be done by calculating the density of water $\rho_{w,c}$ using Equation A.2. This calculated value can then be compared with the theoretical density of water $\rho_{w,t}$ at 20°C. Table A.5 shows the results of this comparison.

$$\rho_{w,c} = \frac{m_w}{V_{py}} \tag{A.2}$$

Table A.5: Validation check confirming the density of water with the measured mass of the water.

Materials sediment-shell mixture	Nr	V_{py} (ml)	m_w (g)	Check		
				$\rho_{w,c}$ (g/ml)	$\rho_{w,t}$ (g/ml)	
Sandy sediment	1	99.4	98.2	0.988	0.998	✓
Sandy sediment	2	99.4	98.2	0.988	0.998	✓
Ensis leei	1	99.4	97.0	0.976	0.998	✓
Ensis leei	2	99.4	98.4	0.990	0.998	✓
Spisula subtruncata	1	99.4	97.2	0.978	0.998	✓
Spisula subtruncata	2	99.4	98.2	0.988	0.998	✓
Fragments 2-4 mm	1	99.4	98.2	0.988	0.998	✓
Fragments 2-4 mm	2	99.4	98.2	0.988	0.998	✓
Fragments <2 mm	1	99.4	97.1	0.977	0.998	✓
Fragments <2 mm	2	99.4	98.2	0.988	0.998	✓

To obtain the density and bulk density of the material, the following values have to be derived: (1) the mass of the dry material m_m (Equation A.3), and (2) the volume of the material V_m (Equation A.4).

$$m_m = m_{pan,m} - m_{pan} \tag{A.3}$$

$$V_m = V_{py} - \frac{m_{py,w,m} - m_{py} - m_m}{\rho_w} \tag{A.4}$$

A material's density (ρ) is defined as the ratio of its mass to its volume. For particles or chunks of material, the bulk density (ρ_{bulk}) is often used. Bulk density measures how much space a given material occupies in its natural state, including the interstitial spaces between particles. It is defined as the mass of a material divided by its bulk volume. The density and bulk density can be calculated using Equation A.5 and Equation A.6, respectively.

$$\rho = \frac{m_{m,dry}}{V_m} \tag{A.5}$$

$$\rho_{bulk} = \frac{m_{m,dry}}{V_{py}} \tag{A.6}$$

The density and bulk density calculation results are shown in Table A.6. Figure A.4 plots the density values for each material. The results indicate that the density of the North Sea sandy sediment corresponds to typical density values for sediment (i.e., 2650 kg m^{-3}). Additionally, the bulk density of the carbonate shells is considerably lower than the bulk density of the sediment. This supports Soulby's claim that the presence of shells reduces the bulk density of the sediment by diluting the quartz fraction (Soulsby, 1997).

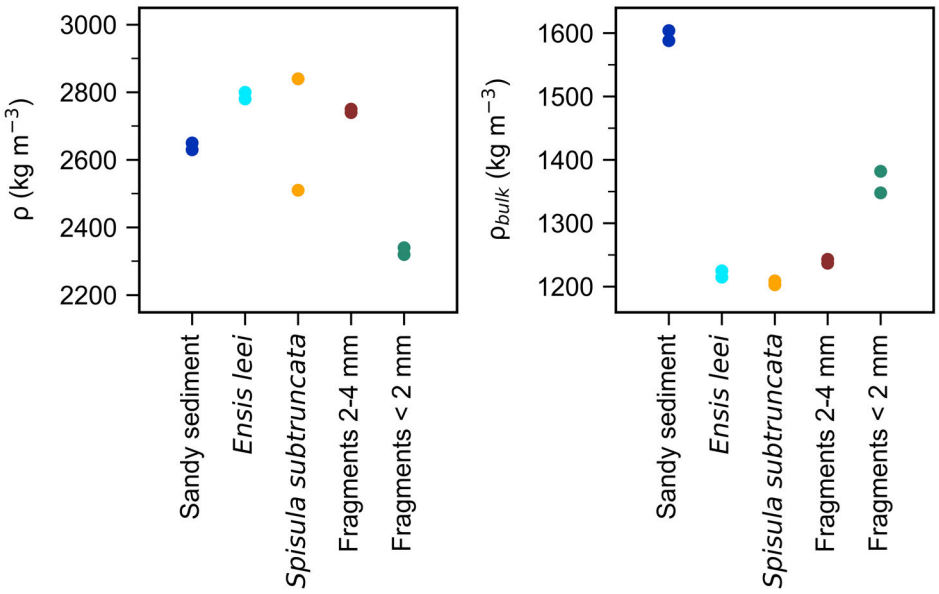

Figure A.4: Density and bulk density of materials.

Table A.6: Results of the density analysis.

Materials sediment-shell mixture	**Nr**	V_{py} **(ml)**	m_{py} **(g)**	$m_{py,w,m}$ **(g)**	m_{pan} **(g)**	$m_{pan,s}$ **(g)**	m_m **(g)**	ρ_w **(g/ml)**	m_m **(ml)**	ρ **(g/ml)**	ρ_{bulk} **(g/ml)**
Sandy sediment	1	99.4	45.4	243.6	6.0	165.4	159.4	0.998	60.53	2.63	1.604
Sandy sediment	2	99.4	45.4	243.0	6.0	163.8	157.8	0.998	59.53	2.65	1.588
Ensis leei	1	99.4	46.7	223.4	6.0	126.8	120.8	0.998	43.40	2.78	1.215
Ensis leei	2	99.4	45.4	223.0	6.4	128.2	121.8	0.998	43.50	2.80	1.225
Spisula subtruncata	1	99.4	46.6	217.8	6.2	125.8	119.6	0.998	47.71	2.51	1.203
Spisula subtruncata	2	99.4	45.6	222.8	6.0	126.2	120.2	0.998	42.30	2.84	1.209
Fragments 2-4 mm	1	99.4	45.6	223.2	6.2	129.2	123.0	0.998	44.70	2.75	1.237
Fragments 2-4 mm	2	99.4	45.6	223.4	6.0	129.6	123.6	0.998	45.10	2.74	1.243
Fragments <2 mm	1	99.4	46.7	222.8	6.2	140.2	134.0	0.998	57.22	2.34	1.348
Fragments <2 mm	2	99.4	45.6	223.0	6.4	143.8	137.4	0.998	59.33	2.32	1.382

B

Measurement instruments

This chapter contains a comprehensive list of all the measurement instruments used in the experiments, along with their corresponding manufacturers and serial numbers.

B.1. Flow velocity

The following measuring instruments have been used to measure the velocity of fluid flow:

Acoustic Doppler velocimeter (ADV)

Manufacturer:	Nortek AS
Serial number:	VNO 0750
Probe number:	VCN 9624
Measuring frequency:	25 Hz

Acoustic Doppler velocimeter Profiler (ADVP)

Manufacturer:	Nortek AS
Serial number:	VNO 1278
Probe number:	VCN 9143
Measuring frequency:	25 Hz

B.2. Pressure

The following measuring instruments have been used to measure the pressure:

Pressure Sensors (PS)

Manufacturer:	Drück Ltd, Baker Hughes
Series:	1800 series
Measuring frequency:	25 Hz

B.3. Cameras

The following cameras have been used to capture images and videos:

GoPro Hero8 Black

Manufacturer:	GoPro, Inc.
Project-ID:	Black UU
Serial number:	C3441327520911

GoPro Hero4 Silver

Manufacturer:	GoPro, Inc.
Project-ID:	SH
Serial number:	C3131126770958

GoPro Hero4 Silver

Manufacturer:	GoPro, Inc.
Project-ID:	UU
Serial number:	C3131126222002

GoPro Hero4 Session

Manufacturer:	GoPro, Inc.
Project-ID:	8
Serial number:	C3141328270234

GoPro Hero4 Session

Manufacturer:	GoPro, Inc.
Project-ID:	18
Serial number:	C3141328271236

GoPro Hero4 Session

Manufacturer:	GoPro, Inc.
Project-ID:	23
Serial number:	C3141328418961

B.4. Particle size

The following instruments have been used to determine the particle size of sediment:

Mastersizer 2000

Manufacturer:	Malvern Instruments
Serial number:	34403/139
Model:	APA 2000, Hydro G 2000, Autosampler 2000

C

Experimental runs

This chapter contains an overview of all experimental runs for both the slowly accelerating and constant flow experiments.

C.1. Slowly accelerating flow experiment

Measurements have been conducted from the 12th of October 2022 until the 30th of November 2022. Table C.1 gives an overview of all nine experimental runs, including the availability of measurement data.

Table C.1: Overview of slowly accelerated flow experiments (P1). A checkmark indicates the availability of measurement data.

Experiment	Date	Cameras		OP	ADV	ADVP	PS
		Top view	Side view				
P1_0_00_R1	12 Oct 2022	✓	✓	✓	✓	✓	×
P1_E_10_R1	21 Nov 2022	✓	✓	✓	✓	×	✓
P1_E_20_R1	29 Nov 2022	✓	✓	✓	✓	×	✓
P1_M_05_R1	9 Nov 2022	✓	✓	✓	✓	✓	✓
P1_M_10_R1	25 Oct 2022	✓	✓	✓	✓	✓	✓
P1_M_20_R1	20 Oct 2022	✓	✓	✓	✓	✓	✓
P1_M_50_R1	17 Oct 2022	✓	✓	✓	✓	✓	✓
P1_S_10_R1	24 Nov 2022	✓	✓	✓	✓	×	✓
P1_S_20_R1	30 Nov 2022	✓	✓	✓	✓	×	✓

Note. E indicates an experiment where *Ensis leei* shells were used, S indicates that *Spisula subtruncata* shells were used. M indicates that a mixture of both shell species was used. The subsequent number indicates the shell content. The ADVP was employed throughout some, but not all, of the experimental runs.

C.2. Constant flow experiment

Measurements have been conducted from the 26th of October 2022 until the 1st of December 2022. Table C.2 gives an overview of all 24 experimental runs, including the target velocity and the availability of measurement data.

Table C.2: Overview of constant flow experiments (P2). A checkmark indicates the availability of measurement data.

Experiment	Date	Target ($m\ s^{-1}$)	Cameras		OP	ADV	ADVP	PS	CBL
			Top view	Side view					
P2_0_00_R1	14 Nov 2022	0.35	✓	✓	✓	✓	✓	✓	✓
P2_0_00_R2	15 Nov 2022	0.45	✓	✓	✓	✓	✓	✓	✓
P2_0_00_R3	15 Nov 2022	0.40	✓	×	✓	✓	✓	✓	✓
P2_0_00_R4	16 Nov 2022	0.30	✓	✓	✓	✓	×	✓	✓
P2_0_00_R5	17 Nov 2022	0.25	✓	✓	✓	✓	×	✓	✓
P2_E_10_R1	21 Nov 2022	0.35	✓	✓	✓	✓	×	✓	✓
P2_E_10_R2	22 Nov 2022	0.45	✓	✓	✓	✓	×	✓	✓
P2_E_10_R3	22 Nov 2022	0.40	✓	✓	✓	✓	×	✓	✓
P2_E_10_R4	23 Nov 2022	0.30	✓	✓	✓	✓	×	✓	✓
P2_E_10_R5	23 Nov 2022	0.25	✓	✓	✓	✓	×	✓	✓
P2_E_20_R1	29 Nov 2022	0.35	✓	✓	✓	✓	×	✓	✓
P2_E_20_R2	29 Nov 2022	0.45	✓	✓	✓	✓	×	✓	✓
P2_M_10_R1	26 Oct 2022	0.35	×	×	✓	✓	✓	✓	✓
P2_M_10_R2	27 Oct 2022	0.45	✓	✓	✓	✓	✓	✓	✓
P2_M_10_R3	27 Oct 2022	0.30	✓	✓	✓	✓	✓	×	✓
P2_M_10_R4	28 Oct 2022	0.40	✓	✓	✓	✓	✓	✓	✓
P2_M_10_R5	31 Oct 2022	0.25	✓	✓	✓	✓	✓	✓	×
P2_S_10_R1	24 Nov 2022	0.35	✓	✓	✓	✓	×	✓	✓
P2_S_10_R2	24 Nov 2022	0.45	✓	✓	✓	✓	×	✓	✓
P2_S_10_R3	25 Nov 2022	0.40	✓	✓	✓	✓	×	✓	✓
P2_S_10_R4	25 Nov 2022	0.30	✓	✓	✓	✓	×	✓	✓
P2_S_10_R5	28 Nov 2022	0.25	✓	✓	✓	✓	×	✓	✓
P2_S_20_R1	01 Dec 2022	0.35	✓	✓	✓	✓	×	✓	✓
P2_S_20_R2	01 Dec 2022	0.45	✓	✓	✓	✓	×	✓	✓

Note. E indicates an experiment where *Ensis leei* shells were used, S indicates that *Spisula subtruncata* shells were used. M indicates that a mixture of both shell species was used. The subsequent number indicates the shell content. BL indicates the collection of bed load transport. The ADVP was employed throughout some, but not all, of the experimental runs.

D

Flow stability

This chapter contains a brief description of known literature to determine the stability of grains exposed to currents (Section D.1) and the corresponding threshold of motion of sand grains (Section D.2). Section D.3 contains the derivation of the threshold of motion for sand grains. Lastly, Section D.4 contains the derivation of the bed shear stress.

D.1. Flow stability

The research of Albert F. Shields in 1936 is one of the best-known for describing the behaviour of grains exposed to currents. The Shields parameter expresses the ratio between load and strength, and it is defined as follows:

$$\theta = \frac{\tau_{cr}}{(\rho_s - \rho_w) g d} \tag{D.1}$$

In this fundamental research, Shields (1936) relates the critical Shields parameter θ_{cr} and the particle Reynolds number. The particle Reynolds number indicates whether the grain protrudes into the turbulent boundary layer and is defined as follows:

$$Re_* = \frac{u_{*_c} d}{\upsilon} \tag{D.2}$$

Van Rijn (1984) replaces the particle Reynolds number with a dimensionless particle diameter. The main advantage is the elimination of u_{*_c}, which avoids iteration. The dimensionless particle diameter is defined as:

$$d_* = d_{50} \left[\frac{g(s-1)}{\upsilon^2} \right]^{1/3} \tag{D.3}$$

D.2. Transport stages

In the previous section, a critical velocity was mentioned concerning stability. However, defining one critical velocity is complicated since the stability of every stone in the bed is different. This can be attributed to the irregularities of natural stones, the differing positions, and the differing protrusions in the bed. Therefore, Breusers and Schukking (1969) defined seven transport stages:

0. No movement at all
1. Occasional movement at some locations
2. Frequent movement at some locations
3. Frequent movement at several locations
4. Frequent movement at many locations

5. Frequent movement at all locations
6. Continuous movement at all locations
7. General transport of the grains

The threshold of motion remains a subjective matter when defining an experiment. Transport stage 6 seems to correspond well to the Shields criterion.

D.3. Derivation of the theoretical threshold of motion for sand grains

The first step to derive the threshold of motion of sand grains for the experiment is to determine the dimensionless particle diameter. Using the grain size characteristics of the North Sea sandy sediment used during the experiment (Table A.1 in Appendix A.1), and sandy sediment density (Table A.6 in Appendix A.3), a salinity of 30 parts-per-thousand (corresponding to approximately 1023 kg $m^{-}3$), and kinematic viscosity of 1.33×10^{-6} m^2 s^{-1}, Equation D.3 leads to a dimensionless particle diameter of 7.18.

The second step is to determine the critical Shields number. Transport stage 6, continuous movement at all locations, is considered for calculating the threshold of motion. An algebraic expression that fits the Shields curve proposed by Soulsby and Whitehouse (1997) is used to determine the critical Shields number:

$$\theta_{cr} = \frac{0.30}{1 + 1.2d_*} + 0.055\left[1 - \exp\left(-0.020d_*\right)\right] \tag{D.4}$$

Using Equation D.4, the critical shields number is 0.039. Throughout the experiment, an ADV measured the depth-averaged velocity. To define an offset velocity for the slowly acceleration flow experiment, the theoretical depth-averaged velocity for the threshold of motion was derived using Van Rijn (1993):

$$\bar{u}_{cr} = 5.7\left[\log\left(\frac{12h}{k_s}\right)\right]\left[\theta_{cr}(s-1)gd_{50}\right]^{0.5} \tag{D.5}$$

Using a water depth h of 0.35 m, $s = \rho_s/\rho_w$, and assuming a roughness k_r equal to $3d_{90}$, Equation D.5 leads to a depth-averaged velocity $\bar{u}_{cr}$ of 0.28 m s^{-1}.

D.4. Derivation of bed shear stress

The first step is to derive the critical bed shear stress. Bed shear stress is commonly expressed in terms of a friction coefficient (c_f), the fluid density (ρ_w), and the depth-averaged velocity ($\bar{u}$). Alternatively, it can be expressed in the shear velocity (u_*). The relationships between these quantities are given by the following expressions:

$$\tau_b = c_f\rho_w\bar{u}^2 = u_*^2\rho_w \tag{D.6}$$

Shear velocity is a representation of shear stress in units of velocity. Although it cannot be directly measured, it is linked to turbulent intensities near the bed. Nezu and Nakagawa (1993) established a relationship between turbulent intensities (u') and shear velocity:

$$\frac{u'}{u_*} = 2.30\exp\left(-\frac{z}{h}\right) \tag{D.7}$$

The relationship is constant at a specific height z above the bed. The turbulent intensities, measured at 0.37 × water depth above the bed, can be derived using the ADV data from the slowly accelerating flow experiment. Subsequently, the shear velocity and critical bed shear stress can be derived using Equation D.6 and Equation D.7, respectively.

$$u_* = \frac{u'}{2.30\exp\left(-\frac{0.37h}{h}\right)} \quad \rightarrow \quad \tau_{b,cr} = u_*^2\rho_w \tag{D.8}$$

The next step is to derive the bed shear stress for each collected bed load sample. The depth-averaged velocity is determined using the ADV data from the constant flow experiment. By rewriting

Equation D.6, the relationship between the relative turbulence and the friction coefficient at $y = 0.37h$ can be expressed as:

$$u_* = \sqrt{\frac{\tau_b}{\rho_w}} = \sqrt{c_f}\bar{u} \qquad \rightarrow \qquad \frac{u_*}{\bar{u}} = \sqrt{c_f} \qquad \rightarrow \qquad r_u = \frac{u'}{\bar{u}} \approx 1.59\sqrt{c_f} \tag{D.9}$$

The relative turbulence of the slowly accelerating flow experiment is used as an approximation to determine the friction coefficient c_f. Together, the depth-averaged velocity and friction velocity allow for the determination of the bed shear stress for each collected bed load sample using Equation D.6.

E

Data processing

This chapter describes the data processing for the slowly accelerating flow experiment and the constant flow experiment.

E.1. Slowly accelerating flow experiment

An analysis was conducted for the slowly accelerating flow experiment using the GoPro video recordings and the ADV data. The ADV data underwent two steps of processing: (1) bad-quality data was filtered out (Section E.1.2), and (2) spikes were removed from the velocity time series (Section E.1.3). Additionally, the quality of the GoPro video recordings was improved (Section E.1.1). Since it was impossible to switch on the ADV and GoPro cameras simultaneously, the time stamps of the ADV and GoPro videos were matched by examining the experiment's start and end points. The full process is illustrated in Figure E.1.

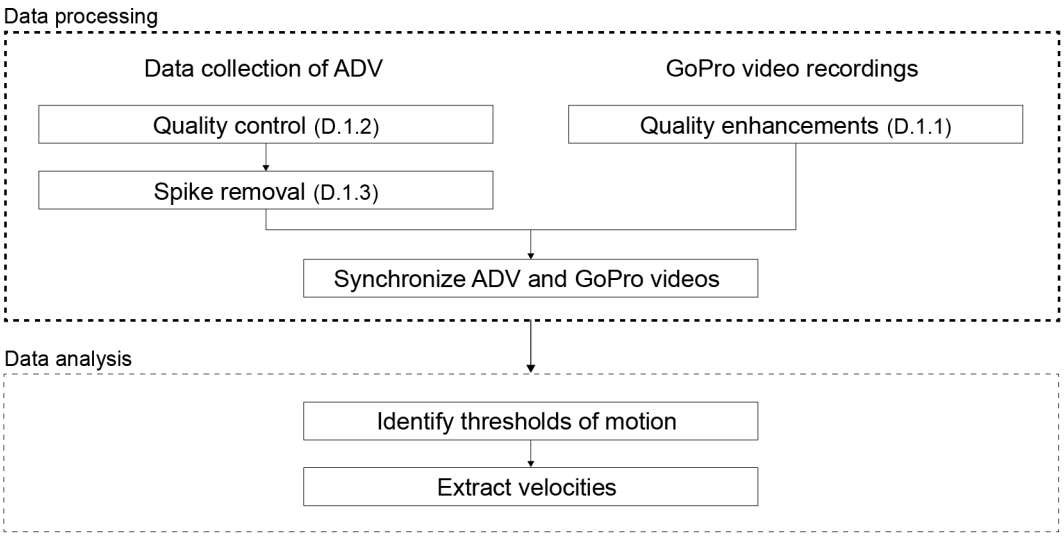

Figure E.1: Data processing procedure, along with the corresponding section in which an explanation will be provided.

E.1.1. GoPro video quality enhancements

Using Adobe Premiere Pro (Adobe Inc., 2023), the quality of the GoPro video recordings was improved by attempting various combinations of enhancements in a trial-and-error fashion. The final enhancements implemented included gamma correction +12, brightness -5.0, contrast -1.0, and sharpening +5.0. Furthermore, a timecode was added to the bottom left corner of the video. Figure E.2 compares the video quality before and after the enhancements.

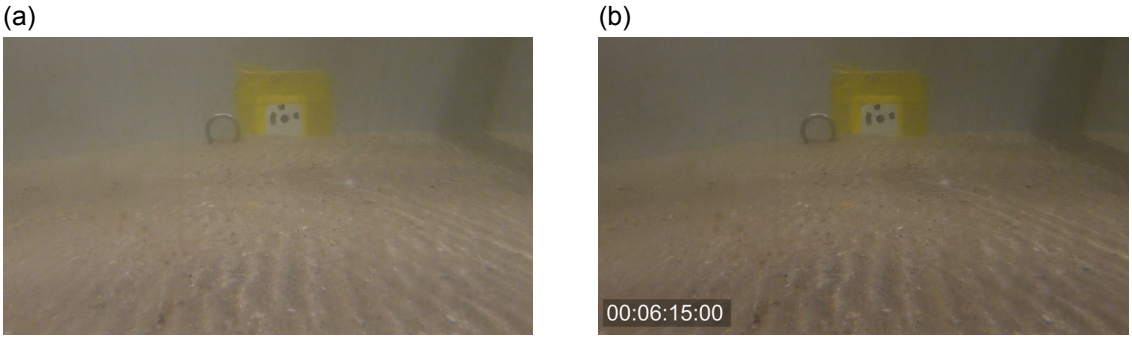

Figure E.2: Comparison of the video quality before (a) and after (b) enhancements.

E.1.2. Quality control of ADV data

In the process of data processing, checking data quality is an important aspect. In general, a lower correlation indicates more noise in the data. The correlation is a measure of the similarity of the two pulse echoes being measured. The signal-to-noise ratio (SNR) is calculated by subtracting the noise level in counts from the amplitude levels measured in counts. The ratio represents the rate of signal over noise. Following Nortek AS (2020), the data was filtered for minimum correlation values of 70% and a minimum SNR of 10 dB. The results of the quality check are presented in Table E.1 for each experimental run.

Table E.1: ADV data statistics for the quality check performed on the measured velocity in the streamwise direction.

Experiment	Raw data points (nr)	Quality control passed (nr)	% Kept
P1_C_0_00_R1	37955	37658	99.22%
P1_C_E_10_R1	53207	52319	98.33%
P1_C_E_20_R1	53846	53610	99.56%
P1_C_M_05_R1	53179	52971	99.61%
P1_C_M_10_R2	47755	43814	91.75%
P1_C_M_20_R1	48317	47688	98.70%
P1_C_S_10_R1	50529	49470	97.90%
P1_C_S_20_R1	51633	50996	98.77%

Very few data points have been disregarded due to low correlation. However, experiment P1_C_M_10_R2 showed a relatively high number of data points being disregarded. A closer examination of the data for this experiment showed a relatively high percentage of the data points being disregarded at the start of the experiment (Figure E.3). Over time, the SNR seemed to improve due to the increasing amount of suspended particles in the water column. According to Van Rijn (1993), sandy sediment with a median grain size of roughly 348 µm is not expected to experience sediment motion below a flow velocity of 0.28 m s^{-1}. As a result, the data collected is still considered valid for use since the bulk of the disregarded data corresponds to flow velocities below 0.26 m s^{-1}.

E.1.3. Spike removal of ADV data

After removing bad-quality data, spikes were observed in the velocity time series of two experiments (Figure E.4). A spiky velocity time series can be attributed to problems such as weak spots, an inaccurate velocity range, low SNR values, or obstacles blocking the sound path between the emitter and receiver (Doroudian et al., 2010). However, despite a closer examination of the data and deployment files, no clear explanation was found for the spiky signal.

Following Doroudian et al. (2010) and Nortek AS (2020), the velocity spikes were removed using two filters: (1) a difference filter, and (2) a hard threshold filter. The difference filter compared a velocity measurement with the subsequent velocity measurement. The data point was disregarded if the difference exceeded 0.5 m s^{-1}. The second filter was applied to remove spikes of multiple points in a sequence. A hard threshold was set discarding velocities below 0.0 m s^{-1} and above 0.7 m s^{-1}.

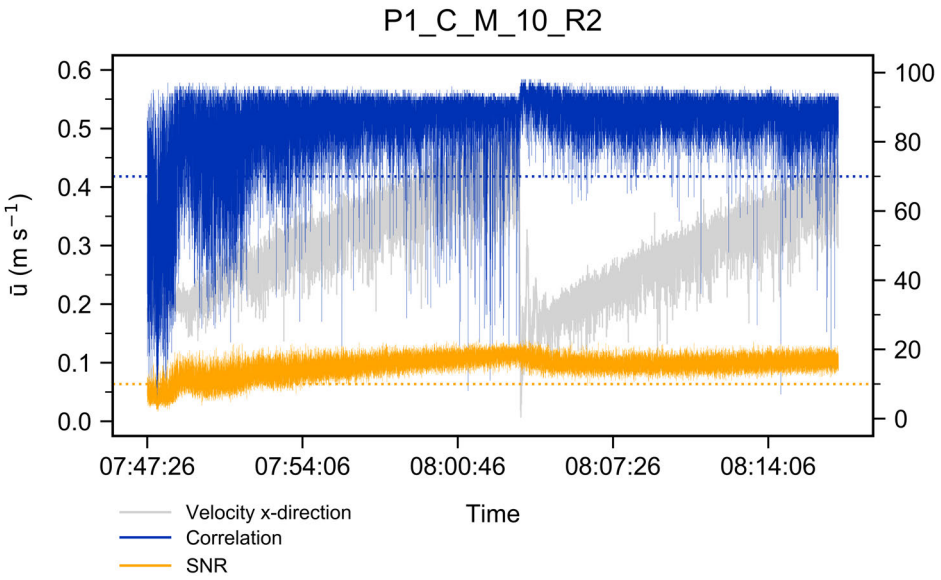

Figure E.3: The flow velocity and corresponding correlation and SNR values for experiment P1_C_M_10_R2.

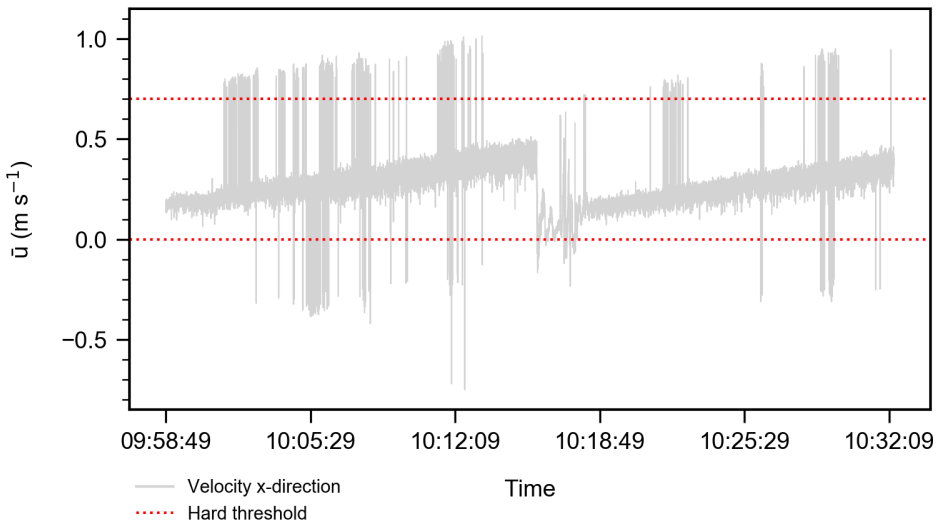

Figure E.4: The spiky flow velocity time series and hard thresholds set shown for experiment P1_C_E_20_R1.

Table E.2 presents the result of the spike removal. Only measurement P1_C_E_20_R1 experienced significant data loss due to spikes. However, the high measurement frequency of 25 Hz and the absence of significant data interruptions validate the collected data for use.

Table E.2: ADV data statistics for the spike removal performed on the measured velocity in the streamwise direction.

Experiment	Raw data points (nr)	Threshold passed (nr)	% Kept
P1_C_0_00_R1	37955	37955	100.00%
P1_C_E_10_R1	53207	53207	100.00%
P1_C_E_20_R1	53846	52527	97.55%
P1_C_M_05_R1	53179	53179	100.00%
P1_C_M_10_R2	47755	47755	100.00%
P1_C_M_20_R1	48317	48317	100.00%
P1_C_S_10_R1	50529	50452	99.85%
P1_C_S_20_R1	51633	51633	100.00%

E.2. Constant flow experiment

An analysis was conducted for the constant flow experiment using the ADV data and the collected bed load. The ADV data underwent two steps of processing: (1) bed-quality data was filtered out (Section), and (2) spikes were removed from the velocity time series. The collected bed load was dried in an oven for two weeks and then subjected to further analysis. The full process is illustrated in Figure E.5.

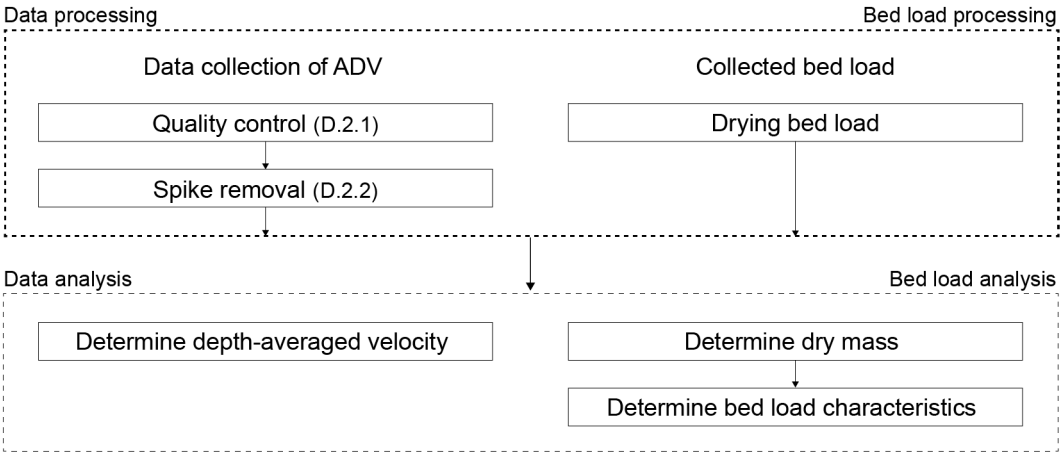

Figure E.5: Data processing procedure, along with the corresponding section in which explanation will be provided.

E.2.1. Correlation and SNR ratio of ADV data

Similarly to the slowly acceleration flow experiment (Section E.1.2), the data were filtered for minimum correlation values of 70% and a minimum SNR of 10 dB. The results of the quality check are presented in Table E.3.

In general, very few data points have been disregarded. However, two experiments showed a relatively high number of data points being disregarded. A closer examination of the data for these experiments showed that throughout the entire experiment, the correlation was occasionally below the set threshold (Figure E.6). However, the high measurement frequency of 25 Hz and the absence of significant data interruptions validate the collected data for use.

E.2.2. Spike removal of ADV data

Similarly to the slowly acceleration flow experiment, data was filtered for spikes after removing bad-quality data. Again, two filters were applied: (1) a difference filter, and (2) a hard threshold filter. The difference filter compared a velocity measurement with the subsequent velocity measurement. The data point was disregarded if the difference exceeded 0.5 m s^{-1}. The second filter was applied to remove spikes of multiple points in a sequence. A hard threshold was set discarding velocities below 0.0 m s^{-1} and above 0.7 m s^{-1}.

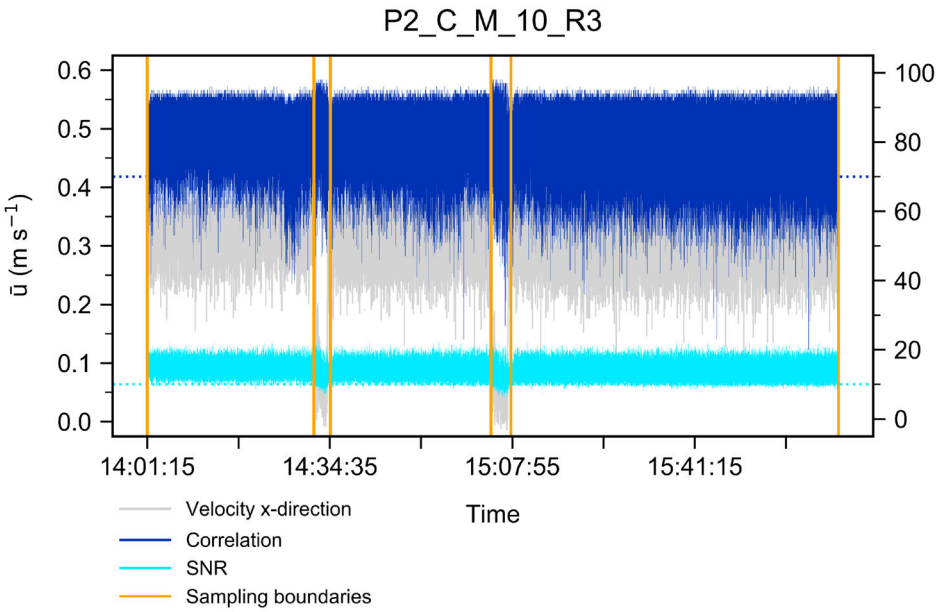

Figure E.6: The flow velocity and corresponding correlation and SNR values for experiment P2_C_M_10_R3.

Table E.3: ADV data statistics for the quality check performed on the measured velocity in the streamwise direction.

Experiment	Raw data points (nr)	Quality control passed (nr)	% Kept
P2_C_0_00_R1	215850	214657	99.45%
P2_C_0_00_R2	223621	221128	98.89%
P2_C_0_00_R3	209073	207192	99.10%
P2_C_0_00_R4	200462	200412	99.98%
P2_C_0_00_R5	204483	204471	99.99%
P2_C_E_10_R1	191507	190873	99.67%
P2_C_E_10_R2	213042	210937	99.01%
P2_C_E_10_R3	201077	200039	99.48%
P2_C_E_10_R4	199160	198908	99.87%
P2_C_E_10_R5	216870	216865	99.99%
P2_C_E_20_R1	202085	201510	99.72%
P2_C_E_20_R2	217255	216154	99.49%
P2_C_M_10_R1	231027	222091	96.13%
P2_C_M_10_R2	229452	226419	98.68%
P2_C_M_10_R3	194778	174035	89.35%
P2_C_M_10_R4	253682	249606	98.39%
P2_C_M_10_R5	198862	176926	88.97%
P2_C_S_10_R1	218612	217814	99.64%
P2_C_S_10_R2	215794	213452	98.91%
P2_C_S_10_R3	232622	230802	99.22%
P2_C_S_10_R4	219655	217103	98.84%
P2_C_S_10_R5	200869	197795	98.47%
P2_C_S_20_R1	200420	200192	99.89%
P2_C_S_20_R2	209404	208493	99.57%

Table E.4 presents the result of the spike removal. Only a few measurements showed spikes. However, the data is validated for use since the velocity was kept constant over time in this experiment, the measurement frequency of 25 Hz is proper, and there is an absence of significant data interruptions.

Table E.4: ADV data statistics for the spike removal performed on the measured velocity in the streamwise direction.

Experiment	Raw data points (nr)	Threshold passed (nr)	% Kept
P2_C_0_00_R1	215850	215850	100.00%
P2_C_0_00_R2	223621	223621	100.00%
P2_C_0_00_R3	209073	209073	100.00%
P2_C_0_00_R4	200462	200462	100.00%
P2_C_0_00_R5	204483	204483	100.00%
P2_C_E_10_R1	191507	191507	100.00%
P2_C_E_10_R2	213042	212461	99.73%
P2_C_E_10_R3	201077	199760	99.35%
P2_C_E_10_R4	199160	199160	100.00%
P2_C_E_10_R5	216870	216870	100.00%
P2_C_E_20_R1	202085	201794	99.86%
P2_C_E_20_R2	217255	217255	100.00%
P2_C_M_10_R1	231027	231022	100.00%
P2_C_M_10_R2	229452	229030	99.82%
P2_C_M_10_R3	194778	194778	100.00%
P2_C_M_10_R4	253682	253602	99.97%
P2_C_M_10_R5	198862	198856	100.00%
P2_C_S_10_R1	218612	218551	99.97%
P2_C_S_10_R2	215794	215794	100.00%
P2_C_S_10_R3	232622	227890	97.97%
P2_C_S_10_R4	219655	219049	99.72%
P2_C_S_10_R5	200869	200869	100.00%
P2_C_S_20_R1	200420	200419	100.00%
P2_C_S_20_R2	209404	209087	99.85%

F

Supporting figures

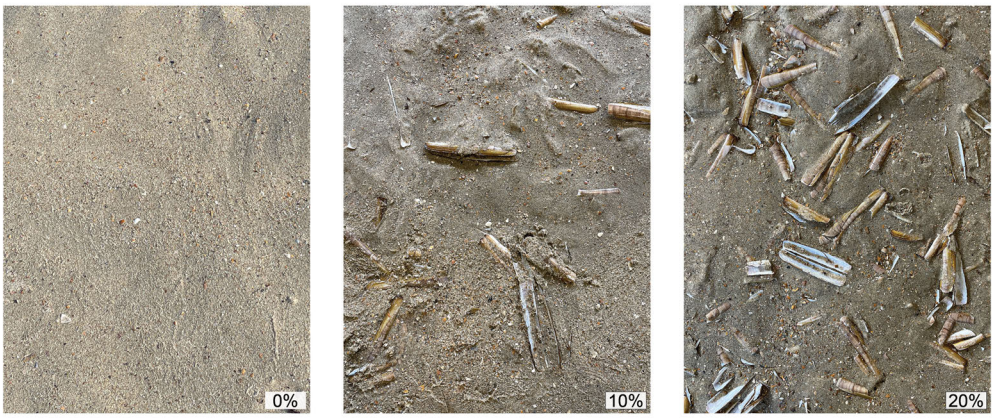

Figure F.1: Sediment-shell bed composition: *Ensis leei* shells.

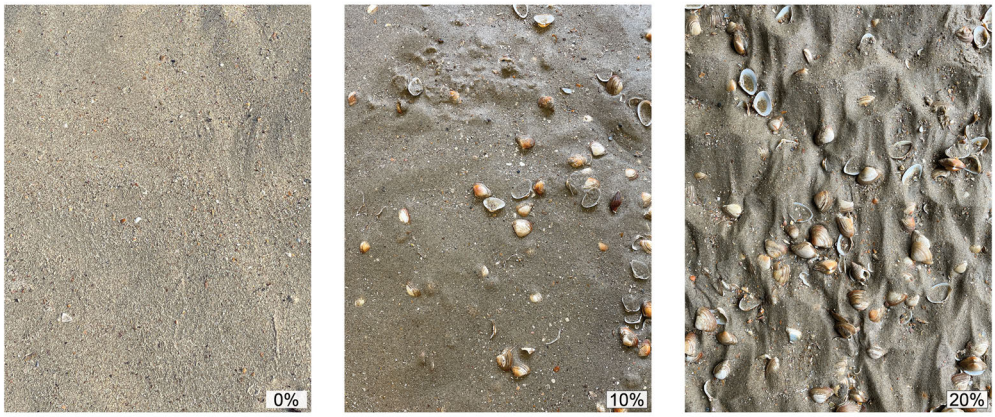

Figure F.2: Sediment-shell bed composition: *Spisula subtruncata* shells.

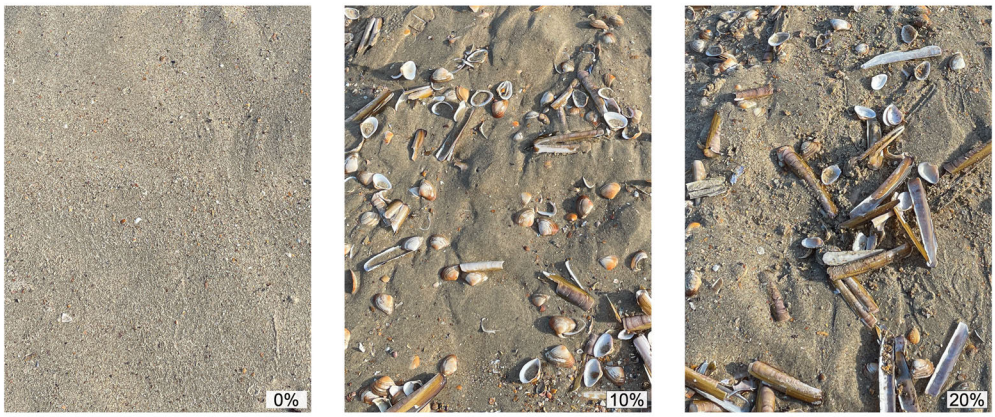

Figure F.3: Sediment-shell bed composition: Mixture of shells.

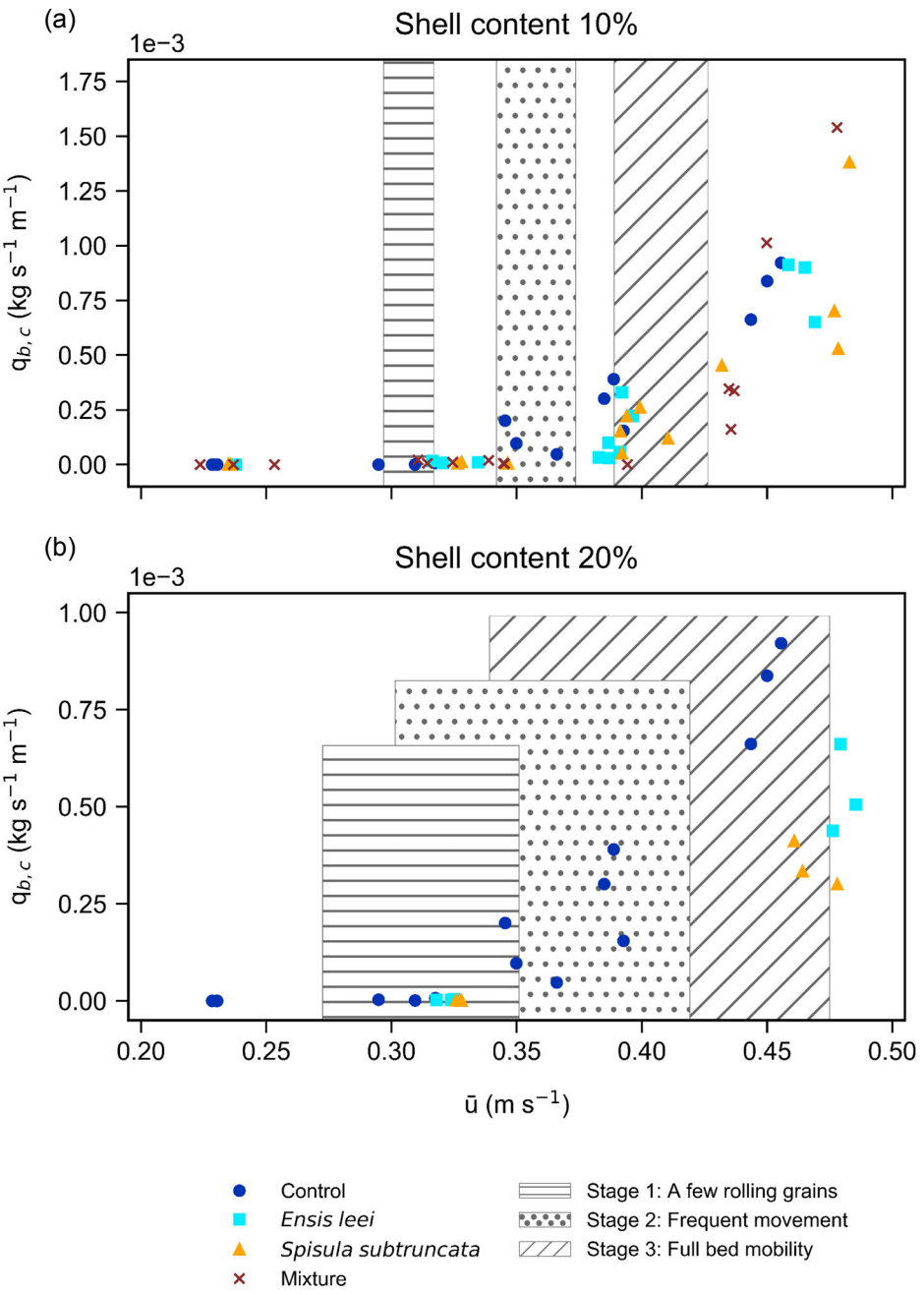

Figure F.4: Total transported bed load versus depth-averaged velocity for a sediment-shell bed composition with a shell content of 10% (a) and a shell content of 20% (b). The markers indicate sediment-shell bed compositions, and the hatches represent the range of motion stages.

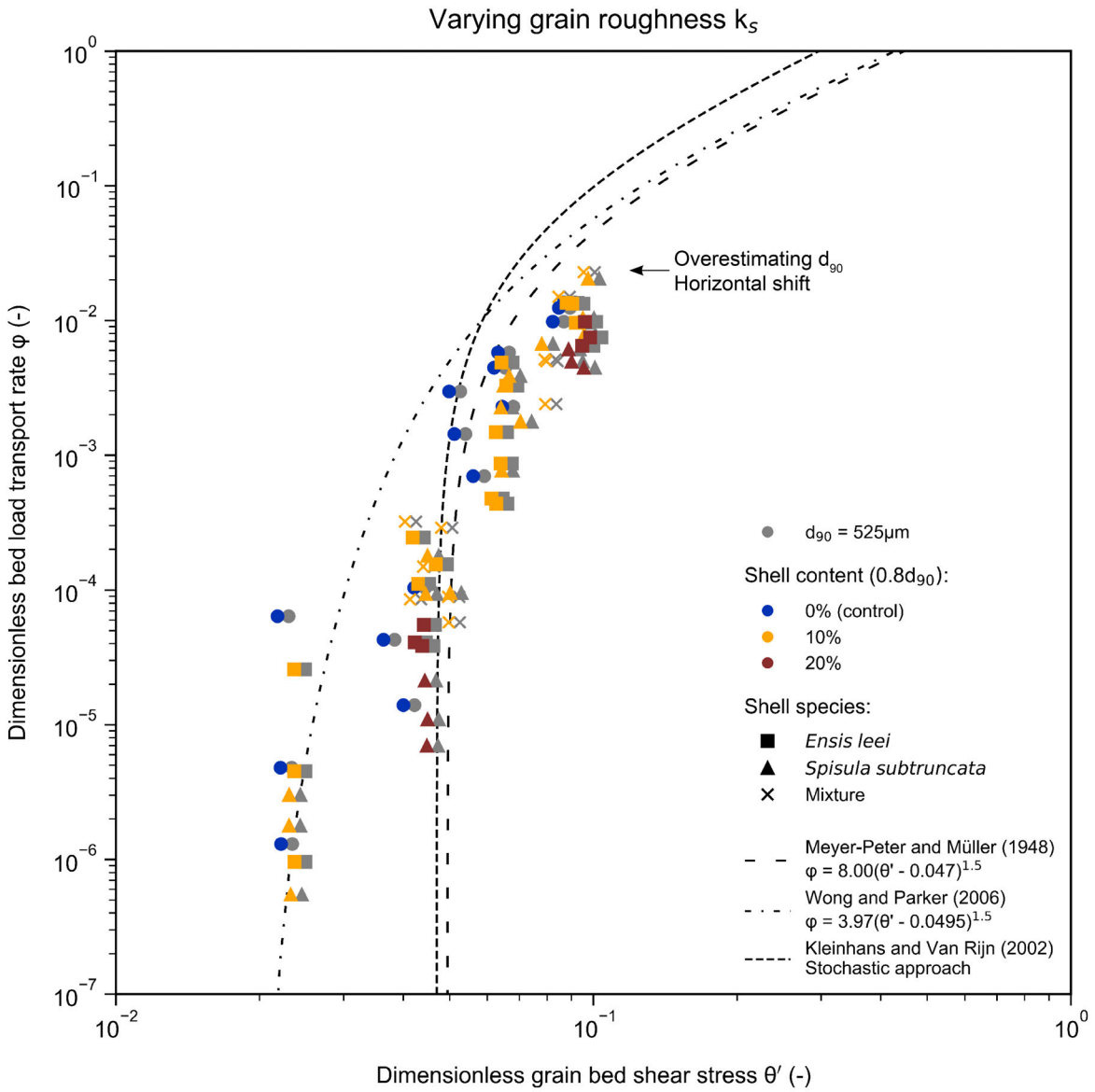

Figure F.5: Dimensionless bed load transport rate versus dimensionless grain bed shear stress using varying grain roughness approximations. Comparison to MPM and WP transport predictors. The colors indicate shell content, and markers indicate the shell species.

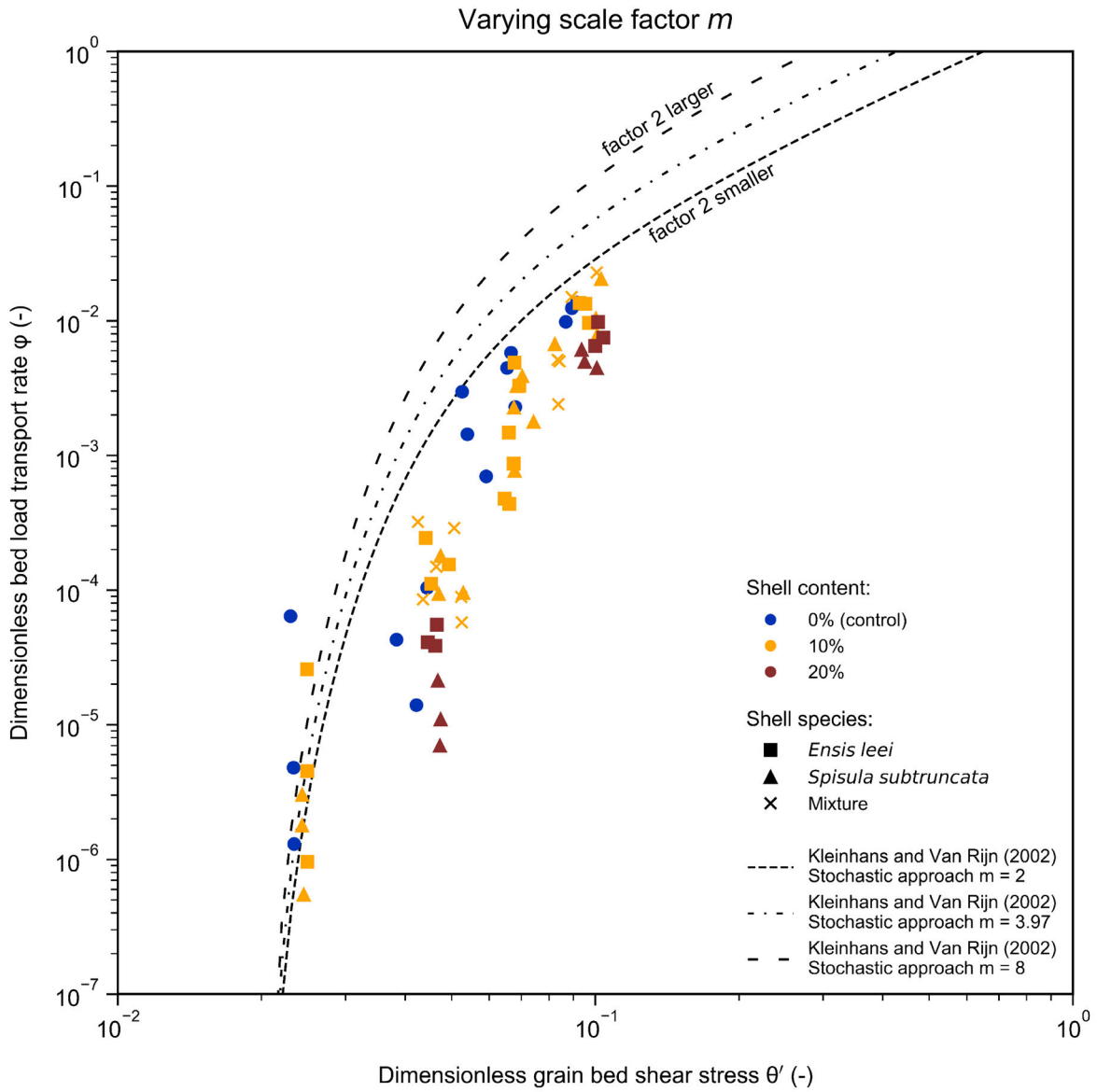

Figure F.6: Dimensionless bed load transport rate versus dimensionless grain bed shear stress. Comparison to the stochastic approach of WP transport predictor with varying scale factor m. The colors indicate shell content, and markers indicate the shell species.

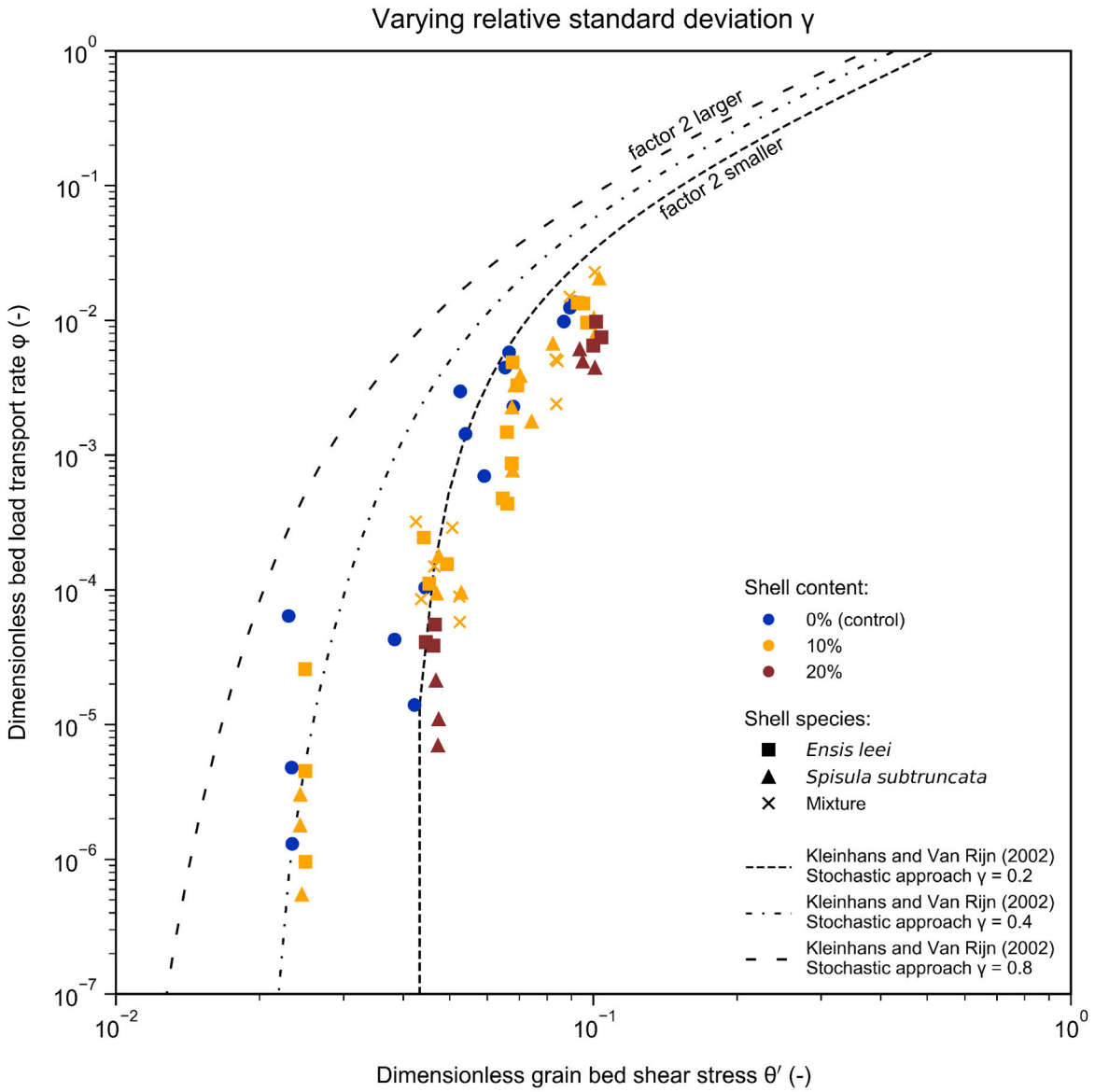

Figure F.7: Dimensionless bed load transport rate versus dimensionless grain bed shear stress. Comparison to the stochastic approach of WP transport predictor with varying relative standard deviation γ. The colors indicate shell content, and markers indicate the shell species.

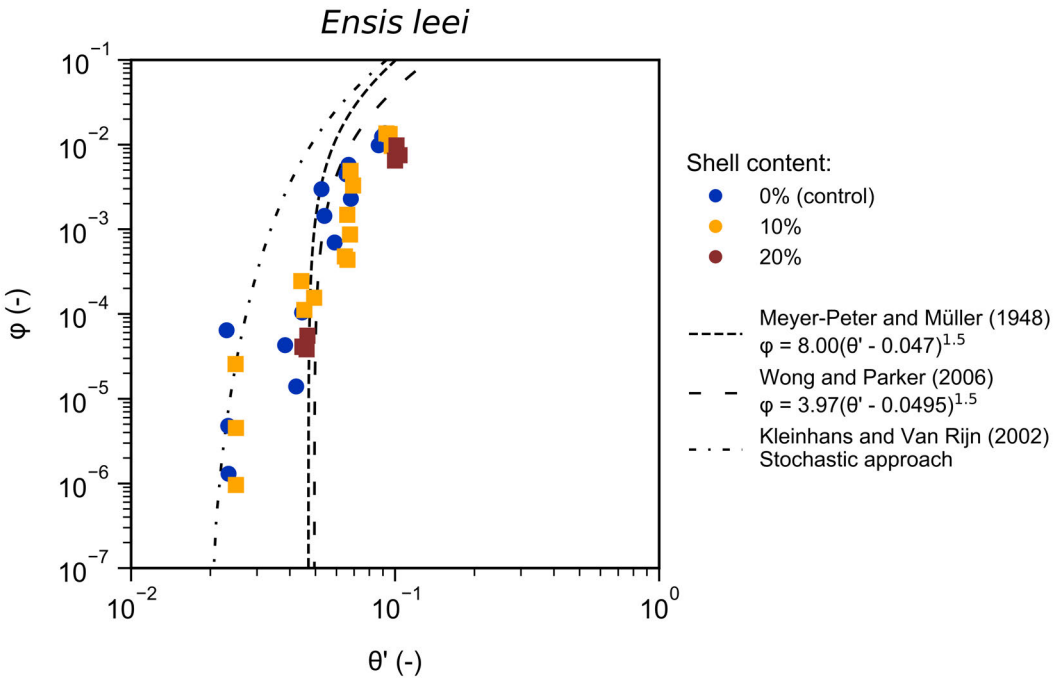

Figure F.8: Dimensionless bed load transport rate versus dimensionless grain bed shear stress for a sediment-shell bed composition consisting of *Ensis leei* shells. Comparison to MPM and WP transport predictors. The colors indicate shell content.

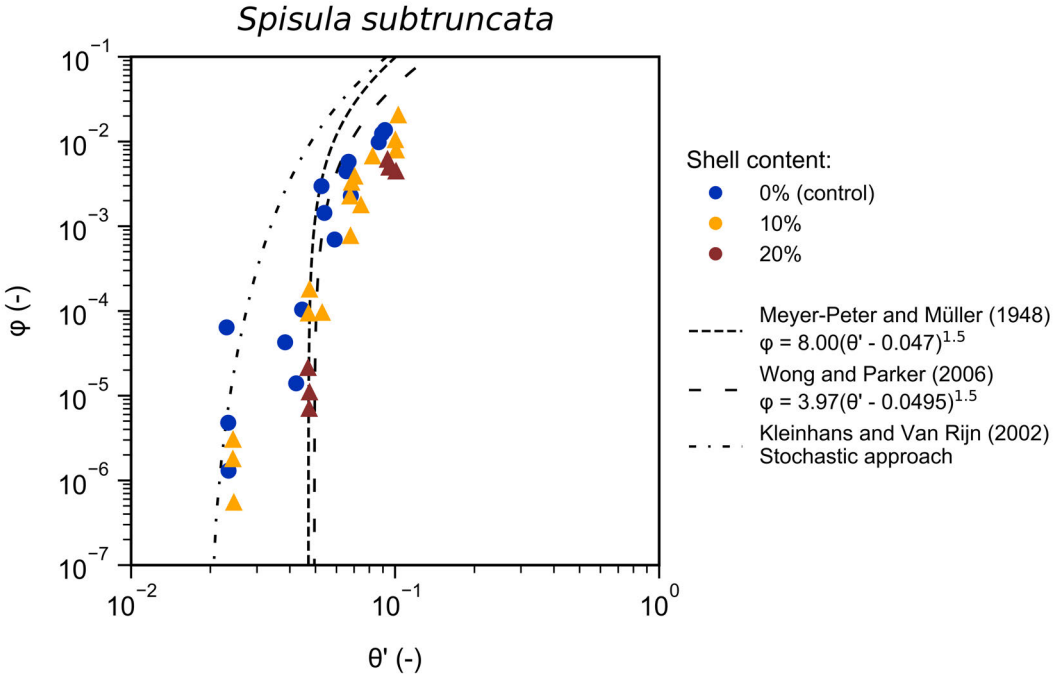

Figure F.9: Dimensionless bed load transport rate versus dimensionless grain bed shear stress for a sediment-shell bed composition consisting of *Spisula subtruncata* shells. Comparison to MPM and WP transport predictors. The colors indicate shell content.

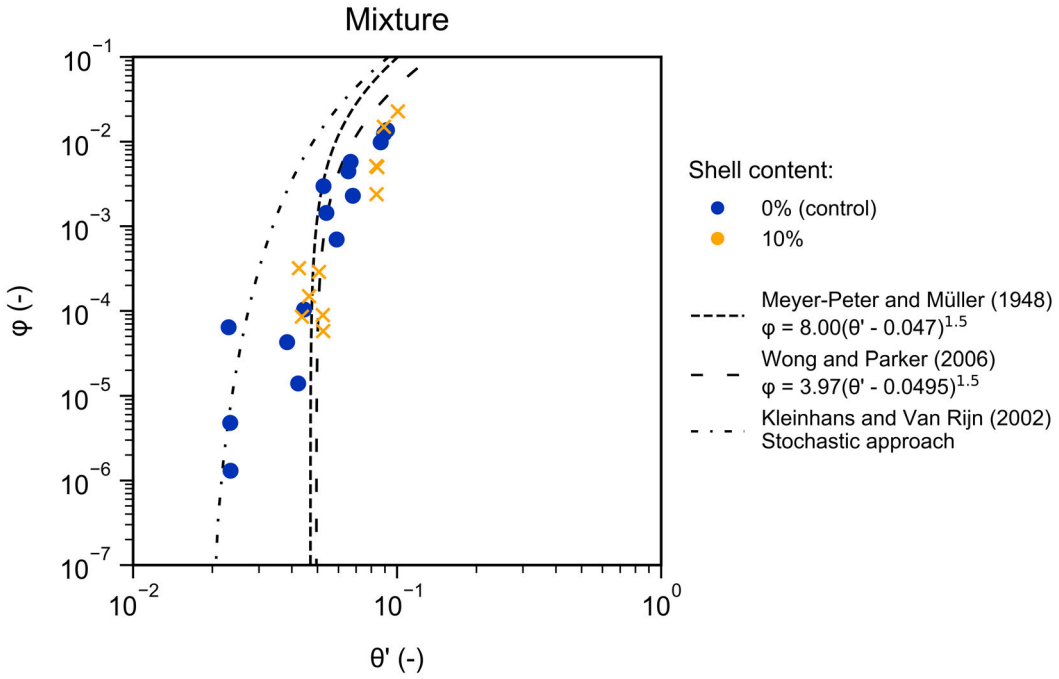

Figure F.10: Dimensionless bed load transport rate versus dimensionless grain bed shear stress for a sediment-shell bed composition consisting of both shell species shells. Comparison to MPM and WP transport predictors. The colors indicate shell content.